UNIVERSIDADE FEDERAL DE PERNAMBUCO
CENTRO DE CIÊNCIAS EXATAS E DA NATUREZA
PROGRAMA DE PÓS-GRADUAÇÃO EM FÍSICA

Daniel Miranda Castro

Phenomenological Renormalization Group Applications to Brain Data

Recife

2024

Daniel Miranda Castro

Phenomenological Renormalization Group Applications to Brain Data

Tese apresentada ao Programa de PósGraduação em Física da Universidade Federal de Pernambuco, como requisito parcial para a obtenção do título de Doutor em Física.

Área de Concentração: Dinâmica Não-Linear, Caos e Sistemas Complexos

Orientador (a): Prof. Dr. Mauro Copelli

Recife

2024

.Catalogação de Publicação na Fonte. UFPE - Biblioteca Central

Castro, Daniel Miranda.
Phenomenological Renormalization Group Applications to Brain Data / Daniel Miranda Castro. - Recife, 2024.
0f.: il.

Tese (Doutorado), Universidade Federal de Pernambuco, Centro de Criências Exatas e da Natureza, Programa de Pós-Graduação em Física, 2024.
Orientação: Mauro Copelli.

1. Phenomenological renormalization group; 2. critical phenomena; 3. brain criticality. I. Copelli, Mauro. II. Título.

UFPE-Biblioteca Central CDD 530.1

Daniel Miranda Castro

Phenomenological Renormalization Group Applications to Brain Data

Tese apresentada ao Programa de Pós-Graduação em Física da Universidade Federal de Pernambuco, como requisito parcial para a obtenção do título de Doutor em Física.

Data de aprovação: 22/08/2024.

BANCA EXAMINADORA

_____

Prof. Dr. Mauro Copelli Lopes da Silva
Orientador
Universidade Federal de Pernambuco

_____

Prof. Dr. Antônio Murilo Santos Macêdo
Examinador Interno
Universidade Federal de Pernambuco

_____

Prof. Dr. Paulo Roberto de Araujo Campos
Examinador Interno
Universidade Federal de Pernambuco

_____

Prof. Dr. Bruno Coelho César Mota
Examinador Externo
Universidade Federal do Rio de Janeiro

_____

Prof. Dr. Hans Jürgen Herrmann
Examinador Externo
École supérieure de physique et de chimie
Industrielles de la ville de Paris

Dedico esta tese ao meu avô, Seu Miranda, que aos noventa e sete anos começou a plantar o jardim da sua casa nova.

ACKNOWLEDGEMENTS

Primeiro, agradeço a todos da minha família, nuclear (Mauro, Ana, Lucas e Pedro) e estendida, com todos os tios e tias e primos e cunhadas que tiver direito! E Joquinha!!! Meu lar é onde vocês estiverem. Um agradecimento especial e segunda dedicatória a Nicolly, minha companheira, que esteve do meu lado todos os dias da minha escrita. Viver do seu lado me ensina uma coisinha nova todos os dias.

Agradeço a Mauro Copelli, pela orientação e amizade ao longo dos anos de doutorado. Poder trabalhar com quem a gente admira, como profissional e humano, é de um privilégio que não dá para calcular. Esse agradecimento também se estende aos outros professores que me acolheram, discutiram e deram oportunidades para que eu crescesse com a minha pesquisa: Fernando Nóbrega, Ernesto Raposo, Fernanda Matias, Bruno Mota...

Agradeço a todos que fazem o grupo do SysCompNeuro existir, presentes e egressos, e que juntos são um projeto maior do que a soma das pesquisas de cada um. Obrigado em particular para Gustavo, Vinícius, Kaio, Thaís e Antônio.

Deixo agradecimentos coletivos à minha segunda família da casa Motoka; a todo o pessoal do discord, que deixava o dia mais leve e divertido depois do expediente; aos meus amigos da música — em especial a Vinícius — que me ensinaram muito nesse momento que eu fui um pouco menos músico; e aos amigos da física da UFPE, que dão vida ao lugar que a gente vive todo dia. Vou também agradecer nominalmente a mais um monte de gente que de alguma forma foi significativa para mim durante esse ciclo: João, Mateus, Bel, Mari, Mari, Vinícius, Nemo, Iacapuca, Gustavo, Thiago, Pran, Ricardo, Iana, Maya, Júlia, Nilo, Amanda, Lucas, Ediane, Elisângela, Edna, Gildo, Álvaro, André, João, Eriton, Juan, Iago e quem mais eu não pude lembrar no momento.

Agradeço ao suporte financeiro do CNPq.

Por fim, agradeço aos leitores, pela disponibilidade em conhecer este texto. Espero que tenham uma boa experiência.

"Making the simple complicated is commonplace; making the complicated simple, awesomely simple, that's creativity."

(Charles Mingus)

ABSTRACT

The critical brain hypothesis has emerged in the last decades as a fruitful theoretical framework for understanding collective neuronal phenomena. Lending support to the idea that the brain operates near a phase transition, Beggs and Plenz were the first to report experimentally recorded neuronal avalanches, whose distributions coincide with the mean-field directed percolation (DP) universality class, which comprises a variety of models in which a phase transition occurs between an absorbing (silent) and an active phase. However, this hypothesis is highly debated, as neuronal avalanches analyses and other common statistical mechanics tools may struggle with challenges ubiquitous in living systems, such as subsampling and the absence of an explicit model for a complete theory of neuronal dynamics. In this context, Meshulam et al. recently proposed a phenomenological renormalization group (PRG) method to deal with neural networks with a model independent analysis. The procedure consists of recursively manipulating the data, obtaining an increasingly coarse-grained description of the activity after each iteration. Under a critical regime, non-trivial correlations and scale-free behavior should be unveiled as we simplify our description. This can be inferred from a series of statistical features of the data, which lead us to different scaling relations. Here, we apply the PRG in two different experimental setups: spiking data from the anesthetized rat visual cortex and functional magnetic resonance imaging (fMRI) time series from young and aging humans. In the first, we investigate the interplay between scale invariance and cortical states, as assessed by populational spiking variability coefficient of variation (CV). In the latter, we find empirical relations between PRG phenomenological exponents and explore connections between those exponents and clinical traits of the experiment participants.

Keywords: phenomenological renormalization group; critical phenomena; brain criticality; scaling relations; neuronal avalanches; cortical states; rat visual cortex; urethane; human fMRI.

CONTENTS

1 INTRODUCTION

This thesis is a perspective on comprehending certain aspects of brain dynamics through the lens of statistical physics. To accommodate readers from diverse backgrounds, we begin by providing context on how different sciences involved in this interdisciplinary subject engage with each other.

1.1 AN OVERVIEW OF SYSTEMS NEUROSCIENCE

Humanity's historical fascination with the function of the brain can be traced back to ancient civilizations like Greece and Egypt (GROSS, 1987). However, contemporary neuroscience has been shaped by very recent breakthroughs. For instance, the idea that the brain operates via the action of individual cells called neurons, the so called neuron doctrine, was established by Ramón y Cajal only in the late 19th century; the first quantification of a single neuron dynamics, named the Hodgkin-Huxley model, earned its creators the Nobel prize in Medicine in 1963 (KANDEL et al., 2000).

The seemingly late development of the field is not unreasonable. It should sound rather unsurprising that, as a physical system, a chunk of matter capable of orchestrating body functions, while making sense of the world around itself - and not so often, reading PhD theses - is dazzlingly complex. The spatial scales involved in the process span several orders of magnitude, ranging from the nanometer scale of neurons' ion channels and synapses to the scale of tens of centimeters of the whole brain (Fig. 1). Temporally, single neuron dynamics operates on the order of milliseconds, whilst brain connectivity may undergo changes over the course of years (Fig. 2A). Let's make a brief overview on the issue, taking a neuron as starting point.

In a nutshell, neurons are viewed as the basic computational units of the brain, amounting to roughly 50% of the cell population of the organ. The other 50%, collectively known as glia, serve supportive roles such as metabolic maintenance, structural support and immune defense of the nervous system (KANDEL et al., 2000). To quantify a single neuron's dynamics, detailed models often use systems of coupled non-linear differential equations, describing its electrical potential and voltage-dependent ion channels (SKINNER, 2006).

One distinctive feature from neuron dynamics is the generation of action potentials. Upon

reaching a certain threshold, the electric potential across the neuron's membrane suffers a rapid and transient change. The intricacies of threshold dynamics, refractory periods and curve shapes can exhibit considerable diversity, depending on the morphological attributes of the cell. However, for statistic purposes we can assume the action potential as an all-or-none event. Importantly, it is the major source of signal transmission between neurons.

This transmission, on its turn, is mediated through what we call synapses. Synaptic interactions are also typically characterized by non-linear dynamics, possessing multiple forms. Chemical synapses can be classified as either excitatory or inhibitory, based on the chemical messengers – neurotransmitters – they release. That is, the emitting pre-synaptic neuron facilitates or hinders the generation of an action potential (also called *spike*) in the receiving post-synaptic neuron through a chemical synapse. Furthermore, neurons as a whole can be identified as excitatory or inhibitory, as they release the same type of neurotransmitter through all their outgoing synapses (KANDEL et al., 2000). Additionally, there is another type of synapses known as electrical synapses. These synapses bidirectionally couple two neurons via gap junctions, allowing ions to flow directly between them.

One remarkable feature of chemical synaptic transmission is that it is not only stochastic, but also fairly *unreliable*: the probability of neurotransmitter release in response to an incoming pre-synaptic action potential is heavily influenced by past dynamics and neuron type, reaching levels as low as 0.1 (KOCH, 2004). Understanding how the brain copes with this unreliability to integrate and encode signals remains an open question.

A third signaling mechanism occurs through neuromodulation. Neuromodulators differ from classical neurotransmitters in that they typically have more diffuse effects and act over longer time scales. While neurotransmitters are involved in rapid point-to-point communication between neurons at synapses, neuromodulators often induce more gradual and sustained modifications in neural activity. As a result, it plays a role in regulating long-term changes in synaptic plasticity, learning, and memory, as well as in the overall state and functional connectivity of neural networks (LEE; DAN, 2012; PEDROSA; CLOPATH, 2017).

The final aspect of this overview regards brain anatomical structure. At the network level, the cerebral cortex often exhibits columnar organization, characterized by a complex hierarchical-modular architecture, conferring it both small-world and scale free features (EGUÍLUZ et al., 2005; HILGETAG; GOULAS, 2016). This non-trivial network structure introduces even more heterogeneity in local network dynamics (LITWIN-KUMAR; DOIRON, 2012). At the whole-brain level, one can also explore methods for quantifying its geometric shape. Throughout develop-

ment, the mechanical stress induced by tissue growth leads to the folding of the cortex, creating a fractal landscape of sulci and gyri, which also holds significance for brain function (TALLINEN et al., 2016). Seeking allometric patterns across species to understand the role of the brain's geometry is also an active research field (HERCULANO-HOUZEL; MOTA; LENT, 2006; MOTA; HERCULANO-HOUZEL, 2015; VENTURA-ANTUNES; MOTA; HERCULANO-HOUZEL, 2013).

While not an exhaustive compilation of brain components, this list aims to expose some of the key challenges in the interdisciplinary endeavor of comprehending brain dynamics and mechanisms. Experimentally, striking a balance between sufficient spatiotemporal resolution, access to various scales, reproducibility, and non-invasiveness is a highly non-trivial task (Fig. 2B). On the theoretical front, simply expanding upon established theories is often impractical, given that neural systems, in general, exhibit novel dynamics and components that are not yet understood at a formal level. Hence, it is necessary to further develop existing theories. For instance, consider the example of a comparison with theoretical solid state physics by Helias and Dahmen (HELIAS; DAHMEN, 2020): often driven by the characterization of new materials and quantum states, systems from solid state physics have the Coulomb interaction as the source of a multitude of phenomena. It is a symmetric interaction, instantaneous and continuously present over time. In contrast, interactions in neural systems are asymmetric, delayed and mediated by temporally short pulses. From this standpoint, a neuronal network may be regarded as an unconventional physical system, offering phenomena not yet observed in solid state physics.

As a result, deriving brain functions from foundational principles remains a challenge. This work focuses on one of the potential frameworks in the search for principles in brain physics: the critical brain hypothesis, which will be explored in the next section.

Figure 1 – Illustration of some dynamical systems relevant to systems neuroscience at different scales, along with characteristic quantities and features. From microscopic to macroscopic: (A) Neurotransmitters (purple dots) diffusing through synaptic clefts from pre- to post-synaptic neurons; (B) A single neuron and its synapses (green dots) across dendrites; (C) small neuronal circuits; (D) hierarquically structured cortical columns; and (E) whole brain.

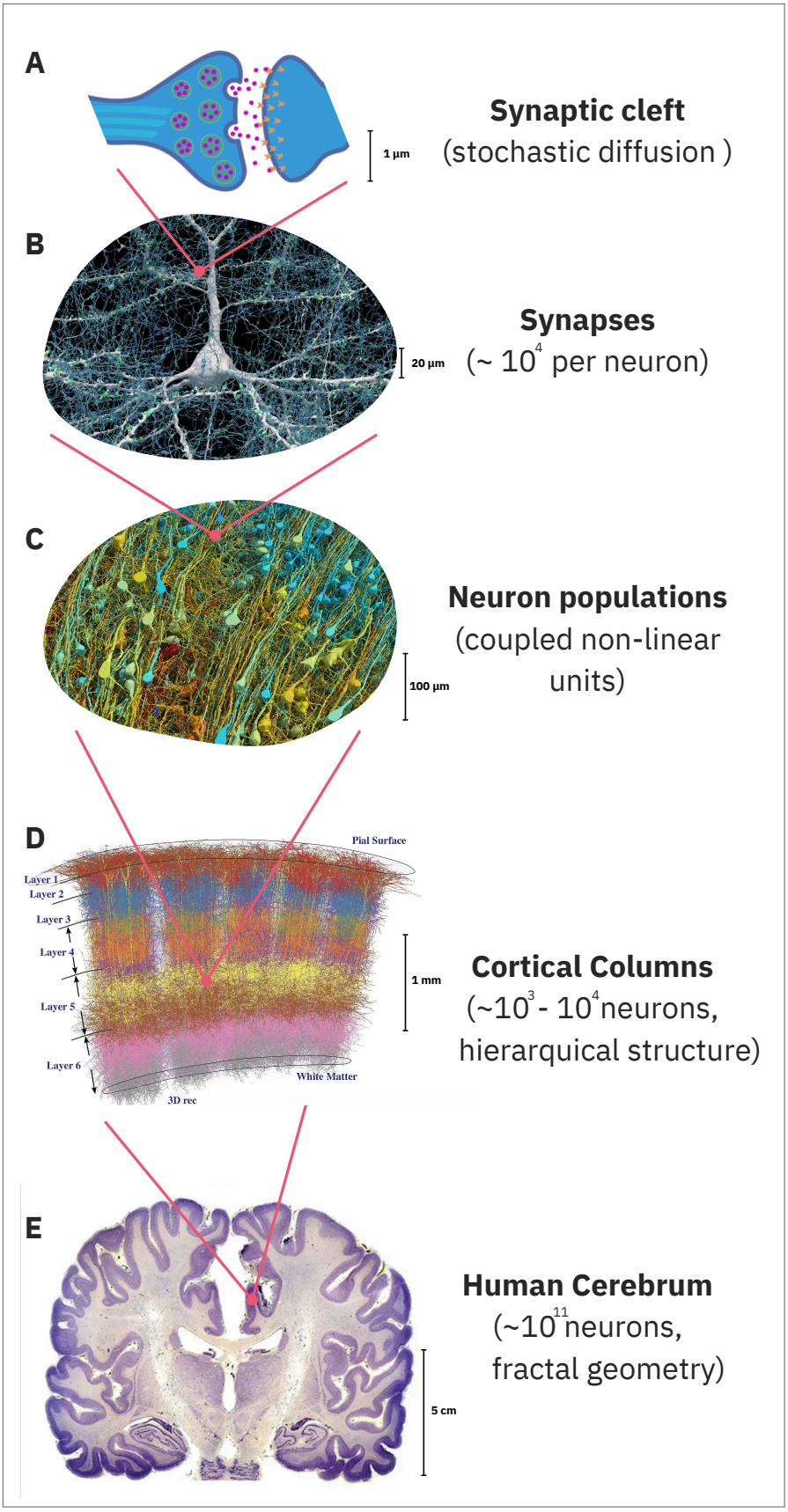

Source: Adapted from (DEFELIPE, 2011) and Google Research & Lichtman Lab.

Figure 2 – Typical length and time scales in systems neuroscience. (A) Different networks and dynamics relevant to brain function span several orders of magnitude. (B) Different experimental techniques available and their acquisition resolutions. Shades represent the scales from (A), for comparison.

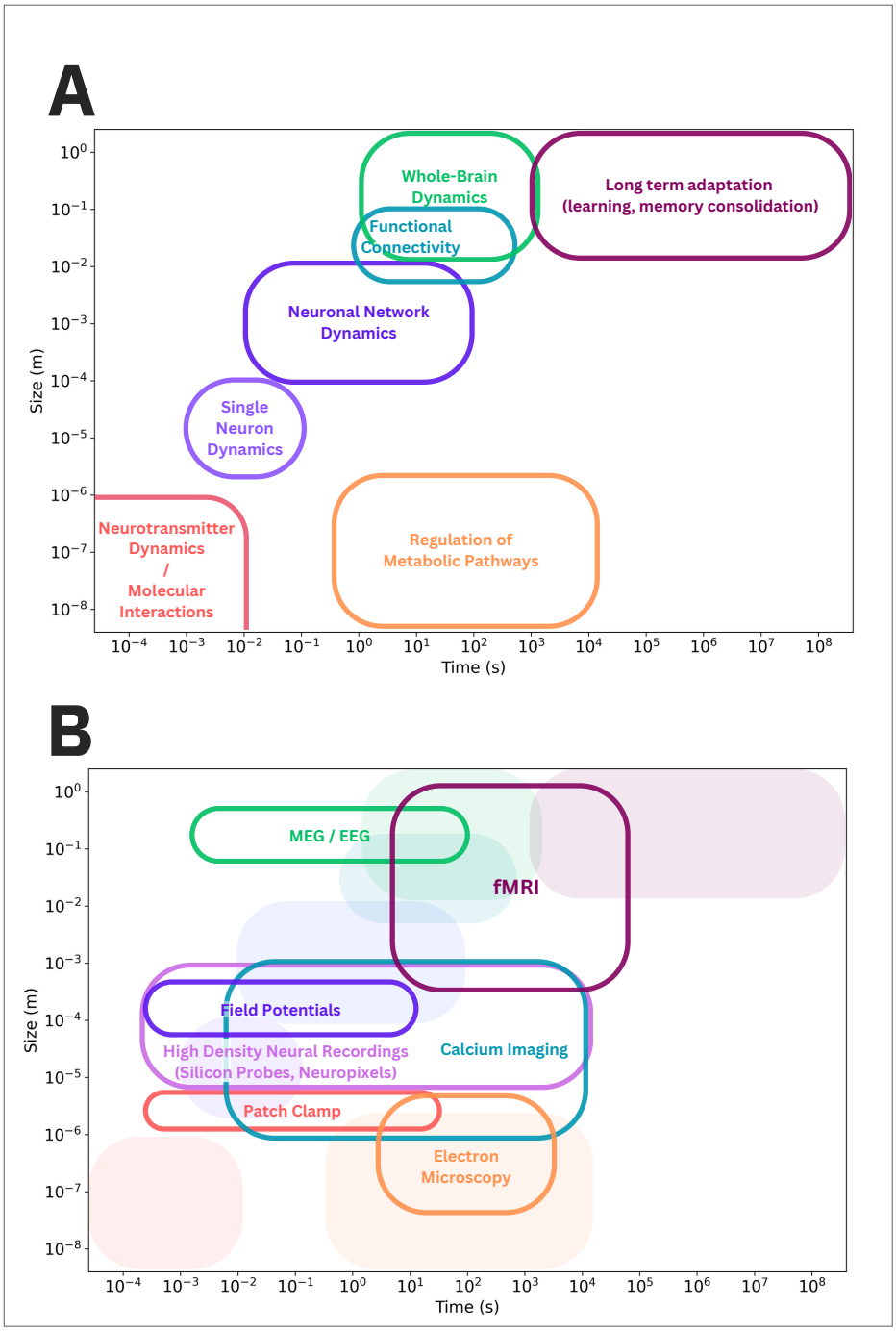

Source: Adapted from (SEJNOWSKI; CHURCHLAND; MOVSHON, 2014; HAMPEL et al., 2018)

1.2 THE CRITICAL BRAIN HYPOTHESIS

1.2.1 First evidences

In this section, we go deeper into the origins and development of the critical brain hypothesis over the past few decades. The hypothesis posits that neuronal activity within the brain operates near a phase transition, in the statistical physics sense of the term. In this state, neuronal networks exhibit a delicate balance between stability and flexibility, enabling optimal information processing and responsiveness to stimuli.

Early findings pointing in this direction can be found in whole brain data from human magnetoencephalogram (MEG) and electroencephalogram (EEG) signals (LINKENKAER-HANSEN et al., 2001). Klaus Linkenkaer-Hansen and collaborators found these signals have long-range temporal correlations and temporal self-affinity. These observations led to the first proposition of self organized critical dynamics as a potential explanation for brain dynamics.

The hypothesis gained traction with the release of Beggs and Plenz's seminal paper on neuronal avalanches (BEGGS; PLENZ, 2003). In their work, they used multielectrode arrays in *in vitro* cortical slices, providing access to neuronal networks spontaneous activity spatiotemporal patterns in the μm and ms scale for a few hours (Fig. 3A).

For this particular framework, a neuronal avalanche is characterized as a continuous activity period, both preceded and succeeded by a time bin Δt devoid of any activity, as illustrated in Fig. 3B. The duration of a neuronal avalanche, denoted as T, represents the number of time bins within that interval, while its size, s, corresponds to the number of electrodes activated during this period. In such setup, they found that avalanches display power law distributions with respect to their size and duration, *i.e.* $P(s) \propto s^{-\tau}$ and $P(\frac{T}{\Delta t}) \propto (\frac{T}{\Delta t})^{-\tau_t}$, with $\tau = 1.5$ and $\tau_t = 2$ (Fig. 3C-3F). As we will see below, this result makes a explicit connection between neuronal activity and the physics of phase transitions.

1.2.1.1 Power laws and phase transitions

Power law distributions have a deep meaning for a system's behavior. First, it means that in general the system does not have a characteristic scale. Starting from a generic power law $p(x) = cx^{-\alpha}$, the statistical moments for this distribution are

$$\langle x^m \rangle = \int_{-\infty}^{\infty} x^m p(x) dx \quad \propto x^{m-\alpha+1}, \tag{1.1}$$

Figure 3 – (A) Local field potential (LFP) signals from multielectrode arrays give access to the electrical activity of tens to hundreds of neurons per electrode. (B) Definition of neuronal avalanche as an interval of activity between two periods of no activity. (C) Power-law distribution of avalanche sizes for different choices of time bin Δt. Inset shows fitted scaling exponents, originally denoted as α, for each bin length. (D) Power-law distribution of avalanche sizes considering size as the total electrical potential involved in the avalanche. Inset shows results for individual slice cultures. (E) Power-law distribution of avalanche durations for different Δt. (F) Similar as (E), rescaling durations by bin length.

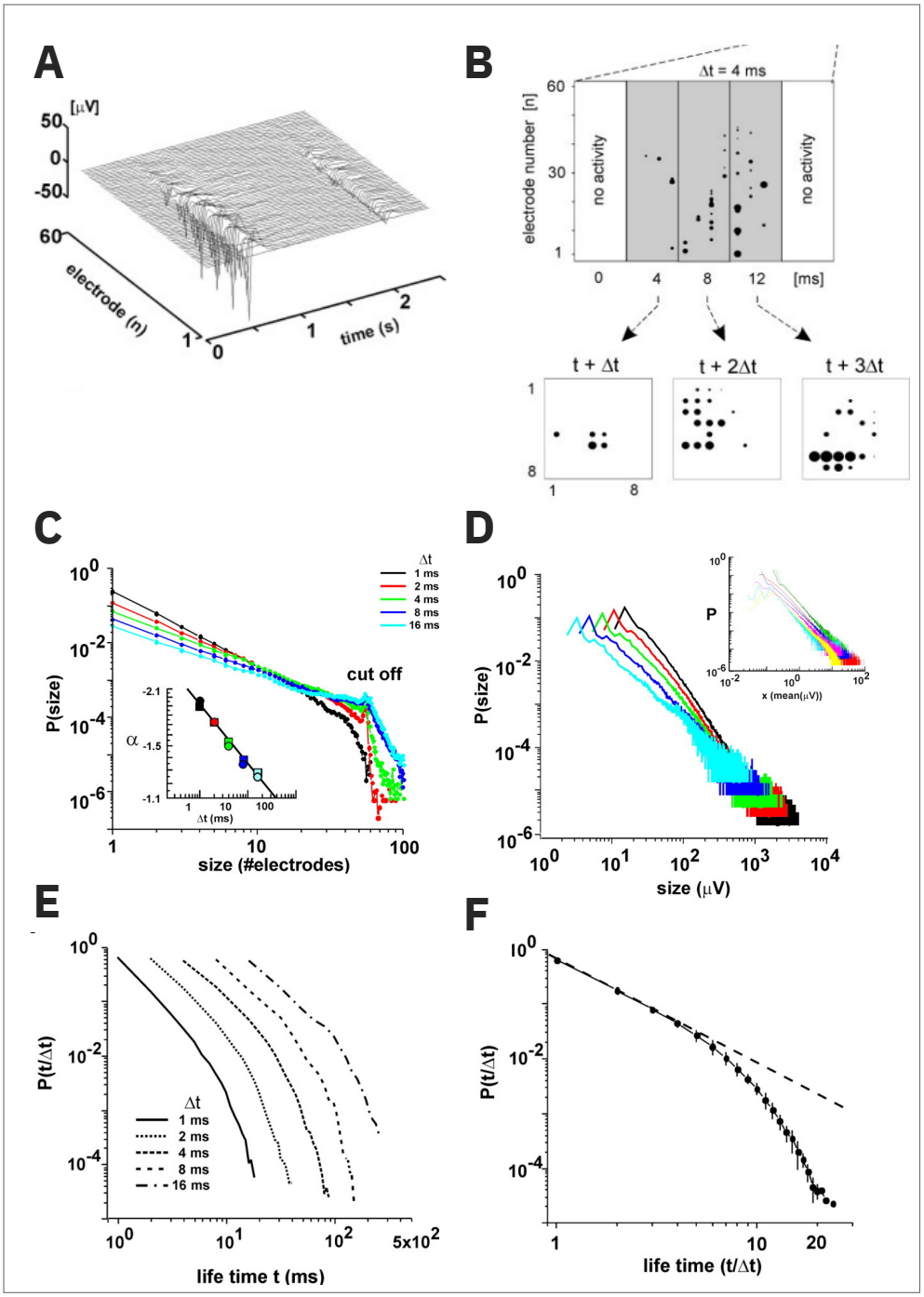

Source: Adapted from (BEGGS; PLENZ, 2003)

implying that only moments with $m < \alpha - 1$ converge; in particular, for $\alpha < 3$ the variance is not well defined, which makes the definition of a typical scale like *"mean $\pm$ standard deviation"* meaningless. Additionally, power laws are homogeneous functions, which have the property of being invariant to scaling in its argument,

$$f(Ax) = c(Ax)^{-\alpha} = A^{-\alpha} f(x), \tag{1.2}$$

i.e. its structure is preserved regardless of the scale choice.

Figure 4 – Visualization of scale invariance in the geometry of a coastline after recursive "zoom-ins" in the image.

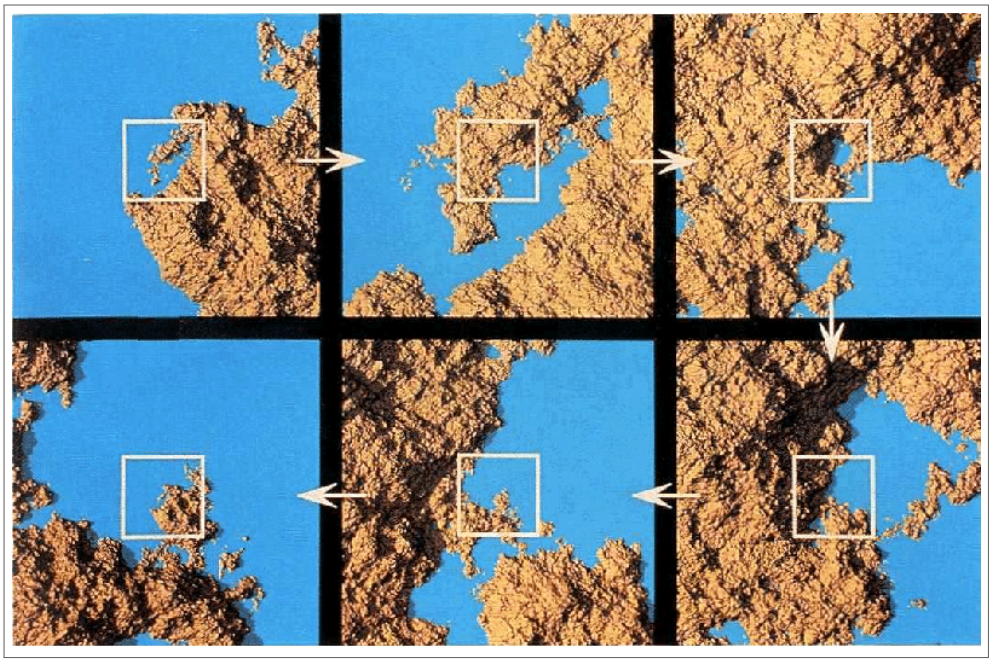

Source: (PÁSZTO; MAREK; TUCEK, 2011)

Scale invariance is an ubiquitous phenomenon in nature (one illustration is shown in Fig. 4). From a physics perspective, it is closely related to second order (or continuous) phase transitions, which are characterized by a sudden change in the state of a system. Specifically, they are quantified by an order parameter (e.g. the density difference between liquid and vapor, in a liquid-vapor transition, or the magnetic moment orientation of a magnet, in a para-ferromagnetic transition) in function of its control parameter (such as temperature of the system). A second order phase transition, where the order parameter changes continuously between phases, happens at a specific point of the control parameter vs. order parameter space — the critical point — and is often accompanied by the breaking of a symmetry of the system (REICHL, 1998).

Figure 5 shows the classic example of the Ising model of a magnetic system. In this case, each site in a regular lattice has a spin (magnetic moment) which may be oriented up or down. Each site interacts with its nearest neighbors, and temperature T is a control parameter governing the overall disorder of the system (Fig. 5A). For a sufficient decrease in temperature (below a critical point T_C), the cohesion between neighbors overcomes thermal fluctuations and the system goes from a disordered to an ordered phase (Fig. 5B).

The critical point is where scale-invariant properties come into play. In its vicinity, it is possible to obtain a set of observables whose behavior scales with power laws, each one providing an associated critical exponent (Fig. 5D). More importantly, the theory of phase transitions predicts the existence of **universality**. At the transition, scale invariance sweeps away the memory of the underlying microscopic details of the system (WILSON, 1975; KADANOFF, 2009; TONG, 2017). Its classification — that is, its set of critical exponents — is then determined solely by its essential features. A large number of very different systems fall into only a handful of universality classes, defined by their dimensionality and symmetries. The theory of critical phenomena provides the ability to extract simple, general principles and make predictions without needing to consider all the greedy details of each individual system and is one of the great successes of 20th century physics. It also remains relevant in contemporary research, as scientists find ways to continuously extend its framework to more complex systems, like we will see throughout this study.

1.2.1.2 Why would brains be critical?

The results from Beggs and Plenz not only underscored the presence of scale-free fluctuations in neuronal spontaneous activity but also revealed scaling exponents consistent with those of a system within a specific universality class, called mean field directed percolation (MF-DP). It governs transitions between an absorbing state, which dampens any activity in the system down to zero, and an active one, characterized by sustained activity. For instance, it can be related to a branching (or contact) process, a class of models where the branching ratio σ between successive iterations of the process is a control parameter that divides the absorbing and active regimes at $\sigma = 1$ (MARRO; DICKMAN, 1999).

With the perspective of providing an unifying framework for neuronal dynamics, Beggs and Plenz breakthrough led to an avalanche of follow-up works. Such research contributed to the foundation of what we refer to as *the critical brain hypothesis* (BEGGS, 2007; SHEW;

Figure 5 – Phase transition of the Ising model.(A) Nonzero macroscopic magnetization m can only be observed below a critical value T_C of the temperature. (B) This point also divides two qualitatively different behaviors of the system. In the vicinity of the critical point, the system (C) exhibits scale-invariant properties, (D) whose fluctuations are described by critical exponents from power laws distributions (both axes are logarithmic).

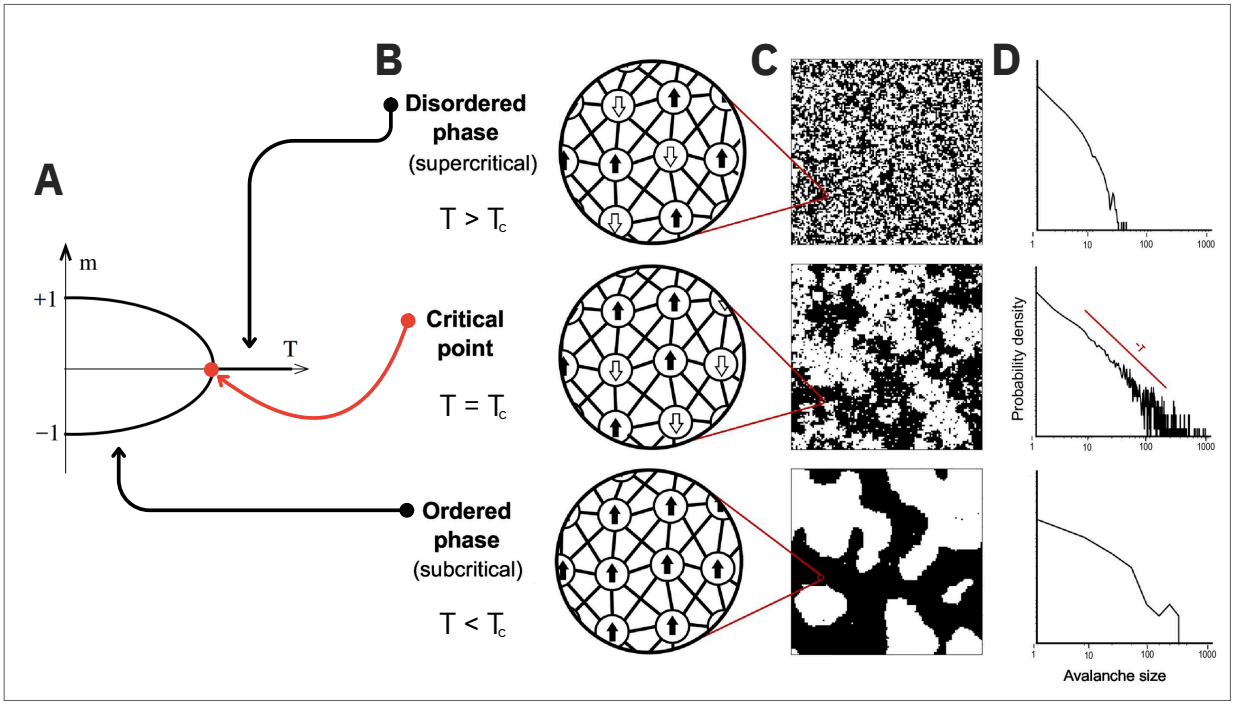

Source: Adapted from (O'BYRNE; JERBI, 2022)

PLENZ, 2013; PLENZ; NIEBUR, 2014; TOMEN; HERRMANN; ERNST, 2019; O'BYRNE; JERBI, 2022), which has been intensively explored theoretically (DE ARCANGELIS; PERRONE-CAPANO; HERRMANN, 2006; KINOUCHI; COPELLI, 2006; LEVINA; HERRMANN; GEISEL, 2007; LEVINA; HERRMANN; GEISEL, 2009; FRAIMAN et al., 2009; BONACHELA; NOZ, 2009; BONACHELA et al., 2010; LARREMORE; SHEW; RESTREPO, 2011; COSTA; COPELLI; KINOUCHI, 2015; CAMPOS et al., 2017; SCARPETTA et al., 2018; SANTO et al., 2018; KINOUCHI et al., 2019; KINOUCHI; PAZZINI; COPELLI, 2020; CANDIA et al., 2021; CARVALHO et al., 2021; NANDI et al., 2022; PIUVEZAM et al., 2023) and investigated in a variety of experimental setups (BEGGS; PLENZ, 2004; HALDEMAN; BEGGS, 2005; STEWART; PLENZ, 2006; PLENZ; THIAGARAJAN, 2007; PASQUALE et al., 2008; SHEW et al., 2009; PETERMANN et al., 2009a; RIBEIRO et al., 2010; LOMBARDI et al., 2012; TAGLIAZUCCHI et al., 2012; YANG et al., 2012; PALVA et al., 2013; SHRIKI et al., 2013; GAUTAM et al., 2015; SHEW et al., 2015; ZHIGALOV et al., 2015; FONTENELE et al., 2019; MILLER; YU; PLENZ, 2019; LOTFI et al., 2020; LOTFI et al., 2021; CAPEK et al., 2023; FONTENELE et al., 2024; CASTRO et al., 2024) in the last couple of decades. Amongst the brain areas, the cerebral cortex stands out as a key area of interest in investigating the critical brain hypothesis, with special attention to the pri-

mary sensory cortices (BEGGS; PLENZ, 2003; RIBEIRO et al., 2010; FRIEDMAN et al., 2012; SHEW; PLENZ, 2013; FONTENELE et al., 2019; CHEN; SCHERR; MAASS, 2022). Such cortical regions are essential for encoding sensory information from environmental stimuli. (KAAS; COLLINS, 2001).

This interest is not accidental. If nature were to select critical behavior as a desirable feature for brain design, it should come with evolutionary advantages. And this is indeed the case, as critical dynamics do offer an efficient solution to several requisites for sensory function. Here, we focus on three main axes: sensory range, information transmission and information capacity (SHEW; PLENZ, 2013).

The sensory range Δ is the range of input intensities a system is able to "distinguish", that is, to produce different outputs from. This is measured by the response curve of the system given an external stimulus. In biology, response curves often have sigmoidal shape: for weak stimuli, the system won't be excited enough to produce meaningful response; on the contrary, its response saturates for excessively strong forcing (Fig. 6A). To study how criticality affect response curves, Kinouchi and Copelli simulated a celular automata model belonging to the MF-DP universality class. By tuning the model's control parameter, the branching ratio σ (*i.e.* the average number of secondary spikes caused by an initial one), they showed that the regime that maximizes the dynamical range of the response curve is precisely at the phase transition between the absorbing and active phases of the model. The critical point would thus be a balance between being sensitive enough to perceive small stimuli whilst preventing the system going into overdrive. This was later verified experimentally in *in vitro* cell cultures, by pharmacologically manipulating the setup to control the system's closeness to criticality (SHEW et al., 2009).

The other two properties were also investigated both computational and experimentally (SHEW; PLENZ, 2013). The fidelity of information transmission is generally quantified by measuring mutual information between the set of different stimuli and the set of corresponding outputs (GREENFIELD; LECAR, 2001; SHEW et al., 2011). In a sense, it is similar to the sensory range, but captures the ability of the network to produce spatially accurate output given diverse patterns of stimuli. Again, information transmission peaks at the critical point of the system. In the same setup as the previous result (SHEW et al., 2011), Shew and collaborators found that the quantity of possible response spatial patterns — the information capacity, as quantified by Shannon entropy — is also maximized at criticality.

In summary, there is an increasing body of evidence that not only brain dynamics exhibit critical dynamics, but that it is meaningful and evolutively advantageous to brain function.

Figure 6 – Systems at criticality have optimal dynamic range. (A) Different response functions F for different values of the model's control parameter σ, the branching ratio. The dynamic rage is defined as the range of the function above the 10% percentile and below 90%.(B) Dynamic range Δ as a function of σ, peaking at $\sigma_C = 1$. (C,D) Same as (A,B), but for experimental *in vitro* results from cell cultures. The control parameter in this case is modulated by drugs that the excitation/inhibition balance of the culture.

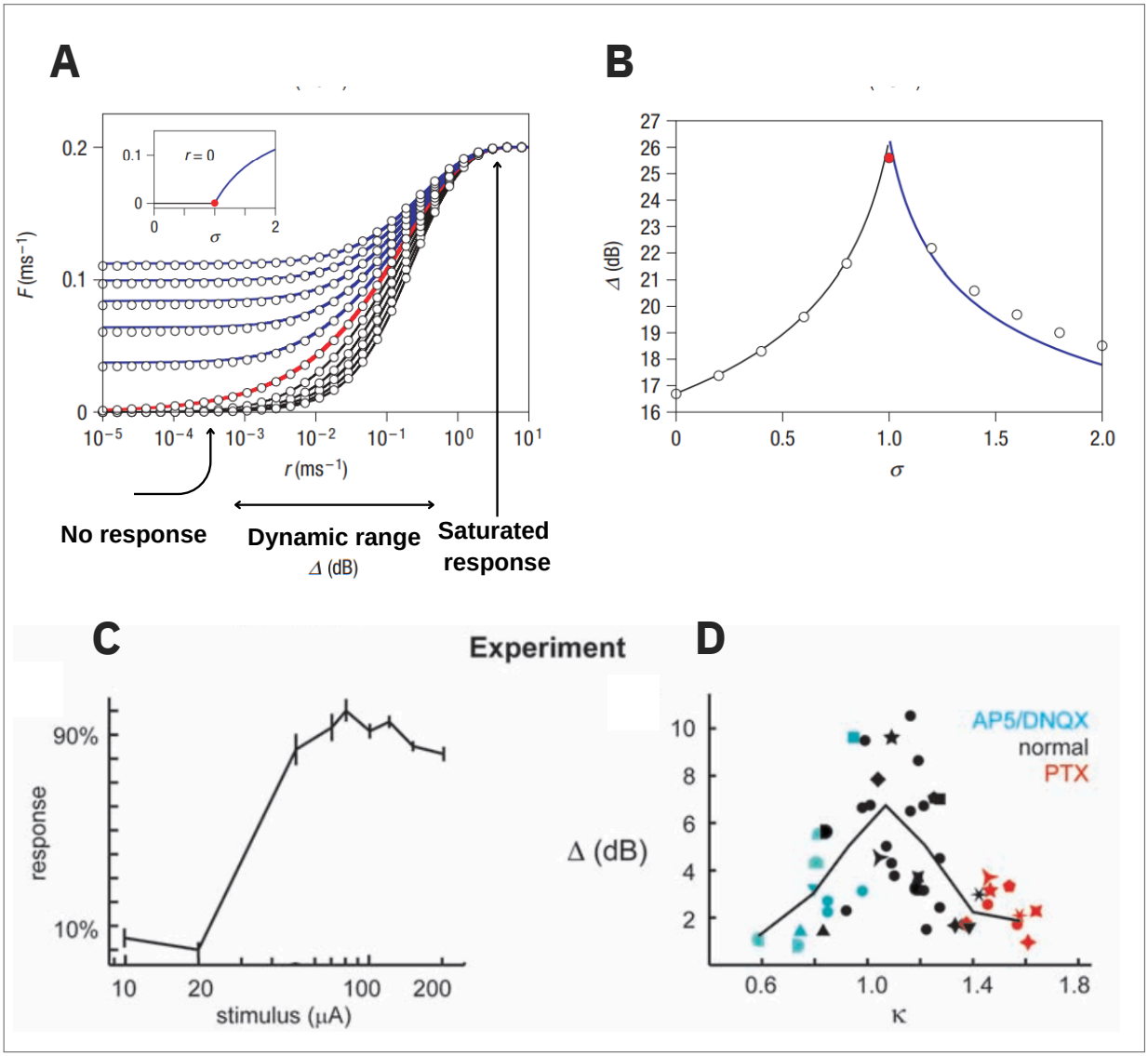

Source: adapted from (KINOUCHI; COPELLI, 2006; SHEW; PLENZ, 2013)

Nevertheless, a proper classification of the putative phase transition is still pending. Candidates other than the MF-DP transition also found place in the hypothesis, such as the edge-of-chaos transition (see Fig. 7), and alternative explanations can now be found in the literature (POIL et al., 2012; DALLA PORTA et al., 2019; FONTENELE et al., 2019; DAHMEN et al., 2019; MORRELL; SEDERBERG; NEMENMAN, 2021; O'BYRNE; JERBI, 2022). We will cover this discussion in more detail in the upcoming sections.

Figure 7 – Summary of the functional benefits of (A) avalanche (AC) and (C) edge-of-chaos (EOC) criticality. (B) Schematic for the propagation of signals across the brain. Avalanche criticality balances between neither dampening nor amplifying a signal across its trajectory, while EOC avoids diverging and converging trajectories.

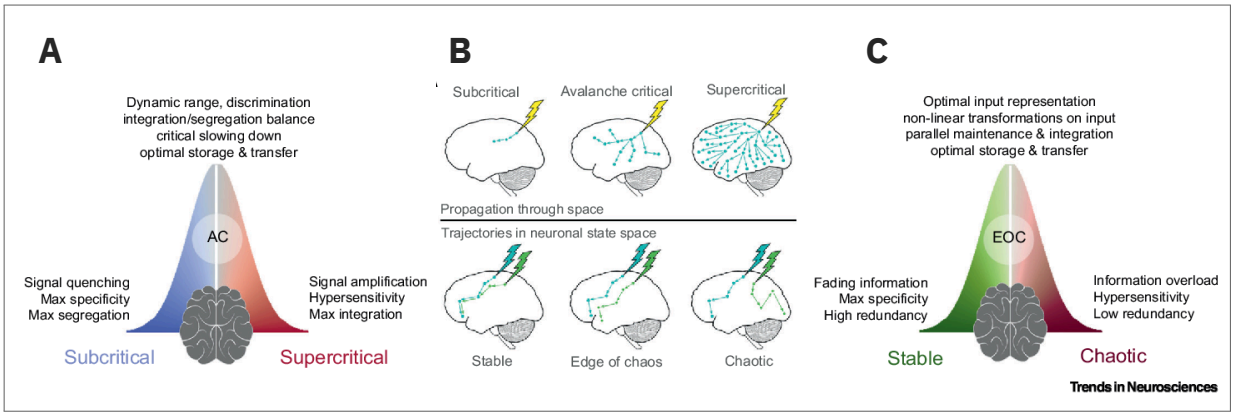

Source: adapted from (O'BYRNE; JERBI, 2022)

1.2.2 The rise and fall (and rise?) of mean-field directed percolation

Throughout the last two decades, advancements in simultaneous recordings of a large number of neurons have propelled the exploration of the critical brain hypothesis at the neuronal population level. This technological development is particularly relevant if one wishes to test criticality in scenarios more representative of biological reality than *in vitro* cell cultures. After all, if support for the hypothesis comes from its alleged computational advantages to perception and task performance, signatures of the proximity to a critical point should be the most visible precisely in this kind of situation.

But, in practice, results in this direction were not so straightforward. First, critical exponents measured in various experimental setups were not necessarily consistent with the MF-DP class. In fact, exponents often varied considerably between different subjects or in different realizations of the same setup or, in some cases, were not found at all (PRIESEMANN; MUNK; WIBRAL, 2009; RIBEIRO et al., 2010; PRIESEMANN et al., 2014; SCOTT et al., 2014; BELLAY et al., 2015; FONTENELE et al., 2019). The exact reason why results are not always compatible with each other is generally unclear, given the amount of specificities of each experiment (O'BYRNE; JERBI, 2022), added to the obvious limitations on reproducibility imposed by the fact that two living beings are not exact copies of each other.

To give a single example, consider the analysis conducted by Ribeiro *et al.* (RIBEIRO et al., 2010) on freely behaving rats, using multielectrode arrays to record the hippocampus (HP) region and primary visual (V1) and somatosensory (S1) areas of the cortex. Employing an

Figure 8 – Absence of scaling exponents in data from awaken rats. (A) Recordings of freely-behaving rats with multielectrode arrays in primary visual (V1) and somatosensory (S1) cortices and the hippocampus (HP). In the columns, plots are separated by experiment stages: before (PRE), during (EXP) and after (POST) the animals are exposed to a new object. Different colors denote data from different phases of the sleep cycle, from waking (WK) to slow-wave sleep (SWS) and rapid-eye-movement (REM) sleep. Grey lines show best curve adjustments, which in all case were a lognormal distribution. (B) Power law distributed avalanchehs in a celular automata model also shrink to a lognormal distribution, when the fraction of observed units is small (inset). (C) Avalanche distributions are well fit by power laws, but exponents vary according to brain region. Inset shows that scaling exponents from the model also vary in function of the sumbsampling rate. Different parameters were chosen in order to mimic anesthesia dynamics in the model.

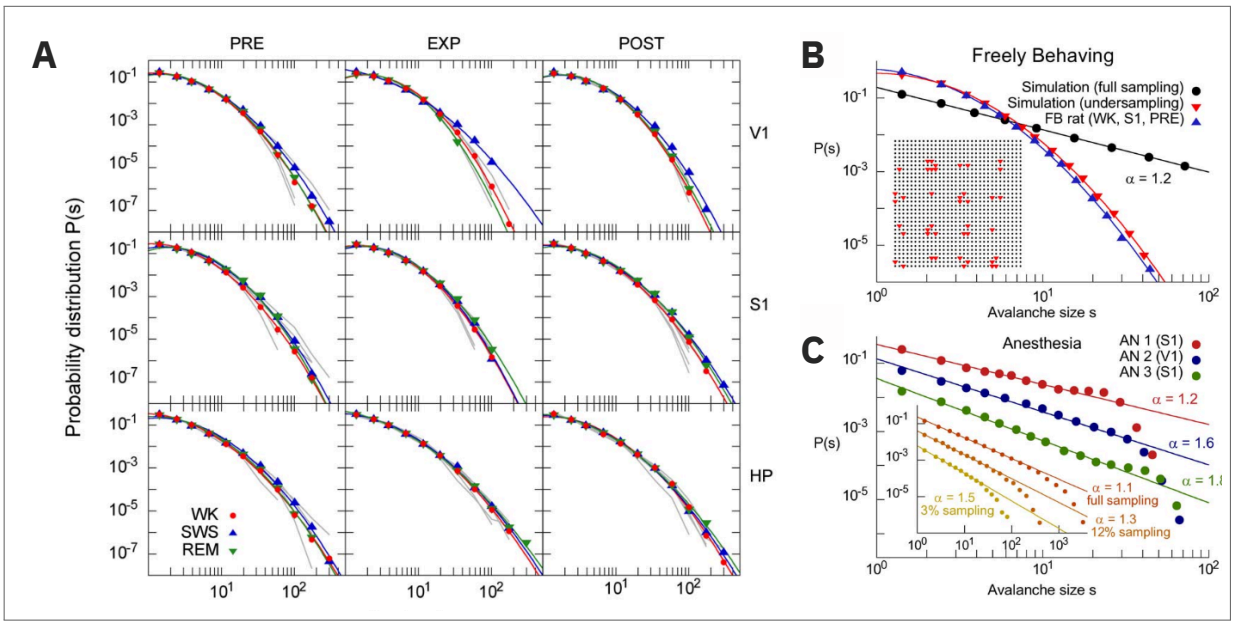

Source: Adapted from (RIBEIRO et al., 2010)

avalanche analysis similar to the one from Beggs and Plenz, they were the first to investigate criticality across the sleep-wake cycle. In their work, the distributions of avalanche sizes were remarkably stable across all three brain regions and different stages of the sleep cycle. But they were not power law distributed: instead, a (non-critical) lognormal curve was consistently found in all situations (Fig. 8A) except for (ketamine-xylazine) anesthetized animals [1](Fig. 8C).

To explain this result, authors used a model of cellular automata of the directed percolation class. Tuning the model at its critical point, they showed that lognormal avalanche distributions take place over power laws when only a very small fraction of the entire system is being observed (RIBEIRO et al., 2010). Indeed, this was — and, in general, still is — a limitation for the analysis of neuronal spiking data. The area around the electrode arrays of the experiment had about two orders of magnitude more neurons than what was recorded (between $10^1 - 10^2$

[1] As an example of how conflicting results are commonly found in the field, the opposite trend was later found in Scott *et al.* (SCOTT et al., 2014) (from voltage imaging data) and Bellay *et al.* (BELLAY et al., 2015) (from spiking data). Under pentobarbital and isoflurane anesthesia, power law distributions in activity were destroyed, and posteriorly recovered when the effects of the drugs wore off.

neurons), resulting in a severe rate of subsampling. In conclusion, power law distributions with the correct exponents should be recovered when observing a sufficient fraction of the system's total population.

This is only one of the technical obstacles in the task of understanding scaling in neuronal populations. To obtain results inspired by statistical mechanics in biological data, one has to consider several factors that were not an issue in original theories: besides subsampling (PRIESEMANN; MUNK; WIBRAL, 2009; RIBEIRO et al., 2010; CARVALHO et al., 2021), scaling exponents are also affected by the choice of temporal resolution used to bin neuron spikes (discrete events) (BEGGS; PLENZ, 2003; PETERMANN et al., 2009a; FONTENELE et al., 2024; CASTRO et al., 2024; SRINIVASAN et al., 2024) (inset in Fig. 3C) and the non-stationarity of the system's statistics caused by the current behavioral state of a subject (FONTENELE et al., 2019; CARVALHO et al., 2021; CASTRO et al., 2024). Some methods were developed to reconcile such apparent contradictions with theory (PRIESEMANN; MUNK; WIBRAL, 2009; PETERMANN et al., 2009a), but a definitive way to measure the "true" scaling exponents while accounting for all these factors is currently still lacking.

1.2.2.1 Alternative explanations to scale invariance

With the unresolved scenario regarding the nature of the putative phase transition governing brain dynamics, several alternative explanations to the observation of neuronal avalanches were proposed (TOUBOUL; DESTEXHE, 2017; FONTENELE et al., 2019; DAHMEN et al., 2019; MORRELL; SEDERBERG; NEMENMAN, 2021; O'BYRNE; JERBI, 2022). Between the proposed solutions, the most antagonistic to the MF-DP hypothesis is the one by Touboul and Destexhe (TOUBOUL; DESTEXHE, 2010; TOUBOUL; DESTEXHE, 2017; DESTEXHE; TOUBOUL, 2021). In their works, criticality signatures found in brain data are argued to be an epiphenomenon of brain dynamics, which they support by providing examples of stochastic systems that, with the right parameters, can also exhibit scale-free fluctuations. Importantly, these counterexamples showed that the mere presence of avalanches with scaling exponents is not sufficient condition to determine a phase transition. This raised the standards of future works in the area, which then implemented more stringent tests for criticality (Sec. 1.2.2.2).

Another interpretation of the phenomenon involves Griffiths phases. In some disordered systems, heterogeneity works in a way that local parameter values may be significantly different from the global average. When this happens, activity can propagate through abnormally active

Figure 9 – Griffiths phase in hierarquical-modular networks. (A) Initially, nodes are grouped into fully connected modules of size M_0 (blue squares); then nodes in different modules are clustered recursively into sets (in this example, pairs) of higher level blocks following level-dependent wiring probabilities: $p_l = \alpha p^l$ with $0 < p < 1$ and constant α. (B) Graph representation of a network with $N = 211$ nodes, organized across $s = 10$ hierarchical levels ($M_0 = 2$, $p = 1/4$, and $\alpha = 4$). (C) Regular phase transition diagram with a critical point λ_c, in contrast to (D) a system exhibiting a Griffiths phase. (E) Single scaling exponent from the critical point in a Erdős–Rényi (ER) random network. (F,G) Power laws with continuously varying exponents in hierarquical-modular networks (HMN)

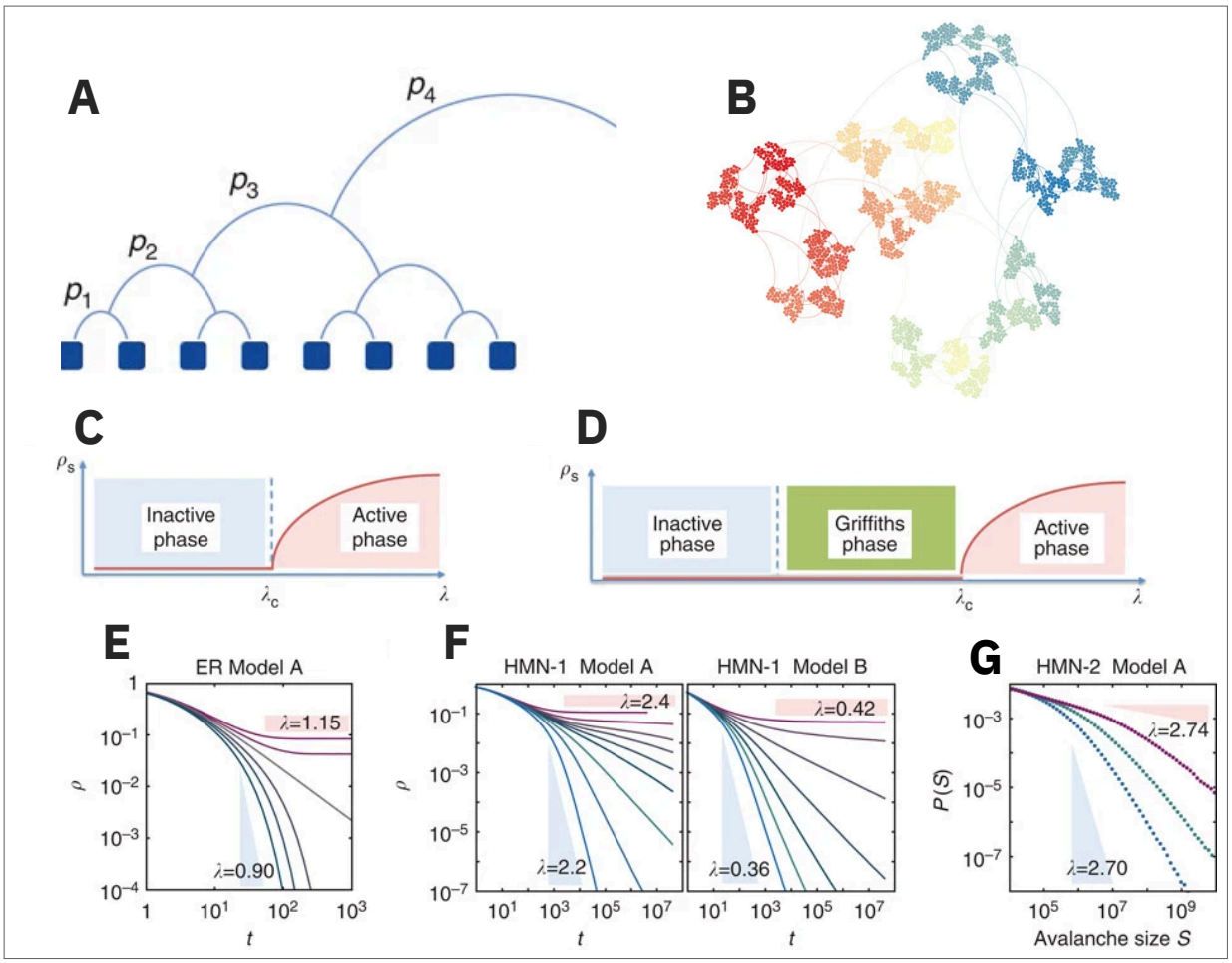

Source: Adapted from (MORETTI; MUÑOZ, 2013)

regions even in the inactive phase. As a consequence, the usual critical point dividing the system's phase gives place to an entire region in parameter space — the Griffiths phase — with continuously varying scaling exponents (Fig. 9C-9G).

Moretti and Muñoz (MORETTI; MUÑOZ, 2013) showed that, in a contact process model (MARRO; DICKMAN, 1999), defining the structure of the network as a hierarchical-modular setting (Fig. 9A-9B) (which is found in the functional brain networks of the *C. elegans* and human fMRI data) introduces disorder in a way that a Griffiths phase is obtained.

Some alternative explanations to scale invariance in brain data still involve phase transitions, but of a different nature. In the next section, we will see how, by studying neuronal avalanches

across different regimes of cortical activity, evidence for a phase transition not belonging to the MF-DP universality class was found (FONTENELE et al., 2019). The following narrative is particularly relevant for the results of this thesis in later chapters.

1.2.2.2 Criticality between cortical states

The brain operates in a state of constant neural activity, displaying a wide range of different dynamical states. Even in the absence of external stimuli or behavioral tasks, the statistics of cortical activity stays non-stationary. Initially observed in whole-brain electroencephalographic recordings (BUZSAKI et al., 1988), this non-stationarity has been explored in experiments of neuronal population as a means to classify different behavioral states in animals (RENART et al., 2010; HARRIS; THIELE, 2011). In such studies, this was achieved by quantifying variability levels from spiking activity. Specifically, they measured the population firing rate coefficient of variation (CV), defined as

$$CV_j = \frac{\sqrt{\langle \rho^2 \rangle_j - \langle \rho \rangle_j^2}}{\langle \rho \rangle_j} \tag{1.3}$$

for a given time window j. Here, $\rho(t)$ is the "instantaneous" firing rate of a neuron in the population and angle brackets denote time averages (RENART et al., 2010; HARRIS; THIELE, 2011). In freely behaving animals, cortical activity spontaneously drifts between more desynchronized states (characterized by lower CVs), during awake and alert behavior, and more synchronized states at high CVs, observed in drowsiness and slow-wave sleep (CLEMENT et al., 2008; HARRIS; THIELE, 2011). Hence, the level of spiking variability has been used as a proxy for cortical states (SOFTKY; KOCH, 1993; HOLT et al., 1996; NAWROT et al., 2008; RENART et al., 2010; HARRIS; THIELE, 2011; SCHÖLVINCK et al., 2015).

A few years ago, Fontenele and collaborators (FONTENELE et al., 2019) proposed to consider the effects of different cortical states in criticality analysis. To do so, they used recordings of spontaneous activity from deep layers of the primary visual cortex (V1) of $n = 8$ urethane-anesthetized rats with silicon probes (at the time, a state-of-the-art technology for high-density recordings of spiking activity (JUN et al., 2017)). The benefits for this kind of setup is twofold: first, it allows for very long recording sessions ($\geq$ 200 min). The characteristics of urethanized activity also mimic those seen in spiking-evoked activity within the sensory cortex of freely moving animals, as particularly noticeable in V1 (TSODYKS et al., 1999; RINGACH, 2009; PETERMANN et al., 2009a; RIBEIRO et al., 2010).

Figure 10 – Cortical dynamics at different levels of spiking variability. (A) Illustration of the point where probes are inserted in the primary visual cortex (V1) (left). Electrode locations within the probe (top right) and sample spiek waveforms (bottom right). (B) Coefficient of variation (CV) over time for a single animal. (C) Raster plots of different 4 s windows: each line correspond to a neuron, with dots depicting spike timings along the time window. Periods with low CV (left) exhibit mostly asynchronous activity, while during higher CV windows (right) neurons fire synchronously. Lines are population rates smoothed by a gaussian kernel $\sigma = 0.1$ s. (D) Histogram of spike timing pairwise correlations in the three representative time windows shown in (C).

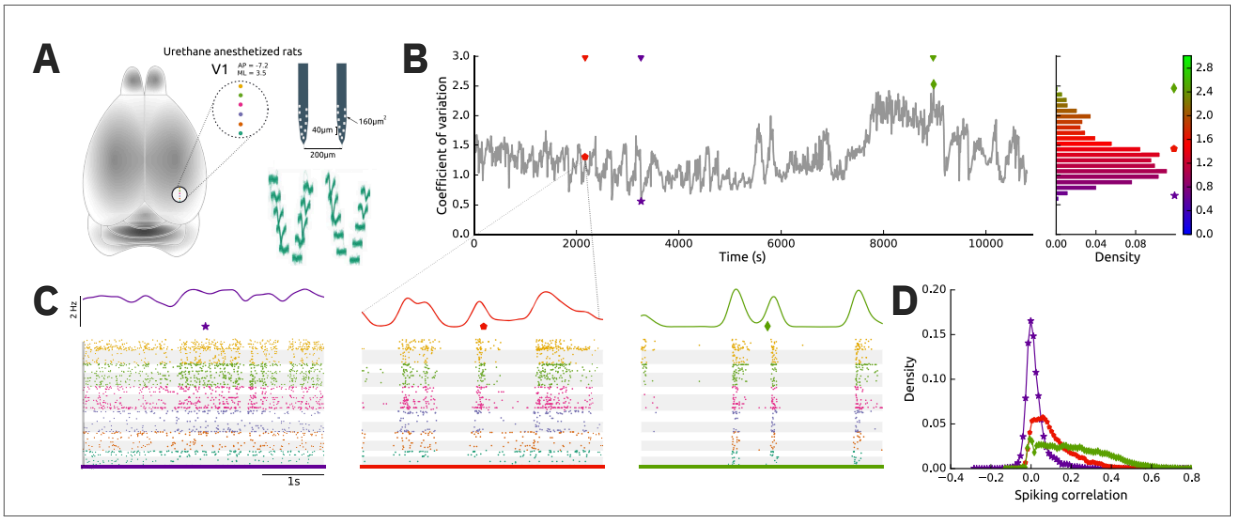

Source: adapted from (FONTENELE et al., 2019)

The analysis by Fontenele *et al.* was the following: they began by partitioning the data in small segments, where the signal's covariance is approximately stationary (in their case, 10-s windows). Then, they found adjustments for avalanche distributions within each time window. Since avalanche size and duration exponents τ, τ_t are not sufficient conditions to infer criticality (TOUBOUL; DESTEXHE, 2010; DESTEXHE; TOUBOUL, 2021) a more stringent test was used. The theory of critical phenomena states that, if both exponents τ, τ_t hold, so should hold the relation between sizes given a duration $\langle S \rangle (T) = T^{\frac{1}{\sigma \nu z}}$ (Fig. 11C) (FRIEDMAN et al., 2012). This exponent is then used in the left side of the so called *crackling noise relation* (SETHNA; DAHMEN; MYERS, 2001)

$$\frac{1}{\sigma \nu z} = \frac{\tau_t - 1}{\tau - 1}, \tag{1.4}$$

Which has not been observed in systems away from a phase transition (TOUBOUL; DESTEXHE, 2017).

By showing in the same graph each side of Eq. 1.4 as a function of the CV value of the window, authors found that the scaling relations could only be found within a narrow range of CVs (Fig. 11D). These results suggests that, if we think of CV as a control parameter, we can see a critical point in an intermediate value of $\langle CV \rangle \simeq 1.4 \pm 0.2$ (Fig. 11E). Over time, the

system fluctuates largely around this critical region. Still, it would stay most of its time in the vicinity of the critical point, as evidenced by the residence time distribution of CVs (dashed line in Fig. 11E).

Moreover, they compared the relation between the τ and τ_t exponents not only across anesthetized rats, but also other 4 types of experiments — including mice, turtles, monkeys and cell cultures — and a model (Fig. 11F) (KOHN; SMITH, 2016; SENZAI; FERNANDEZ-RUIZ; BUZSÁKI, 2019; FRIEDMAN et al., 2012; SHEW et al., 2015; DALLA PORTA et al., 2019) Remarkably, not a single setup of the list exhibited exponent relations compatible with the mean-field directed percolation class (black dot in Fig. 11F). Exponents were instead linearly spread along the exponent plane, with the adjusted slope of $\frac{\tau_t - 1}{\tau - 1} = 1.28$.

The model which falls into the same slope as the experiments is precisely the "CRitical OScillations" (CROS) model (POIL et al., 2012). This model was an attempt to unify two hallmarks of criticality, scale-invariant avalanches and long-range temporal correlations[2]. Despite achieving good agreement with the exponents observed experimentally, it is unknown whether the model has a true critical point or undergoes some different kind of transition phenomenon (DALLA PORTA et al., 2019). Nevertheless, it further suggested that the nature of the phase transition measured in data may not be between absorbing and active states. Rather, it could be a transition between an active phase and oscillating one. These results challenged what had been the main theoretical paradigm used in the field for almost twenty years, while raising questions of what would then be the minimal model capable of reproducing all the experimental results.

Shortly after, such minimal model was proposed by Carvalho *et al.* (CARVALHO et al., 2021). But, perhaps surprisingly, the answer did not come from a different universality class. The model chosen was the Gerstner-Galves-Löcherbach (GGL) model, which belongs yet again to the MF-DP universality class (GIRARDI-SCHAPPO et al., 2020). This model is a network composed of populations of excitatory and inhibitory neurons, with all-to-all connections, *i.e.* connected in a complete graph. In essence, it works similar to common "integrate-and-fire" models[3] with the key difference that stochasticity is introduced in a particular manner. Its

[2] Notice that these two signatures may seem contradictory at first. Theoretically, avalanches in models exhibit infinitely separated timescales: once an avalanche ends, there is no activity and the system needs to be reset. For a system to display both phenomena, the definition of avalanche needs to be adapted. The proposed solution by the CROS model is to define them as supra-threshold collective activity.

[3] Integrate-and-fire models are a class of simplified mathematical models for neurons and neuronal networks. They abstract away many of the detailed mechanisms involved in neural signaling but capture the essential feature of neurons integrating inputs and generating output spikes, generally through linear differential equations or maps with an artificial reset point at the spike threshold. They are widely used for being

Figure 11 – Analysis of critical exponents subject to CV parsing. (A,B) Distributions for the size S (A) and duration T (B) (same examples as Fig. 10C). (C) Relation between size and lifetime of spike avalanches. (D) Scaling relations (from the exponents in (A-C)) across 10-s windows for five anesthetized rats, each represented by a different symbol. (E) Same as (D), averaging all group data. Shadows around lines are standard deviations, grey stripe marks the range where the crackling noise relation is satisfied. Dashed lines are relative residence times at each CV. (F) Linear relation between avalanche exponents for different experimental setups (KOHN; SMITH, 2016; SENZAI; FERNANDEZ-RUIZ; BUZSÁKI, 2019; FRIEDMAN et al., 2012; SHEW et al., 2015) and one model (DALLA PORTA et al., 2019). Black dot points the MF-DP universality class.

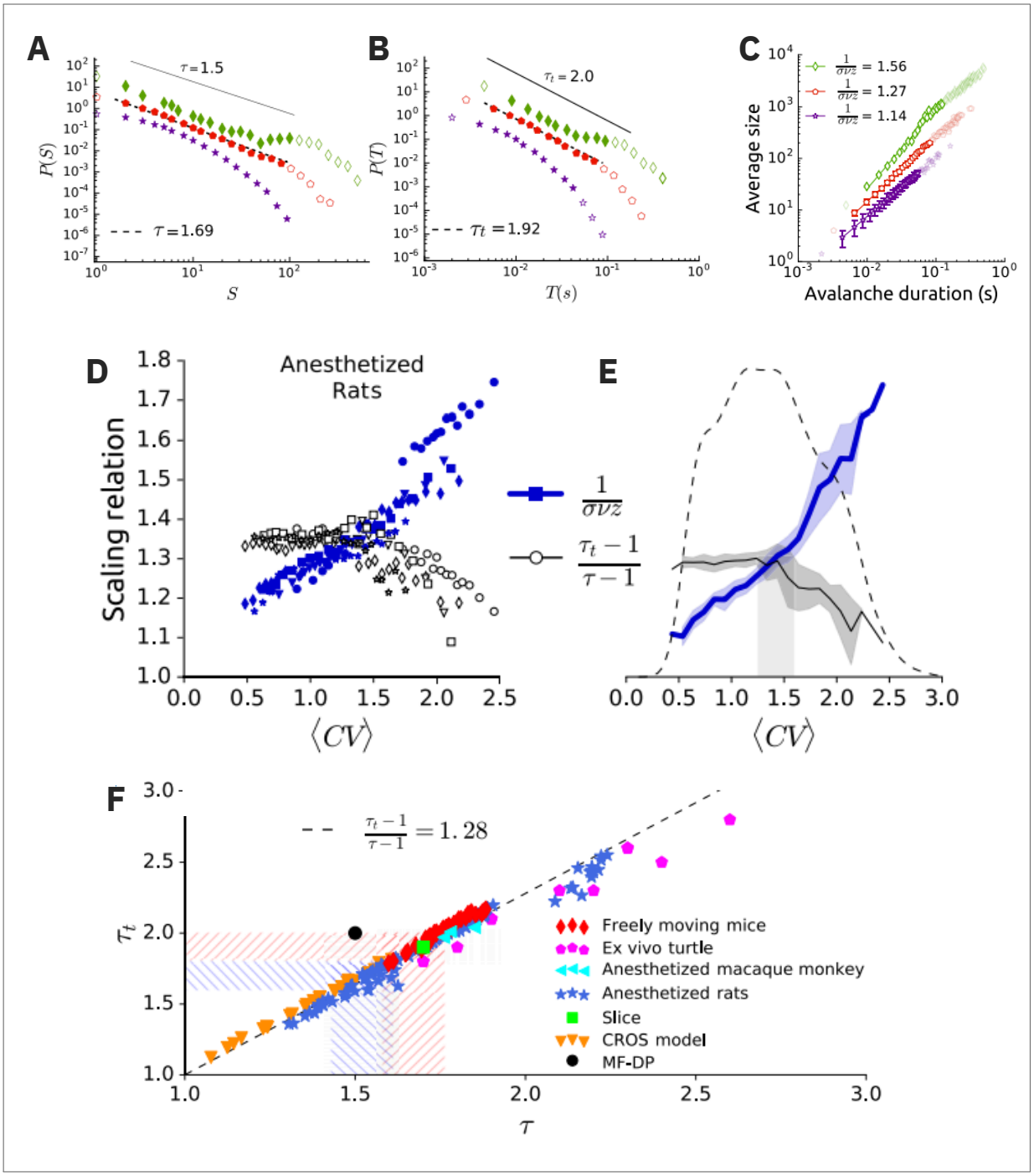

Source: adapted from (FONTENELE et al., 2019)

computationally efficient and allowing analytic results to be derived.

neurons fire a spike $X_i = 1$ according to a piecewise linear sigmoidal probability

$$P(X_i = 1 \mid V) = (V_i - \theta)\Gamma\Theta(V_i - \theta)\Theta(V_S - V_i) + \Theta(V_i - V_S) \tag{1.5}$$

where θ is the firing threshold, Γ is the firing gain constant, $V_S = 1/\Gamma + \theta$ is the saturation potential, $\Theta(x > 0)$ is the step function and V_i the membrane potential of neuron i, which evolves in time. For $\Gamma \to \infty$, the model becomes the traditional integrate-and-fire neuron network (GERSTNER, 2002).

Figure 12 – Directed Percolation model recovers results from CV parsed avalanche analysis when subsampled. (A) CV distribution over time from experimental data (FONTENELE et al., 2019). (B) Reproduction of the CV distribution using the GGL model. (C) Phase diagram of the density of firings $\bar{\rho}$ as a function of inhibition strength g (left) and sual MF-DP avalanche exponents for the fully sampled model (middle, right). (D) Scaling relations in the subsampled model ($n/N = 10^{-3}$). Under subsampling, results from (FONTENELE et al., 2019) are recovered within 3% of the critical parameter value. (E) Relation between avalanche exponents for different subsampling rates. for $n/N \to 1$, exponents depart from the linear relation found in data and converge to MF-DP values.

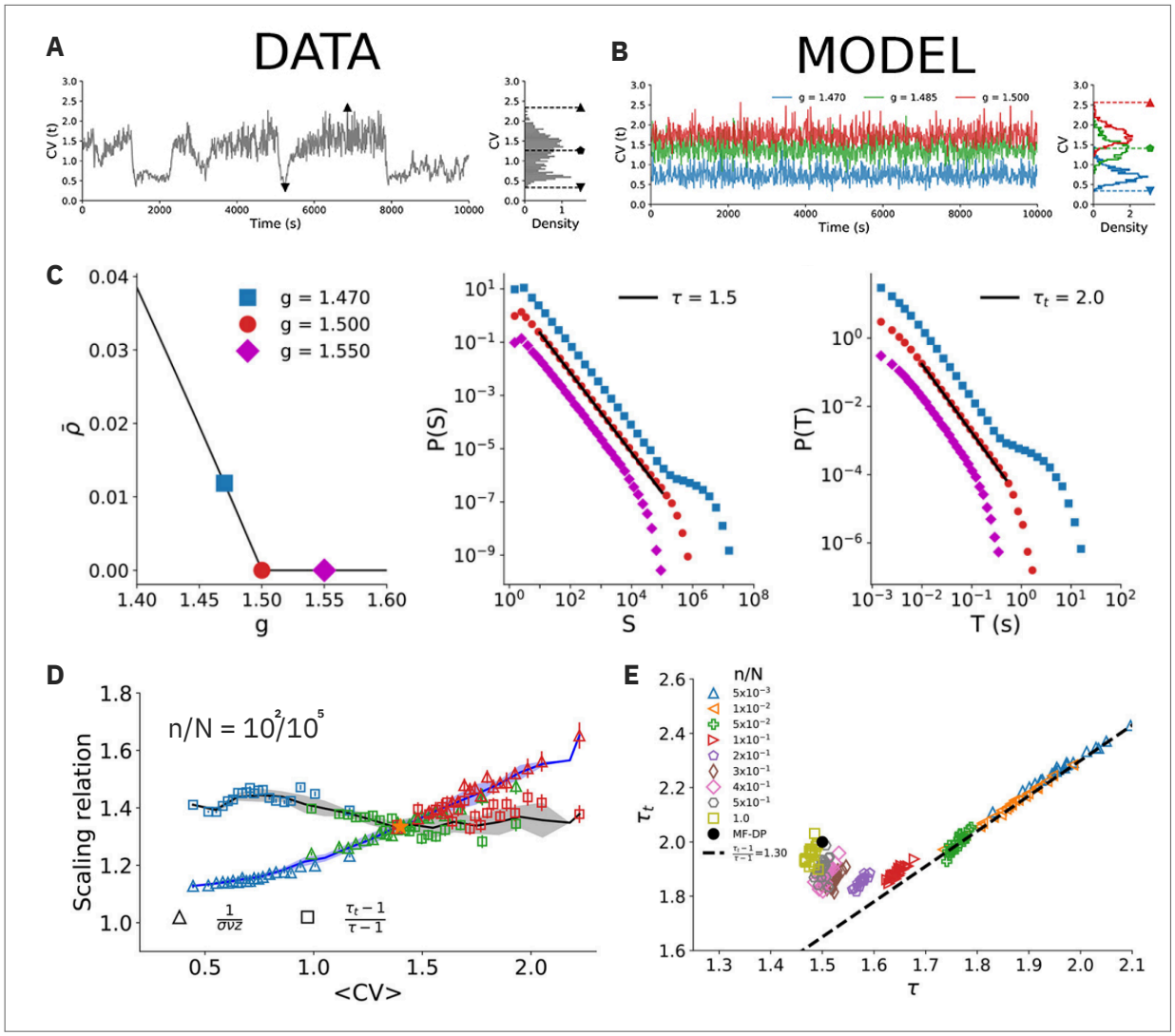

Source: adapted from (CARVALHO et al., 2021)

First, it was shown that most of the spectrum of spiking variability seen in the CV distribution of urethane experiments could be achieved with minimal deviations from the critical point of the model (Fig. 12A-12B). There, avalanche exponents have the usual MF-DP values (Fig. 12C), as expected analytically from the model. To obtain the experimentally observed variations in exponent values, the model did not require any additional features, but rather the introduction, this time intentional, of a familiar issue in criticality analysis: *subsampling*. When restricting the observation of the network to a small fraction ($n/N = 10^{-3}$) of the total number of neurons, exponents found within 3% of the critical parameter value could reconstruct all the scaling relations found in Fontelene *et al.* (Fig. 12D). This includes satisfying the crackling noise relation only at the narrow range of variability $CV \approx 1.4$. Furthermore, the entire line in the avalanche exponents plane followed by diverse data (Fig. 11F) could actually be reproduced by varying the level of subsampling in the exponent measurement (Fig. 12E). MF-DP values were recovered once we observed the full network again (CARVALHO et al., 2021), showing that the other values were indeed distortions caused by subsampling.

These results once more exposed the methodological frailty of relying exclusively on avalanche analysis to infer criticality in neuronal systems. They also underscored the need for developing additional ways to measure criticality.

1.2.3 A second type of criticality: on the edge of chaos

In the midst of the struggle to categorize the putative phase transition governing neural collective dynamics, researchers also sought for alternatives to the avalanche-counting framework in phase transitions studied outside of the statistical mechanics background. Recently, an approach proposed by Dahmen *et al.* (DAHMEN et al., 2019) caught the attention of the brain criticality community.

Initially, the authors noticed that, in multi-electrode array recordings of spiking activity in their experimental setup — from the macaque motor cortex — neurons seem to operate in a regime incompatible with those of avalanche dynamics: neural activity in the motor cortex is dominated by inhibition, leading to very weak pairwise correlations and fluctuations at the population level. Since it would not be operating at criticality, does that mean that the motor cortex is sub-optimal in terms of information processing?

To reconcile this apparent contradiction, authors show that it is possible to probe for a different kind of phase transition: an edge-of-instability (or edge-of-chaos) one. The intuition for

this type of transition is as follows: suppose we model a network of neurons whose interactions are mediated by a controlled connectivity matrix W. For weak connection strengths, most of the input received by a neuron j will come from the activity of other neurons i directly connected via W_{ij}. As connection strength grows, it creates a network of parallel pathways through which neurons interact, spreading indirect connections across multiple neurons. Consequently, neurons influence one another through many intermediate neurons, even in the absence of a direct connection W_{ij}, as illustrated in Fig. 13A.

Figure 13 – (A) Illustration of the indirect pathways through which a neuron may stimulate another for increasing synaptic weights w. (B) As the network approaches its unstable regime, bulk eigenvalues of its covariance matrix approach $Re(\lambda) = 1$. At the same time, the distribution of covariances c_{ij} (C,D) greatly increase its width δc_{ij}.

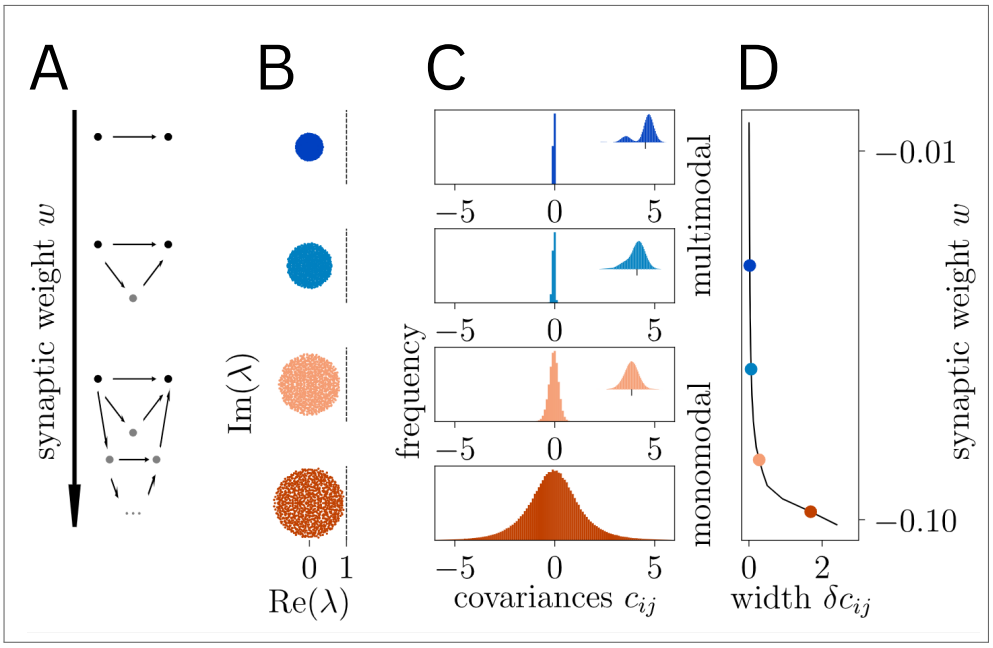

Source: Adapted from (DAHMEN et al., 2019)

The importance of indirect interactions can be quantified by the eigenvalues of the connectivity matrix. Since the contribution of an interaction with n intermediate neurons is proportional to W^n, an indirect path becomes comparable to direct ones when an eigenvalue of W reaches $Re(\lambda) = 1$ (DAHMEN et al., 2019). At this point, the network becomes unstable, and the distribution of covariances between neurons exhibit a large width and small mean (Fig. 13C).

This transition was already well known in computer science. A particularly convenient result from it is that, for a type of recurrent neural network framework (called reservoir computing), information storage and signal-to-noise ratio of network inputs are maximized at this transition (GREENFIELD; LECAR, 2001; O'BYRNE; JERBI, 2022). In order to put these ideas forward

in data analysis, the main obstacle is that one does not have direct access to the connectivity matrix. Hence, it is necessary to bridge the statistics of connections with the statistics of the data covariances, which can be calculated from spike trains.

Figure 14 – Closeness to the edge-of-chaos transition at $\lambda_{max} = 1$ in function of the network size. Shaded region shows the authors' estimation for a biologically plausible number of neurons around the electrode array.

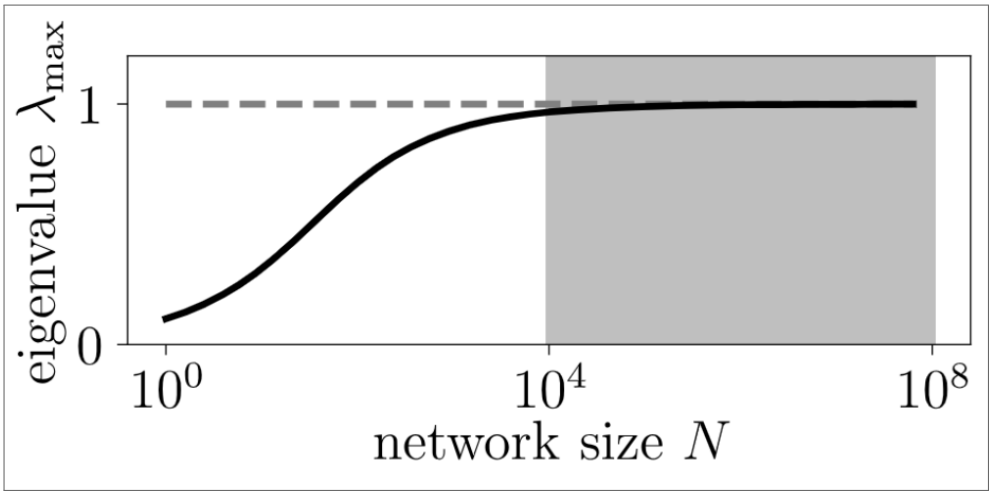

Source: Adapted from (DAHMEN et al., 2019)

For long observation times T, it is possible to connect spike count covariances and the integral of the time-lagged covariance function of a system (DAHMEN et al., 2019):

$$c_{ij} = \frac{1}{T}(\langle n_i n_j \rangle - \langle n_i \rangle \langle n_j \rangle) \xrightarrow[T\to\infty]{} \int_{-\infty}^{\infty} c_{ij}(\tau) d\tau, \tag{1.6}$$

where n_i is the number of spikes at site i over time and

$$c_{ij}(\tau) = \int_{-\infty}^{\infty} x_i(t) x_j(t-\tau) p(x_i, x_j) dx_i dx_j. \tag{1.7}$$

Employing a combination of spin-glass techniques with approximations for large-N field theories, Dahmen and collaborators could establish an analytical relation between the distance to instability λ_{max} and the width of spike count covariances $\Delta = \delta c_{ij}/c_{ii}$ distribution (Fig. 13). Namely,

$$\lambda_{max} = \sqrt{1 - \sqrt{\frac{1}{1 + N\Delta^2}}}. \tag{1.8}$$

With this result in hands, they inserted the empirical covariance width $\Delta = 0.15$ into the expression. They concluded that, assuming a biologically plausible value for $N > 10^4$

Figure 15 – Comparison between types of putative phase transition in neuronal data. Edge-of-chaos criticality is related to (A) a large distribution of possible covariances around zero, (C) many non-negligible covariance eigenvalues and (E) multiple eigenvectors with strong self-correlation in time. This is in contrast to avalanche criticality's (B) narrow covariance histogram, (D) single dominating eigenvalue and (F) eigenmode. Lines in (E-F) are from eigenmodes corresponding to the first, second and 20-th largest eigenvalues, from darker to lighter.

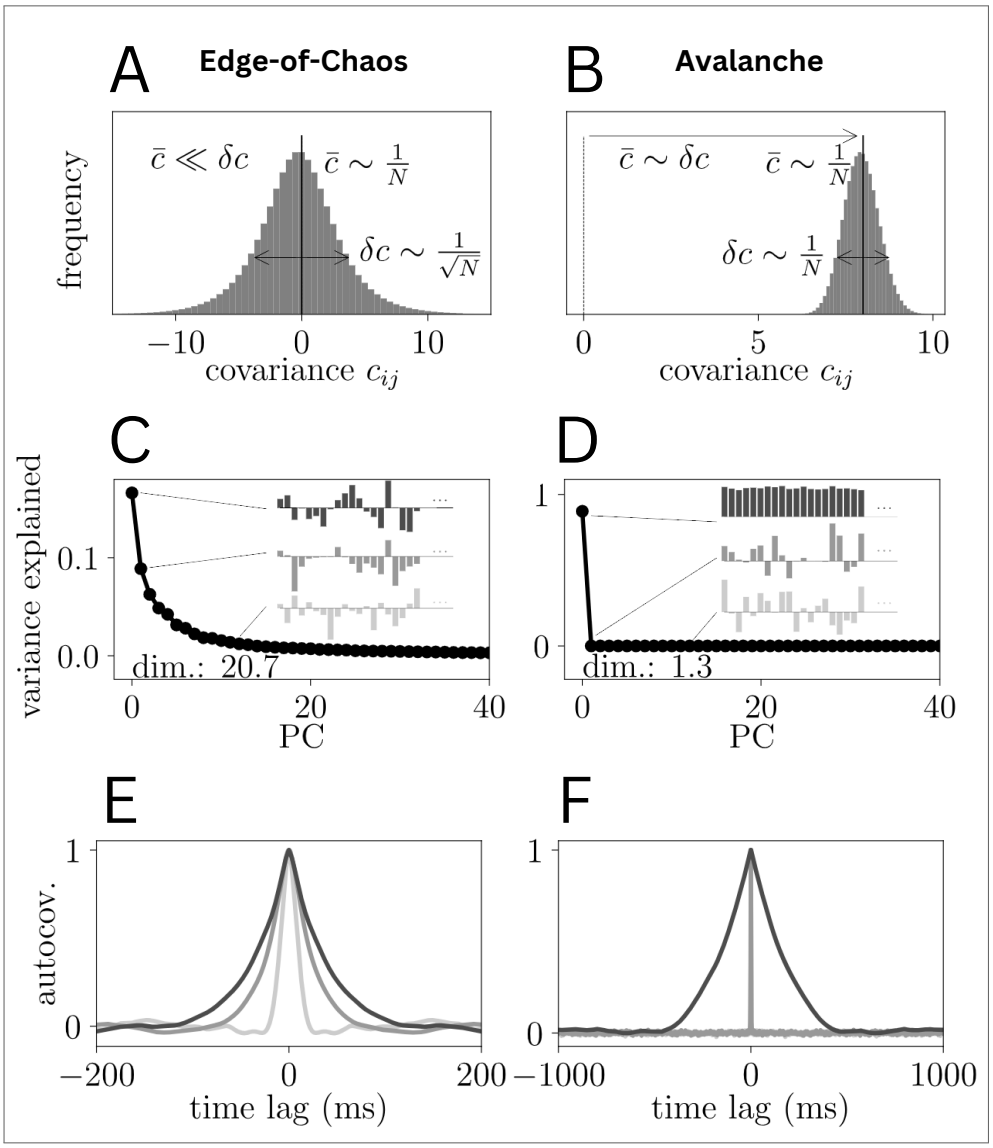

Source: Adapted from (DAHMEN et al., 2019)

— not directly measured by multi-electrode arrays, whose recordings capture an order of 100 neurons — neural activity from the macaque motor cortex operates near the edge of instability $\lambda_{max} \lesssim 1$, as shown in Fig. 14. Finally, authors catalogued how avalanche and edge-of-chaos differ statistically from one another. In regards to the distribution of covariances, the second type of transition yields a vanishing mean and large standard deviation, whereas the inverse is true for avalanche-type criticality (Fig. 15A-15B)). In the avalanche regime, a single covariance mode dominates the dynamics. At the edge of instability — also termed the "dinamically

balanced critical regime" — many different modes influence the system's dynamics. As a result, this case displays a continuum of significant eigenvalues and their corresponding modes, with many eigenmodes having long autocorrelation times (see Fig. 15C-15F).

Despite the contrast between the two critical states, one should not erroneously conclude that they are mutually exclusive. They are achieved through different mechanisms: avalanche criticality stems from a balance between excitation and inhibition in the neuronal population; for the dynamically balanced criticality, the spectral radius of the effective connectivity is pushed towards instability, guided by the heterogeneity of the network (DAHMEN et al., 2019). Moreover, the transition occurs in a direction of a high-dimensional neuronal state space. In this view, the population activity from which avalanche criticality is measured is simply a particular projection in this space. Thus, both regimes may coexist or alternate dynamically in order to adapt to specific brain tasks. Recent works from Fontenele *et al.* (**??**) show that neuronal avalanches and long-range temporal correlations happen in a small subspace of the high-dimensional dynamical space, while coexisting with a desynchronized subspace.

The work of Dahmen *et al.* were a step towards mathematically understanding criticality in dynamical systems, beyond the language of equilibrium statistical mechanics. This allowed them to capture critical properties in irregular asynchronous neuronal network states, where avalanche regimes from a branching process phase transition do not exist.

1.3 A PHENOMENOLOGICAL APPROACH

So far, we have provided context for the current status of brain criticality within neuroscience. In this section we arrive at the method that gives this work its title. First, we cover a brief historical introduction of the renormalization group (RG), the theoretical framework whose ideas inspire the phenomenological application presented here. To keep the text concise enough for this overview, detailed calculations to derive results from RG were ommitted; they can be easily found in standard texts in statistical physics[4]. Finally, we introduce the phenomenological method and explore how it has been utilized in the literature so far.

[4] See, for example, Linda Reichl's *Modern course in statistical physics* (2nd edition), chapter 8.C through 8.S.A (REICHL, 1998) for an introduction.

1.3.1 The Renormalization Group

The renormalization group stands as one of the most influential concepts in modern physics. It functions both as a conceptual and calculational tool, refining our understanding of critical phenomena, phase transitions, and the behavior of systems with many degrees of freedom across various scales.

Renormalization techniques made their debut in quantum field theory, to address the issue of ultraviolet divergences in quantum electrodynamics (QED). Developed in the 1940s and 1950s by Schwinger, Feynman, Tomonaga, Dyson, and others, it involves subtracting infinities from calculations in a consistent way to obtain finite results (TONG, 2017). Despite delivering results in great agreement with experiment, the process was poorly understood. The first step towards a stronger conceptual basis (and usage of a (semi-)group tool in the subject) was taken by Gell-Mann and Low in 1954. They recognized the possibility of defining an effective charge for the electron $e(\mu)$ through scale transformations, with μ representing the energy scale of the experiment. This effective charge transitions between the physical charge at low energy scales (as μ approaches zero) and the so called bare charge at high energies.

Simultaneously, statistical physicists in the 50s and 60s were long dealing with the challenge of understanding second-order (or continuous) phase transitions. Landau's "classical" theory was already known to fail at the critical point (DOMB, 1996), but solutions to this issue took decades to develop. Benjamin Widom was the first to demonstrate that, by invoking scale invariance, relationships between critical exponents could be derived, but with little insight into the origin of this scale invariance (TONG, 2017). This could be done by assuming that a singular part of the system's Gibb's free energy g_s — the one containing the relevant behavior of the phase transition — is a generalized homogeneous function (Sec. 1.2.1.1). In the Ising model, this would be written as

$$g_s(\lambda^p\theta, \lambda^q B) = \lambda g_s(\theta, B), \tag{1.9}$$

where $\theta = (T - T_C)/T_C$ and B is the external field. By choosing suitable values of λ and manipulating g_s, he was able to show that all critical exponents can be written in terms of p and q. To give a single example, we may obtain the exponent that governs the scaling of the system's magnetization M near the critical point, defined as

$$M(\theta, B = 0) \sim (-\theta)^\beta. \tag{1.10}$$

We can obtain M by differentiating g with respect to B, which in this case reads as

$$\lambda^q M(\lambda^p \theta, \lambda^q B) = \lambda M(\theta, B), \tag{1.11}$$

and set $\lambda = (-\theta)^{1/-p}$ with $B = 0$ to write

$$M(\theta, 0) = \theta^{(1-q)/p} M(-1, 0), \tag{1.12}$$

from where we conclude that $\beta = \frac{1-q}{p}$. Analogous procedures lead to the rest of the exponents and the relations between them (REICHL, 1998).

Meanwhile, at the University of Illinois, Leo Kadanoff introduced the concept of "blocking" in lattice models (TONG, 2017). This method utilized a real-space renormalization group technique, which worked with increasingly coarse lattice models to understand the behavior of systems near critical points. Still in the Ising model example, we start with halmiltonian

$$\mathcal{H} = -K \sum_{\langle i,j \rangle} S_i S_j - B \sum_{j}^{N} S_j. \tag{1.13}$$

To employ Kadanoff's coarse-graining idea we fraction the spin lattice into n blocks of side La, where a is the spacing between points and $L \gg 1$ is an arbitrary number, resulting in $n = N/L^d$ blocks of L^d spins for a d-dimensional system (Fig. 16). Then, we assign to each spin block σ_i a magnetic moment $\tilde{S}_{\sigma_i}$ based on the block's constituents (e.g. a majority rule), under the assumption that block moments $\tilde{S}_{\sigma_i}$ behave like site moments S_j — that is, the new hamiltonian $\mathcal{H}_\sigma$ has the same form as the original lattice's $\mathcal{H}$ — with different parameters $\tilde{K}$ and $\tilde{B}$.

If it is indeed the case that both hamiltonians have the same structure, we can also assume that the form of the partition functions are also the same. Thus, we can relate the thermodynamic potentials of the two models, and infer that

$$g(\tilde{\theta}, \tilde{B}) = L^d g(\theta, B). \tag{1.14}$$

Here, we can make the connection with Widom's scaling hypothesis, relating $\tilde{\theta}, \tilde{B}$ to θ, B by

$$\begin{aligned} \tilde{\theta} &= L^x \theta \\ \tilde{B} &= L^y B \end{aligned} \tag{1.15}$$

to write

Figure 16 – Illustration of the "spin blocking" process.

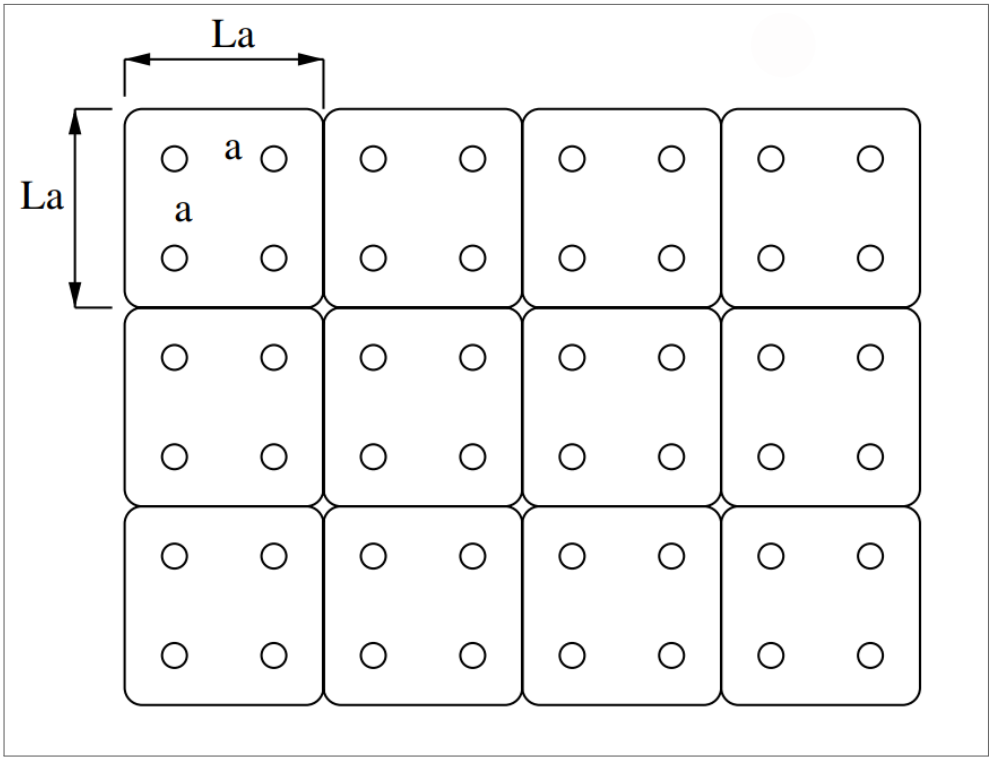

Source: Adapted from (MCCOMB, 2003)

$$g(L^{x/d}\theta, L^{y/d}B) = Lg(\theta, B). \tag{1.16}$$

In this case, $p = x/d$, $q = y/d$ and L functions as the arbitrary λ if $1 \ll L \ll \xi/a$.

Moreover, this approach introduced two new scaling exponents ν and η, respectively from the correlation length close to the critical point

$$\xi \sim (T - T_c)^{-\nu} \tag{1.17}$$

and the correlation function

$$C(r, 0) = \left(\frac{1}{r}\right)^{(d-2+\eta)}, \tag{1.18}$$

which could also be derived in terms of the original ones and vice-versa.

The culmination of renormalization group methods came with the work of Kenneth Wilson, which provided a broader perspective on the renormalization group while connecting ideas from particle physics, statistical physics and condensed matter physics (TONG, 2017). Importantly, he made Kadanoff's picture of scaling mathematically solid, allowing the calculation of critical exponents from microscopic behavior. To understand Wilson's derivation of critical exponents,

suppose a general system of the form

$$\mathcal{H}(\mathbf{K}, \{S_i\}, N) = K_0 + K_1 \sum_i S_i + K_2 \sum_{\langle i,j \rangle}^{(1)} S_i S_j + K_3 \sum_{\langle i,j \rangle}^{(2)} S_i S_j + K_4 \sum_{(i,j,k)} S_i S_j S_k + \cdots . \quad (1.19)$$

Here, $\mathbf{K}$ represents an infinite-dimensional vector that includes all possible coupling constants, while the sum $\sum^{(i)}$ means that only i-th nearest neighbors are included. The dependence on temperature is embedded in the coupling constants K_i. For instance, the Ising model has $K_1 = -\beta B, K_2 = -\beta J$ and $K_3 = K_4 = \cdots = 0$.

Again, we introduce spin blocks σ_i in a way that the blocked partition function has the same functional form as the original one (REICHL, 1998)

$$Z(\mathbf{K}, N) = \sum_{\{S_i, \sigma_I\}} \exp[-\mathcal{H}(\mathbf{K}, \{S_I, \sigma_I\}, N)] = Z(\mathbf{K}_L, NL^{-d}). \quad (1.20)$$

This time, we will think of the change in the free energy in terms of the old and new coupling constants $\mathbf{K}$ and $\mathbf{K}_L$, *i.e.* $g(\mathbf{K}) = L^{-d} g(\mathbf{K}_L)$. This allows us to write the site spin and block spin lattices as connected by a transformation

$$\mathbf{K}_L = \mathbf{T}(\mathbf{K}), \quad (1.21)$$

which can be iterated as much as we want ($\mathbf{K}_{nL} = \mathbf{T}(\mathbf{K}_{(n-1)L})$), as the system's Hamiltonian does not change under $\mathbf{T}$.

In this approach, the critical point $\mathbf{K}^*$ lies where

$$\mathbf{K}^* = \mathbf{T}(\mathbf{K}^*), \quad (1.22)$$

which can be studied from the perspective of non-linear dynamics of discrete maps. In particular, we may linearize the map in the neighborhood of $\mathbf{K}^*$ by choosing small $\delta\mathbf{K}_L = (\mathbf{K}_L - \mathbf{K}^*)$ and $\delta\mathbf{K} = (\mathbf{K} - \mathbf{K}^*)$ to obtain

$$\delta\mathbf{K}_L = \mathbf{A} \cdot \delta\mathbf{K}, \quad (1.23)$$

where $\mathbf{A}$ is the Jacobian matrix $A_{ij} = \partial K_{iL} / \partial K_j$ evaluated at $\mathbf{K}^*$. By calculating the eigenvalues and eigenvectors of $\mathbf{A}$, we may determine the behavior of the trajectories (in the $\mathbf{K}$ "space of possible models"). In this context, universality arises quite naturally: *any* model configuration lying near an eigencurve with eigenvalue $\lambda < 1$ will get arbitrarily close to the fixed point after enough RG transformations. Furthermore, eigenvalues $\lambda > 1$ will have directions along which trajectories diverge from the critical point. These eigenvectors (called *relevant* operators) may be identified as the physical quantities that measure the system's distance to

Figure 17 – Illustration of a hyperbolic fixed point in a two-dimensional space. Relevant deformations, given by eigenvectors whose eigenvalues exceed one (such as u_1 in the picture), repel trajectories from the critical point, and may be identified as physical quantities of the system (like θ or B in the Ising model). Irrelevant ones, like u_2, eventually reach the critical point under successive RG transformations (REICHL, 1998).

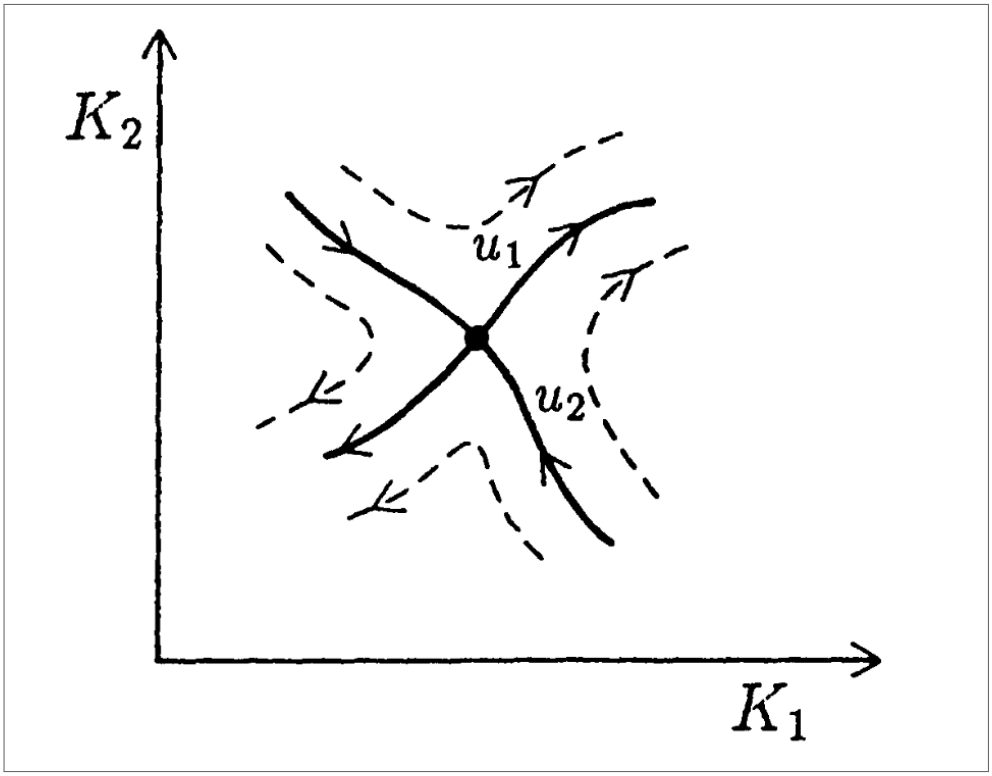

Source: (REICHL, 1998)

the critical point (such as θ or B in the Ising model); its corresponding eigenvalues can be used to write the free energy in a similar way to Widom scaling:

$$g(\lambda_1 \delta u_1, \lambda_2 \delta u_2, ...) = L^d g(\delta u_1, \delta u_2, ...), \tag{1.24}$$

from where values for the critical exponents may be derived like in the example that follows Eq. 1.9.

The obtention of critical exponents can also be done in a momentum-space picture of the renormalization group, where the flow across spatial scales occurs by integrating out high-momentum (small wavelength) modes in Fourier space, in the same recursive fashion as its real space counterpart (WILSON, 1975). For his groundbreaking work, Wilson was awarded the Nobel Prize in Physics in 1982.

There is yet another lens through which we may see RG ideas, which is by working directly from probability theory (JONA-LASINIO, 1975). Here, we are interested in studying how random variables $\xi_1, \xi_2, \ldots, \xi_n$ and their probability distributions $P_1, P_2, \ldots, P_n$ change when summed

together. Our former procedure of blocking variables can then be visualized as constructing convolutions between distributions

$$\hat{P}_n = P_1 * P_2 * \dots P_{n-1} \tag{1.25}$$

with recurrence relations like

$$\hat{P}_{n+1} = \hat{P}_n * P_n \tag{1.26}$$

to understand how they may approach fixed forms (JONA-LASINIO, 2001). Despite this alternative being less widespread in the statistical physics community (perhaps for being more technically complicated), it provides several interesting results, including showing the equivalence between Gell-man and Low's and Wilson's approaches (CASSANDRO; JONA-LASINIO, 1978) and drawing a close connection between the RG and limit theorems (JONA-LASINIO, 1975). These are also among the ideas upon which Leenoy Meshulam, William Bialek, and their group built to construct their phenomenological version of the RG (MESHULAM et al., 2019), as will be shown next.

1.3.2 Model independent coarse-graining

Based on the RG framework, systems with many degrees-of-freedom can still have simple and universal behavior, despite the intricacy of its microscopic constituents. From the perspective of neuroscience, to show that this heuristic still holds for more complex systems — such as neuronal and brain networks — would be a green light for the development of a theory of neural dynamics. However, how could one surpass the intractability of any model that faintly resemble something biological?

In a seminal paper published by Leenoy Meshulam from William Bialek's research group at Princeton University (MESHULAM et al., 2019), a new prospect on the subject was introduced. Drawing inspiration from Leo Kadanoff's block-spins idea, they proposed a phenomenological coarse-graining procedure meant to handle data time series directly, without the need for an explicit model. In standard uses of real-space RG, coarse-graining over neighboring variables is reasonable because interactions are known to be local, hence each variable will be the most correlated with others spatially close to them. In a neural network, locality cannot be taken for granted[5] and in general interactions are unknown. Thus, one solution is to employ correlation

[5] Neurons are extended objects, and make synaptic connections across distances comparable to the size of the entire network (MESHULAM et al., 2019).

measures as a proxy for neighborhood.

In the authors' experimental setup, they used a group of three mice genetically tailored to express a protein that glows fluorescent in the presence of calcium: this is a widely spread technique in neuroscience research, called optogenetics. Then, neural activity can be indirectly tracked by measuring its associated calcium concentration, whose fluorescence is captured by a scanning two-photon microscope (Fig. 18). In their case, temporal resolution is limited to the imaging frame rate of $\Delta t = 1/30$ s. However, the technique achieves excellent spatial resolutions at the μm scale (MESHULAM et al., 2019). Fluorescence levels from a 433 x 433 μm^2 field of view of the mouse hippocampus in the CA1 region are recorded in 40 minute sessions, while the mouse runs through a virtual track. The amount of neurons registered in each animal is $N = 1487, 1485, 1325$.

For a group of N fluorescence variables $\{\sigma^{(1)}(t)\}$, the coarse-graining procedure is as follows (Fig 18C):

(i) Calculate pairwise correlations (Pearson coefficients) between all neurons;

(ii) One pair at a time, join the most correlated variables until none is left alone;

(iii) Restore the normalization of coarse-grained variables;

(iv) Iterate the process.

In summary, after one iteration one should obtain $N/2$ coarse-grained variables

$$\sigma_i^{(2)}(t) = Z_i^{(2)}(\sigma_i^{(2)} + \sigma_{j*(i)}^{(2)}). \tag{1.27}$$

The normalization factor $Z_i^{(k)}$ is chosen so that the average amplitude of the nonzero part of the signal of a variable is equal to one. This choice deals with the arbitrariness of the relation between the amplitude of the fluorescence signal and electrical activity, without distorting the moments where the signal is truly absent. After k sucessive rounds, coarse-grained variables will be sums of 2^k fluorescence signals. A complete description of the method and its results can be found in the Methods chapter, Section 2.1.1.

By monitoring the changes in the statistics of the system across recursive iterations, Meshulam *et al.* could probe for scale invariance by calculating the probabilities of activity and silence. This way, we can see the distribution of coarse-grained variables as the combination of a delta function at zero and a continuous density for positive values

Figure 18 – (A) Experimental setup from Meshulam *et al.*. During the session, a mouse runs on a styrofoam ball while its CA1 region of the hippocampus is recorded via calcium imaging. The ball's motion drives a virtual track forward, which is displayed on the toroidal screen. (B) Neurons in the hippocampus as recorded by calcium imaging. (C) Correlation-based coarse-graining of fluorescence signals. Each variable can only be paired up once, and the iteration ends when there is none left unpaired.

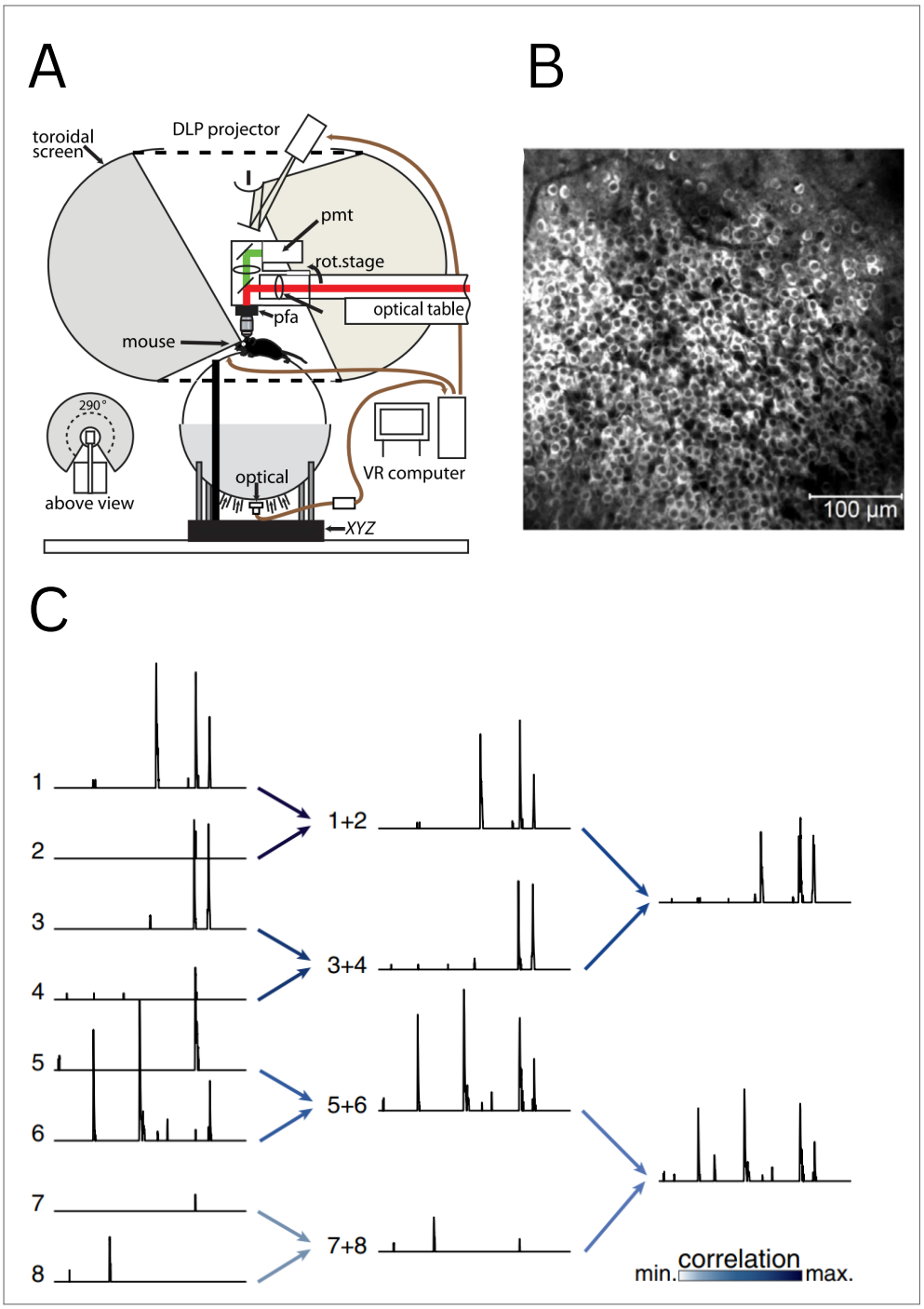

Source: Adapted from (MESHULAM et al., 2019)

$$
\begin{aligned}
P_K(x) &\equiv \frac{1}{N_k}\sum_{i=1}^{N_k}\langle\delta(x-\sigma_i^{(k)})\rangle \\
&= P_0(K)\delta(x) + [1-P_0(K)]Q(x).
\end{aligned}
\tag{1.28}
$$

Figure 19 – Scaling in the activity of coarse-grained variables. (A) Probability of silence within a cluster in function of its size (here denoted as K. dashed line for exponential decay $\widetilde{\beta} = 1$ indicates the expected result for uncorrelated units. (B) Distribution of the normalized activity of coarse-grained variables for increasing K. Notice the different curves approach a fixed form that is non-gaussian.

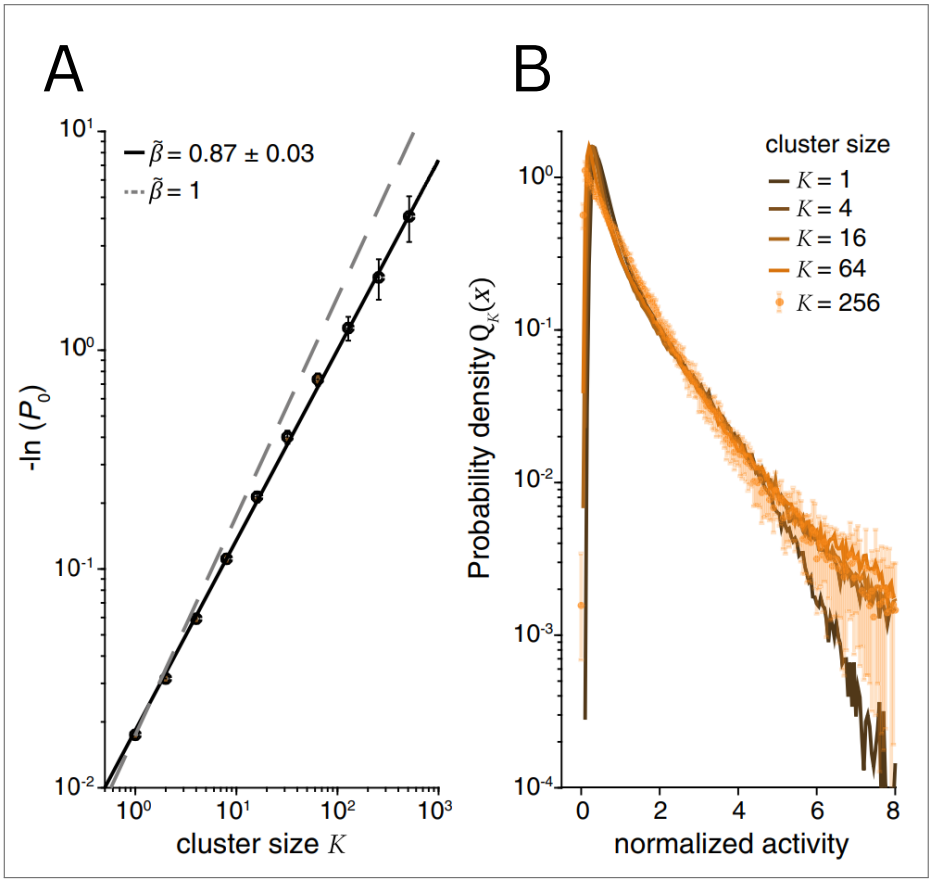

Source: Adapted from (MESHULAM et al., 2019)

If correlations in the data were not self-similar, the sucessive averaging of many microscopic variables would eventually push the probability distribution into a gaussian-form (JONA-LASINIO, 1975). The fundamental concept of the RG here is the possibility of a non-gaussian fixed form (that is, a RG fixed point in the space of models). We can see in Fig. 19B that this is indeed the case, even when variables represent the summed activity of 256 neurons (∼20% of all signals). Additionally, authors also introduced a set of four scaling exponents that could be derived from different quantities of the coarse-grained variables (see Section 2.1.1), such as the log probability of finding silence within a variable, *i.e.* $P(\sigma_i^{(k)}(t) = 0)$ in Fig. 19A.

A fixed non-gaussian form is a signature that the system finds itself in a critical point of its parameter space. Being able to verify this phenomenon in any high-dimensional data without relying on analogies from equilibrium statistical dynamics places this model-independent coarse-graining method as a primary test for criticality in neural data (MESHULAM et al., 2018).

Shortly after the introduction of the phenomenological renormalization group (PRG) tech-

nique, a handful of studies followed. Nicoletti *et al.* (NICOLETTI; SUWEIS; MARITAN, 2020) — who coined the term PRG — verified the validity of the technique on two canonical models with identified phase transitions, the contact process and the Ising model. Notice that the renormalization constant in equation 1.27 deals with aspects specifically related to calcium imaging data; there is currently no general prescription for a renormalization step in the method. For this reason, this and posterior works from other researchers opted to directly sum binary variables, with no normalizing constant[6].

In 2023, the method was extensively repeated in 16 different brain areas of the non-anesthetized mice brain, placing scale invariance as a quasi-universal phenomenon in neural activity (MORALES; SANTO; MUÑOZ, 2023). In this work, an explicit association was made between scale-invariant properties and edge-of-instability phase transition in the lines of what we introduced in Section 1.2.3 (DAHMEN et al., 2019).

Later in the same year, Ponce-Alvarez *et al.* (PONCE-ALVAREZ; KRINGELBACH; DECO, 2023) extended the application of PRG to functional magnetic resonance imaging (fMRI) data. Analyzing a large dataset of human brain data (detailed in Section 2.2.2), their results suggested that there is an intrinsic variability in scaling exponents from one person to another. Chapter 4 will go into this particular application.

This is the scenario in which the work of this thesis was conceptualized and worked through. Before we cover the main results, we dedicate a chapter to detail all the quantitative methods that will be employed throughout the rest of the text.

[6] As was also done in the preprint of Meshulam's original paper (MESHULAM et al., 2018)

2 METHODS

In this chapter, we detail the methods involved in the data processing and analysis throughout this work. Special emphasis is placed on the application of the phenomenological renormalization group (PRG) methodology and its procedural details for our specific datasets, which allow us to achieve the results that will be shown in the final chapters.

2.1 PHENOMENOLOGICAL RENORMALIZATION GROUP

2.1.1 Correlation-based coarse-graining

In the context of the usual real space renormalization group, Kadanoff's original idea of grouping neighbouring spins into blocks makes sense because the interactions are known and local. That is, real-space renormalization was architectured for extensively large, lattice-structured models. Since the interactions are typically unknown for neuronal and brain data, the key idea of the PRG method is to make use of a functional similarity metric as a proxy for distance. Thus, it allows us to (phenomenologically) make use of coarse-graining directly to any set of time series, even without knowledge of an explicit model.

As mentioned, the procedure consists of summing the most similar pairs of variables until none remains ungrouped, then iterating recursively. Initially, Pearson's correlation coefficient will be used to pair up most correlated variables. If $\sigma_i^{(1)}(t)$ is the binary ($\sigma_i^{(1)} \in \{0,1\}$) time series of the raw variable i ($i = 1, \ldots, N$), then after the first PRG interaction one has $N/2$ coarse-grained variables, or "clusters":

$$\sigma_i^{(2)} = \sigma_i^{(1)} + \sigma_{j_*(i)}^{(1)} \ , \tag{2.1}$$

where $\sigma_{j_*(i)}^{(1)}$ is the variable maximally correlated with $\sigma_i^{(1)}$. After k such iterations, we have $N_C = N/2^k$ units (clusters) $\{\sigma_j^{(k+1)}\}_{j=1,\ldots,N_C}$, each of size $C_{size} = 2^k$ (Fig. 20)[1].

[1] In the previous chapter, the cluster size was notated by capital K, as in the original references. We avoid this notation here to better distinguish it from the iteration round k.

Figure 20 – Visual scheme for the PRG procedure. Repeated iterations sum up maximally correlated variables, resulting in clusters of size $C_{Size} = 2^k$ after k iterations. (B) Example of correlation matrices for $C_{Size} = 4, ..., 64$

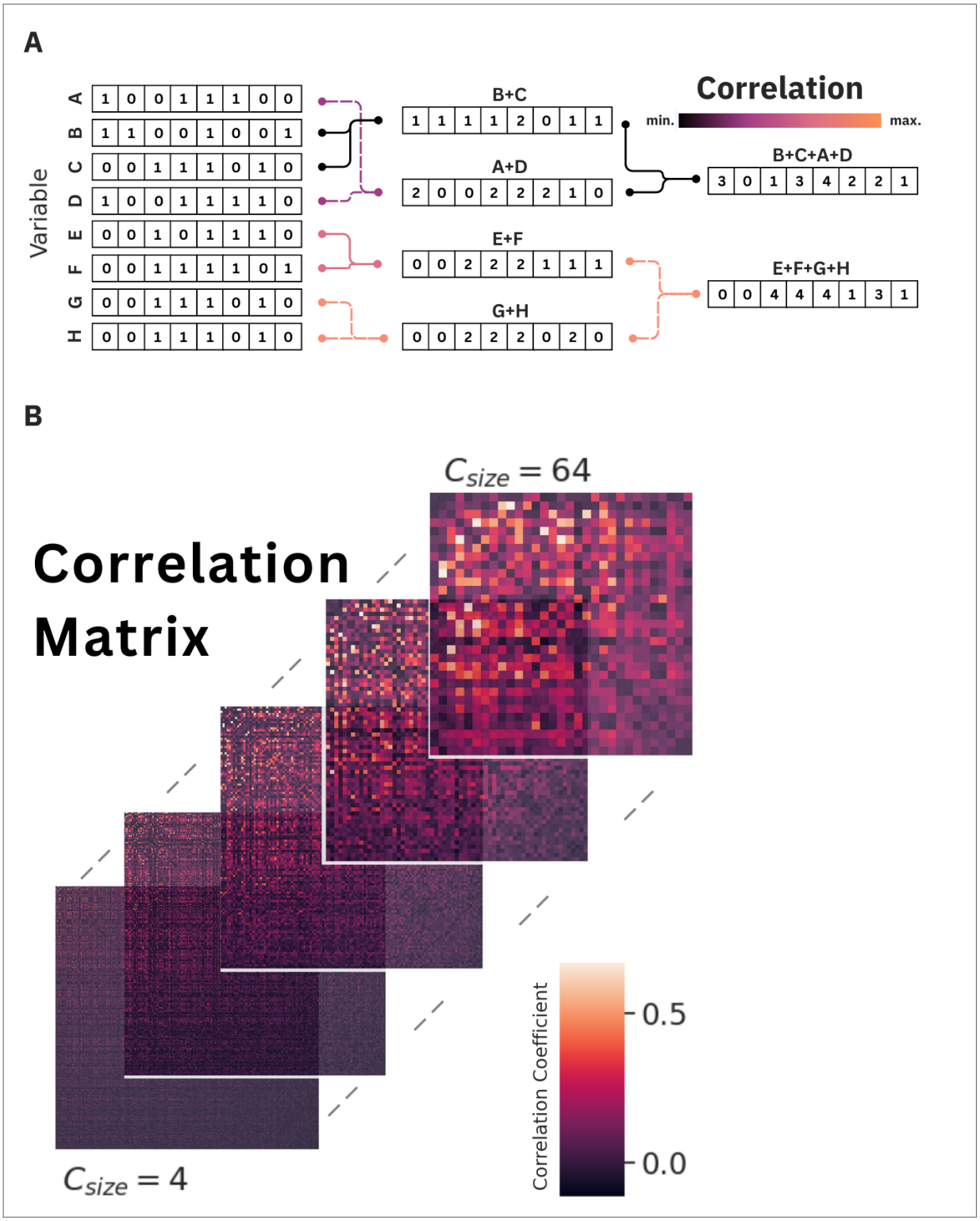

Source: The author.

Under this scheme, the presence of a nontrivial fixed point in the renormalization group should be assessed by scaling relations on several statistical quantities. Notice that, by going "model-free", we lose the connection to the usual scaling exponents obtained in equilibrium statistical mechanics. Hence, we must think of the RG flowing through possible joint probability distributions, rather than hamiltonians (JONA-LASINIO, 2001). The activity distribution under a nontrivial fixed point should approach a non-gaussian form. We have also to rediscover which observables exhibit scaling relations and document their exponents. Meshulam et al. introduced four such quantities – the mean variance, silence probability, covariance matrix spectrum and mean autocorrelation characteristic time – in their pioneering work (MESHULAM et al., 2019). We define them below.

2.1.1.1 Mean variance

The mean variance of the activity of clusters of size C_{size} is written as

$$M_2(C_{size}) = \frac{1}{N_C}\sum_{i=1}^{N_C}\left[\left\langle(\sigma_i^{(k+1)})^2\right\rangle - \left\langle\sigma_i^{(k+1)}\right\rangle^2\right]. \tag{2.2}$$

It grows with cluster size as

$$M_2(C_{size}) \propto C_{size}^{\tilde{\alpha}}\ . \tag{2.3}$$

It can be easily shown that one expects $\tilde{\alpha} = 1$ for independent variables and $\tilde{\alpha} = 2$ for completely correlated ones. Nontrivial self-similar structure should present itself as an intermediate exponent between those two.

2.1.1.2 Probability of silence

When examining the distribution of individual coarse-grained variables, we can track the probability of a cluster remaining inactive at a given moment. For independent variables, such probability decays exponentially, as clusters are simply sums of uncorrelated activity. The presence of self-similarity is again assessed through a power law, namely

$$\mathcal{F}(C_{size}) \equiv -\log \mathcal{P}_{silence}\ \propto C_{size}^{\tilde{\beta}}. \tag{2.4}$$

For independent variables, one expects therefore $\widetilde{\beta} = 1$; for perfectly correlated ones, summing clusters will not change the silence probability, hence $\widetilde{\beta} = 0$. $\mathcal{F}(C_{size})$ can be thought of as

an effective free energy of the system (MESHULAM et al., 2019), although there is no definition for a temperature in this context.

2.1.1.3 Covariance spectrum

We start with the intracluster covariance matrix, defined by

$$C_{ij} \;=\; \langle \sigma_i^{(1)} \sigma_j^{(1)} \rangle - \langle \sigma_i^{(1)} \rangle \langle \sigma_j^{(1)} \rangle \;, \tag{2.5}$$

$\sigma_i^{(1)}, \sigma_j^{(1)}$ being all raw variables comprising a cluster l at the k-th iteration, $\sigma_l^{(k+1)}$. From this matrix, we take its eigenvalues $\{\lambda_r\}_{r=1,\ldots,C_{size}}$, defined by

$$\sum_{r}^{C_{size}} C_{ij} u_{jr} = \lambda_r u_{ir} \;, \tag{2.6}$$

and rank them in descending order. The resulting curve has also been shown to have scaling relations at a RG fixed point (BRADDE; BIALEK, 2017):

$$\lambda_r \propto \left(\frac{C_{size}}{r} \right)^{\mu} \;. \tag{2.7}$$

Scaling is also manifested through the shape collapse of these curves for different C_{size}, providing another hallmark of scale invariance.

2.1.1.4 Characteristic autocorrelation time

From PRG's original prescript, the last scaling relation results from dynamical scaling of the coarse-grained variables. Starting with the autocorrelation function of an individual cluster, namely,

$$C_i(C_{size}, t) = \frac{\left\langle (\sigma_i^{(k+1)}(t_0) \sigma_i^{(k+1)}(t_0 + t) \right\rangle - \left\langle \sigma_i^{(k+1)} \right\rangle^2}{\left\langle (\sigma_i^{(k+1)})^2 \right\rangle - \left\langle \sigma_i^{(k+1)} \right\rangle^2}, \tag{2.8}$$

we take the average across all clusters

$$C(C_{size}, t) = \frac{1}{N_C} \sum_{i}^{N_C} C_i(C_{size}, t) \;. \tag{2.9}$$

From here, we can define the characteristic autocorrelation time as $C_i^{(C_{size})}(\tau_c) = 1/e$. In the presence of dynamical scaling, it should behave as $\tau_c \propto C_{size}^{\widetilde{z}}$. For uncorrelated units, we find trivial exponential decay at all iterations ($\widetilde{z} = 0$).

2.1.2 Momentum-space transformation and non-gaussianity criterion

To analyze the activity distribution of coarse-grained variables, we can also make use of a momentum space (MS) transformation (BRADDE; BIALEK, 2017). This is done by employing a subset of the covariance matrix eigenvectors $\{\mathbf{u}_r\}$, in descending order of their respective eigenvalues, by means of the projectors

$$\hat{P}_{ij}(N_{modes}) = \sum_{r=1}^{N_{modes}} u_{ir}u_{jr} \ , \tag{2.10}$$

where we may choose the cutoff in the number of modes included: $N_{modes} = N, N/2, ..., N/2^k$. With these projectors we can build momentum space coarse-grained variables

$$\phi_i(N_{modes}) = z_i(N_{modes}) \sum_{j}^{N} \hat{P}_{ij}(N_{modes})[\sigma_j^{(1)} - \langle\sigma_j^{(1)}\rangle], \tag{2.11}$$

where $z_i(N_{modes})$ is chosen to make $\langle\phi_i^2(N_{modes})\rangle = 1$ (NICOLETTI; SUWEIS; MARITAN, 2020). In this case, coarse-graining amounts to including an ever smaller fraction of modes into building the new variables, much like in Wilson's MS picture of the RG (Sec. 1.3.1). For systems with translational invariance, the covariance eigenvalue spectrum is equivalent to the Fourier modes of the correlation matrix (as shown in appendix A), which makes the connection to a MS transformation even stronger.

We are interested in the activity distribution of the coarse-grained variables

$$P_{N_{modes}}(\phi) = \frac{1}{N}\sum_{i=1}^{N} \mathbb{P}[\phi_i(N_{modes}) = \phi]. \tag{2.12}$$

In this representation, a trivial distribution (i.e. without strong enough correlations) would fall into a gaussian form for a sufficiently small number of modes, whereas self-similarity presents itself as deviations from a gaussian distribution. To assess the non-gaussianity of the distributions throughout this work, we calculate the kurtosis $\kappa = \langle\phi^4\rangle/\langle\phi^2\rangle^2$. For a gaussian distribution, $\kappa = 3$.

This method establishes a connection between Principal Component Analysis (PCA) and RG (BRADDE; BIALEK, 2017). Both methods seek simplification in the description of systems: PCA does so through dimensionality reduction, which is accomplished by projecting data onto a suitable (highest variance) subspace; the RG also operates by recursively making projections onto lower dimensional spaces, but its simplification happens in the space of models, not the space of system variables (Sec. 1.3.1) (KADANOFF, 2009). Indeed, the complete RG even restores the original number of degrees-of-freedom after each transformation (BRADDE; BIALEK, 2017).

2.1.3 Similarity metrics

To implement the coarse-graining prescription described earlier in section 2.1.1, recent literature involving the PRG methodology relied solely on computing pairwise Pearson correlations in order to aggregate raw variables into coarse-grained ones (MESHULAM et al., 2019; NICOLETTI; SUWEIS; MARITAN, 2020; MORALES; SANTO; MUÑOZ, 2023; PONCE-ALVAREZ; KRINGELBACH; DECO, 2023). However, this is not mandatory. The key to achieving nontrivial fixed points in model space and scaling properties lies in recursively flowing through scales; the specific rule adopted for individual steps should not, at least in principle, matter. Hence, one can test this hypothesis by introducing the coarse-graining step in a slightly more general fashion, namely

$$\sigma_i^{(k+1)} = \sigma_i^{(k)} + \sigma_{j_*(i)}^{(k)}, \quad j_*(i) = \arg\max_j S(\sigma_i^{(k)}, \sigma_j^{(k)}). \tag{2.13}$$

Here, $S(\sigma_i^{(k)}, \sigma_j^{(k)})$ accounts for a chosen similarity metric. We will see in chapter 4 that this is indeed the case. Specifically, we will repeat the analysis with four different metrics: (i) mutual information, (ii) cosine distance, (iii) Hamming distance and (iv) Spearman's rank correlation. Below, we list their definitions.

2.1.3.1 Mutual information

In the context of information theory, mutual information is utilized to quantify how much information you have about a variable, provided the values of another one (LATHAM; ROUDI, 2009). Here, information is defined as the Shannon entropy of a variable, namely

$$H(X) = -\sum_{x\in X} p(x)\log\left(p(x)\right), \tag{2.14}$$

from which we calculate

$$I(X;Y) = -\sum_{x\in X}\sum_{y\in Y} p(x,y)\log\left(\frac{p(x,y)}{p(x)p(y)}\right) = H(X) - H(X|Y), \tag{2.15}$$

where

$$H(Y|X) = -\sum_{x\in X}\sum_{y\in Y} P(x,y)\log\frac{P(x,y)}{P(x)} \tag{2.16}$$

is the conditional entropy.

For independent variables, $p(x,y) = p(x).p(y)$ and hence $I(X;Y) = 0$. Conversely, perfectly correlated variables give $I(X;Y) = H(X) = H(Y)$. In what concerns the usage as a

similarity metric, the main divergence between Pearson's correlation and mutual information is that the latter captures both linear and nonlinear dependences, whereas the former quantifies linear relationships exclusively. Additionally, Mutual information is not normalized by default, albeit it can be by doing $I_{norm}(X;Y) = \frac{I(X;Y)}{\sqrt{H(X)H(Y)}}$, which yields $I_{norm}(X;Y) \in [0,1]$.

2.1.3.2 Cosine Similarity

Commonly applied in machine learning, the cosine similarity reads two time series as two vectors **u**, **v** in high dimensional space and computes the cosine of the angle between them:

$$S_c(\mathbf{u},\mathbf{v}) = \frac{\mathbf{u}\cdot\mathbf{v}}{\|\mathbf{u}\|\cdot\|\mathbf{v}\|}. \tag{2.17}$$

In our datasets negative values do not exist, and hence $0 \leq S_c \leq 1$.

2.1.3.3 Hamming distance

Originally from information and coding theory, the Hamming distance between two vectors computes the number of positions in which the two vectors are different. It is a proper distance measure mathematically speaking, as it satisfies non-negativity, symmetry, the triangle inequality and is zero only if the two variables are identical.

For the PRG application, we will incorporate the Hamming distance in the similarity metric

$$S_{Hamming}(X,Y) = n - d_{Hamming}(X,Y), \tag{2.18}$$

where n stands for the number of entries in X, Y and is the maximum possible value for $d_{Hamming}(X,Y)$. Notice that this measure *completely ignores* the actual values contained in our variables. It should then be a crude, overly simplistic similarity measure.

2.1.3.4 Spearman's rank correlation

Spearman's rank correlation measures the statistical dependence between the rankings of two variables X and Y. Specifically, it is computed by taking the rankings $R(X)$, $R(Y)$ — *i.e.* the relative positions of the list of sorted values of a variable — of the variables and calculating the Pearson coefficient between them. We can write it as

$$\rho_{Spearman} = \rho(R(X),R(Y)) = \frac{\langle R(X)R(Y)\rangle - \langle R(X)\rangle\langle R(Y)\rangle}{\sqrt{\langle R(X^2)\rangle - \langle R(X)\rangle^2}\sqrt{\langle R^2(Y)\rangle - \langle R(Y)\rangle^2}}. \tag{2.19}$$

In the case of binary data, only two ranks are possible and hence the calculation is identical to Pearson correlation. Consequently, applying the PRG method with Spearman or Pearson correlation should yield similar results at first. As coarser-grained variables have more possible values (therefore more possible ranks), the two metrics cease to be equivalent after the first iteration.

2.1.4 PRG Convergence via Wasserstein distance

Another unaddressed aspect of the PRG application concerns the convergence of the iterations. In theory, phase transitions occur in systems with an infinite number of degrees-of-freedom (KADANOFF, 2009). While both real and momentum space renormalization could be iterated indefinitely under these conditions, this is not the case for real-world data, in particular biological systems. Therefore, it is of interest to possess some technique to monitor the changes — and perhaps the convergence — of phenomenological coarse-graining across iterations.

In chapter 4, we propose a candidate to fulfill this role. After each coarse-graining step, compute the Wasserstein distance between activity distributions from the the current and previous iteration. Originally from optimal transport, the conceptual idea of this measurement is to quantify the minimum amount of "mass" moved required to transform one distribution into another (PANARETOS; ZEMEL, 2019) (Fig. 21).

Figure 21 – Example of the optimal transport map that morphs P into Q.

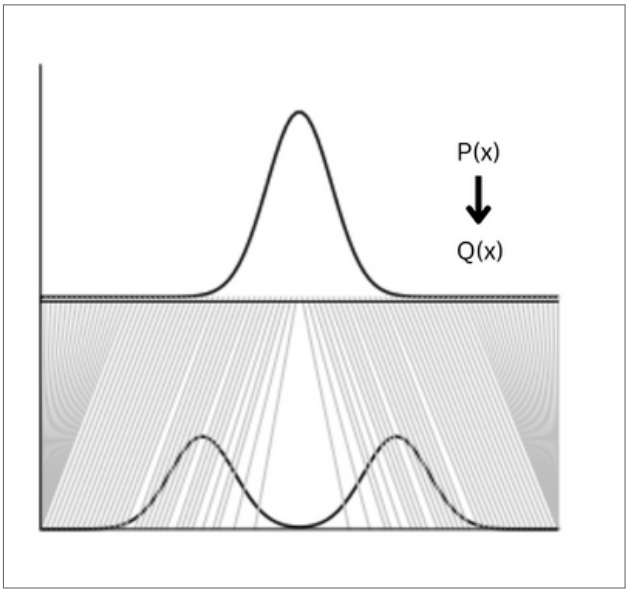

Source: Adapted from (KOLOURI, n.d.).

For $X \sim P$ and $Y \sim Q$ (*i.e.*, X (Y) is a variable whose possible values are determined by the specified probability distribution P (Q)), let $\mathcal{J}(P,Q)$ denote all joint distributions J for (X,Y) that have marginals[2] P and Q. The Wasserstein distance is then defined as

$$W_p(P,Q) = \left(\inf_{J \in \mathcal{J}(P,Q)} \int ||x-y||^p dJ(x,y) \right)^{1/p}, \tag{2.20}$$

with $p \geq 1$. If both distributions are one-dimensional, there is a simpler, closed-form expression in terms of the inverse of the cumulative distributions (or quantile functions) of P and Q, F^{-1} and G^{-1}:

$$W_p(P,Q) = \left(\int |F^{-1}(z) - G^{-1}(z)|^p dz \right)^{1/p}, \tag{2.21}$$

where $F^{-1}(z) = \inf x \in \mathbb{R} : z < F(X)$.

Although less simple than common alternatives, such as Kullback-Leibler divergence or the Kolmogorov-Smirnov test, The Wasserstein distance has two desirable features: first, it is less sensitive to outliers; second, it is suited to compare distributions with different supports (*e.g.* P continuous and Q discrete) (VILLANI, 2021). It is also a proper distance measure, although this is not a requirement for our purposes.

2.2 DATA ACQUISITION AND PREPROCESSING

This section examines the datasets used in this study. It is divided in two main parts: spiking data from the primary visual cortex of urethane-anesthetized rats and continuous data from resting-state functional magnetic resonance imaging (rs-fMRI) in humans. Details of the acquisition and data processing pipelines for each part are discussed in the next sections.

2.2.1 Urethane-anesthetized rat spiking data

2.2.1.1 Acquisition

In the first experimental setup, we have nine extracellular recordings of ongoing activity in the rat's primary visual cortex (V1) under urethane anesthesia. Recordings last 216 ± 31 min. All 9 datasets used the same surgery and recording protocol, as described in (VASCONCELOS et al., 2017; FONTENELE et al., 2019; CARVALHO et al., 2021).

[2] Given a joint probability distribution over multiple variables, the marginal distribution of a specific variable is obtained by summing (or integrating, in the continuous case) over the other variables.

The recordings were conducted on non-albino and albino male rats (Long-Evans, $n = 2$ (CARVALHO et al., 2021); Wistar-Han, $n = 7$ (VASCONCELOS et al., 2017)) aged 3-4 months. They were anesthetized with urethane (1.58 g/kg, 1.44 g/kg, respectively). As soon as the animal reached plane anesthetics, the surgery was performed, including trichotomy, craniotomy, and durotomy (only non-albino). The coordinates used to guarantee V1 recording access (PAXINOS; ASHWELL, 2018) were AP (anteroposterior) $= -7.2$ mm, ML (mesolateral) $= 3.5$ mm (Fig. 22A).

A 64-channel silicon probe (BuzsakiA64sp, Neuronexus) with 6 shanks 200 μm apart was implanted in the primary visual cortex deep layers. In each shank, 10 channels of area 160 μm^2 are disposed from the shank tip in a staggered configuration, 20 μm apart. Four extra channels exist along the 4th shank for tissue depth reference. The raw data were sampled at 30 kHz (16 bits/sample), amplified, and digitized in a single head-stage Intan RHD2164.

Out of the 9 recordings, 7 were performed at the University of Minho/School of Medicine abiding by the European regulations (European Union Directive 2010/63/EU), and all the experiments were approved by the Ethics Committee of the University of Minho (SECVS protocol #107/2015). Two of the recordings were performed at the Systems and Computational Neuroscience lab in the Federal University of Pernambuco in strict accordance with the CONCEA-MCTI directives and were approved by the Federal University of Pernambuco (UFPE) Committee for Ethics in Animal Experimentation (23076.030111/2013-95 and 12/2015).

The extracellular electric potential raw data was pre-analyzed using Klusta-Team Software. Following the spike sorting pipeline, two kinds of activity are obtained: single- and multi-unit activity (SUA and MUA). In SUA, individual spikes were isolated by the spike sorting process and attributed to a specific neuron based on their distinctive waveform and timing characteristics. MUA contains activity from multiple and/or distant neurons that could not be discerned. For all analyses, we employed both single-unit and multi-unit activities.

2.2.1.2 Binarization

Following preprocessing, we partitioned the data containing spike timings for each unit in 50-ms bins, aligning methodology outlined in Refs. (FONTENELE et al., 2019; LOTFI et al., 2020; LOTFI et al., 2021). A unit i was considered active ($\sigma_i(t) = 1$) if there was at least one spike within a bin centered at time t, and inactive ($\sigma_i(t) = 0$) otherwise (Fig. 22B). The population firing rate $\rho(t)$ at each bin was estimated as the total number of spikes divided

by the bin duration. Due to the nature of the method, only experiments with $N \geq 256$ units were selected for this analysis.

Figure 22 – Data acquisition from the anesthetized rat's primary visual cortex. (A) Recording location (left), shank positions within the silicon probe (top right) and samples of spike waveforms (bottom right). (B) Example of a raster plot after preprocessing: each line represents a neuron, with binned spike timings marked as dots along the horizontal axis.

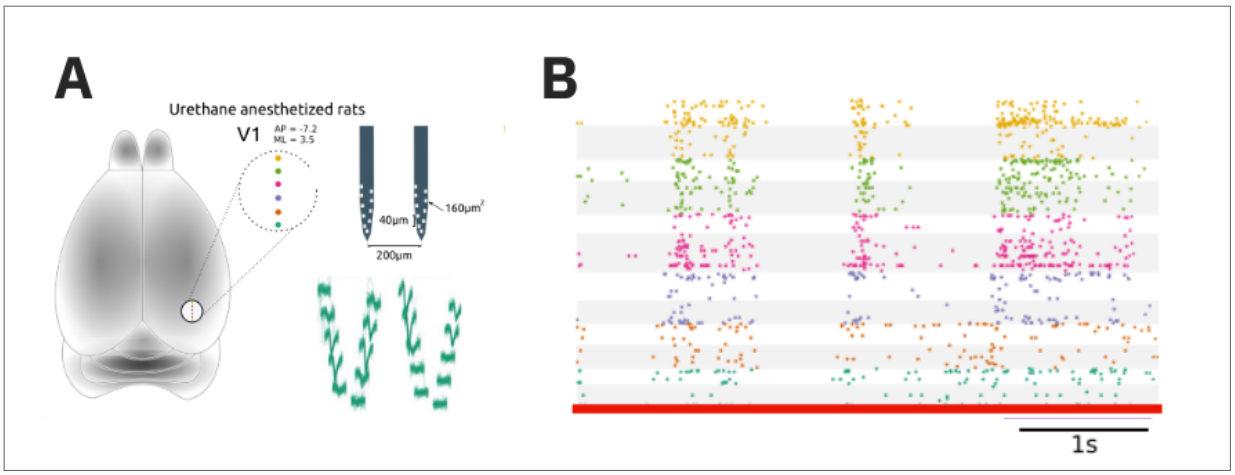

Source: Adapted from (FONTENELE et al., 2019).

2.2.1.3 Surrogate data

In neuroscience, a standard practice employed to validate results is to subject the analysis to testing on surrogate data. This approach involves generating surrogate datasets that preserve certain statistical properties of the original data, while disrupting other features. By applying the same analytical methods to both the authentic and surrogate datasets, it is possible to discern whether observed effects are genuine or can also arise from random fluctuations.

In this study, all surrogates for spiking data were generated by shuffling the interspike intervals (ISI) of original units within each analyzed time window (CASTRO et al., 2024). This results in each spike train possessing the same ISI distribution of the original one, but destroys the temporal ordering of the spikes.

2.2.2 Human fMRI data: The Human Connectome Project

2.2.2.1 Acquisition

The second collection of datasets derives from human fMRI data obtained through the Human Connectome Project. The project is a large-scale research endeavor, created to provide an extensive number of human brain data and analysis tools to be shared openly with the scientific community (ELAM et al., 2021). In total, 1439 subjects were analyzed, 714 from the Young Adults dataset (aged 22-35) and 725 from the Aging dataset (aged 36-100+). Both contain extensive demographic, behavioral and clinical data from subjects, allowing us to compare these attributes to fMRI data analysis.

In fMRI data, time series are generated from blood oxygenation level dependent (BOLD) signals (HILLMAN, 2014). In summary, BOLD signals reflect changes in blood oxygen – typically small changes, around 1-5% –, measurable due to the different magnetic properties of oxygenated and non-oxygenated hemoglobin. These fluctuations are associated to neural activity levels (after undergoing several preprocessing steps related to the remotion of physiological noise, such as heartbeats and head motion). The resulting signal has high three dimensional spatial resolution (in the order of 1 mm) of the entire brain, at the expense of temporal resolution, with sampling rates in the order 1 s (Fig. 2).

2.2.2.2 Binarization

Differently from spiking data, fMRI data has continuous values. In order to obtain the binary format required to follow the coarse-graining prescript, we first need a criterion to map the BOLD signal into a binary time series.

Firstly, to analyze fMRI data, researchers often divide the brain into distinct regions based on anatomical or functional criteria. These regions are often referred to as parcels or regions of interest (ROIs), which can be defined in a standardized way across different individuals or studies through an fMRI parcel atlas. In this study, we chose the 1000 parcels Schaefer Atlas in all analyses, as it is the standard atlas with the highest number of parcels (1014) (SCHAEFER et al., 2018).

To obtain binary variables, we employed an upper threshold in the z-score of the continuous signal. Specifically, a unit (parcel) was considered active ($\sigma_i(t) = 1$) if there was at least one

value of the BOLD signal surpassing the z-score upper threshold $z_{threshold}$ within a bin centered at time t; otherwise, it was considered inactive ($\sigma_i(t) = 0$). This methodology was also applied in Ponce et al.(PONCE-ALVAREZ; KRINGELBACH; DECO, 2023). Given the inherently low time resolution of the signal, bin sizes for fMRI data in this study were all equal to the inverse of the sampling rate (meaning there is a single data point per bin). A visual summary of process can be seen in Fig. 23.

Figure 23 – Pipeline for fMRI binarization. (A) Map BOLD signals into a parcel atlas; (B) Employ a z-score upper threshold; (C) Assign 1 or 0 for each bin centered at time t.

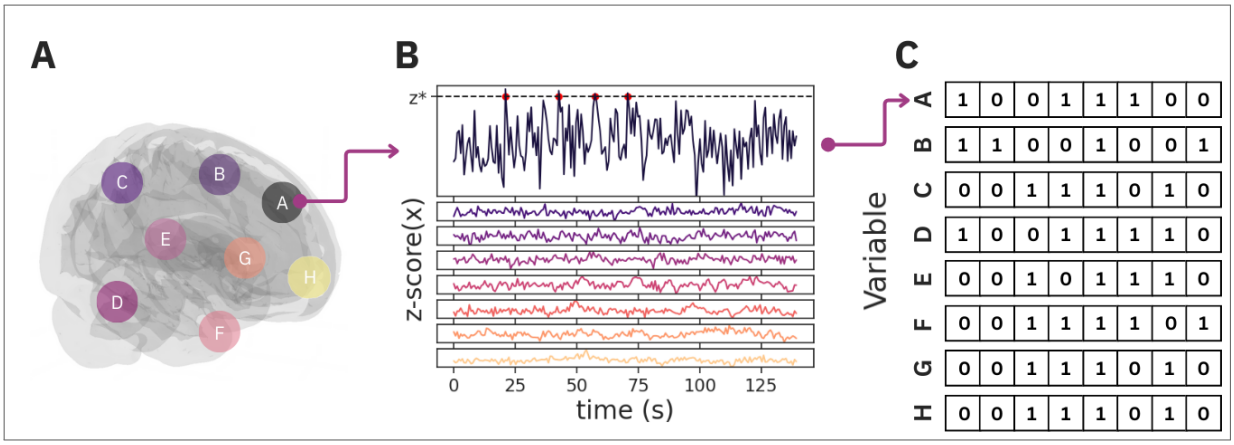

Source: The author.

2.2.2.3 Surrogate data

As explained in section 2.2.1, we test the robustness of our analyses by repeating them on surrogate data. For all fMRI data, we obtain surrogates by taking the Fourier transform of the original data, shuffling its complex phases and taking the inverse transform, as previously done in the literature(SCHREIBER; SCHMITZ, 2000). The process is done within each analyzed time window and, differently from spiking data, occurs before binarization.

3 STATE DEPENDENT SCALING: IN AND OUT OF CRITICALITY?

This chapter contains the first central results of this thesis. Here, we investigate how signatures of scale invariance, as assessed by the PRG methodology, are influenced by different dynamical regimes in the rat's primary visual cortex. We do so by taking advantage of an urethane anesthesia experimental protocol, in which the cortical activity from our recordings spontaneously drifts between a spectrum of synchronization levels, here defined by population-level spiking variability.

What we find is that, in order to find scale invariance signatures, we must surpass a characteristic threshold in variability. Low variability instances, which stem from asynchronous activity, do not display statistics indicative of proximity to a critical point. The system fluctuates between the two states, seemingly in and out of criticality, spending approximately three quarters of the experiment duration within the scaling regime.

3.1 COARSE-GRAINING DATA FROM ANESTHETIZED RATS' VISUAL CORTEX

As described in section 1.2.2.2, Fontenele *et al.* recently proposed a relationship between criticality and cortical states in a study including spiking data of urethane-anesthetized rats (FONTENELE et al., 2019). The urethane anesthesia setup allows cortical activity to drift spontaneously for extended recording periods. Consequently, it is possible to observe more synchronized states, akin to those found during drowsiness and slow-wave sleep, and more desynchronized states, like what we see during awake and alert behavior (HARRIS; THIELE, 2011; CLEMENT et al., 2008). In order to quantify this variability, authors chose to calculate the coefficient of variation (CV) of the population spiking rate. Evaluated every few seconds, CV measurements were employed as a *de facto* control parameter for cortical states (with CV increasing with synchronization levels). By subjecting avalanche exponent analysis to segmentation by CV, scaling relations were present only within a *narrow* range of spiking variability. This suggested that, while the brain's dynamics exhibited considerable fluctuations, only intermediate CV values met stricter criteria for criticality, as assessed by scaling relations for avalanche exponents.

Later, an alternative interpretation was presented by Carvalho *et al.* (CARVALHO et al., 2021) (also detailed in section 1.2.2.2). Using an analytically solvable model, the majority

of experimental results were successfully reproduced. By adjusting the relative weight of the model's inhibitory coupling — a true control parameter (GIRARDI-SCHAPPO et al., 2020) — the model could reproduce almost the whole range of spiking variability observed in the data within only 3% of its critical point. This raised the possibility that the urethanized rat cortex was actually close to a critical point most of the time, instead of only *en passant*. If true, these results suggest that a wide range of the observed spiking variability would correspond to small fluctuations around the critical point, an important conclusion for the understanding of cortical states. Additionally, since CV fluctuated widely even for fixed values of a *bona fide* control parameter in the model, it would not be suited as an "effective" control parameter. However, these conclusions were solely based on results derived from the model. To further investigate this matter, we employed the PRG method in conjunction with a state-dependent analysis, where we segmented the data by CV, following the approach outlined in (FONTENELE et al., 2019).

Figure 24 – Scaling relations obtained from the coarse-graining procedure for a single animal. (A) Mean Variance, (B) Silence Probability and (C) Characteristic autocorrelation decay time as functions of cluster size. (D) Intracluster spectrum of the covariance matrix. (E) and (F) show the probability density $P_K(\phi)$ of MS coarse-grained variables in the original and surrogate data, respectively. In (A)-(D), r^2 stands for the usual coefficient of determination, used to assess the quality of our power-law fits. Points (shades) are averages (standard deviations) across all the 600 s windows.

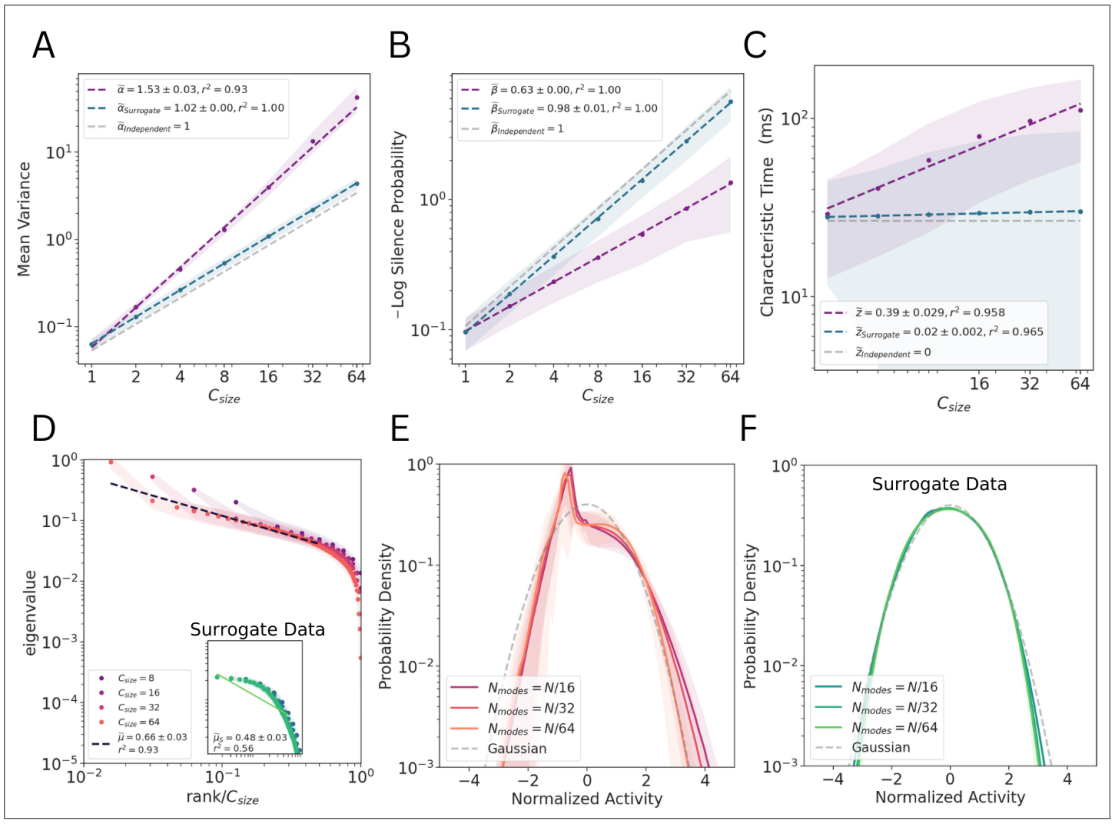

Source: (CASTRO et al., 2024)

At first, we applied the PRG procedure (Sec. 2.1) to raw spiking data and averaged from 600-s time windows of the whole time series. By doing this, we are purposely disregarding the fact that spiking variability changes considerably in the scale of a full experiment. We obtained results regardless of CV values, and verified their robustness by repeating the same procedure on surrogate data, which was obtained by shuffling the interspike intervals (ISI) of each unit during the time window of the analysis (Sec. 2.2.1.3).

We observe that, across all animals, the average variance of cluster activity rose with cluster size according to a power law, characterized by a non-trivial exponent $1 < \widetilde{\alpha} < 2$ (as explained in Eq. 2.3 and illustrated in Fig. 24A). In surrogate data, the scaling aligns more closely with expectations for independent data.

As we increasingly simplify and aggregate our variables into sums involving more units, the likelihood of a variable being entirely silent diminishes, particularly for large C_{size}. For the free energy, we observe a power-law decline with $\widetilde{\beta} < 1$, consistent with the anticipated self-similar correlations (Eq.2.4 and Fig. 24B). Surrogate data, on the other hand, shows a faster decay, which corresponds to the trivial case $\widetilde{\beta} = 1$.

Dynamical scaling is also evident in the coarse-grained variables. The autocorrelation decays with a characteristic time τ_c, and we observe that larger clusters of units also have an increased relaxation time (Fig. 25). It increases as $\tau_c \propto C_{size}^{\widetilde{z}}$ (as shown in Fig. 24C and detailed in Sec. 2.1.1.4). For surrogate data, this correlation time remains unaffected by cluster size.

Figure 25 – Example of the scaling of the mean autocorrelation function for a single animal. We can observe the function's relaxation time increase progressively as we coarse-grain our variables into bigger clusters.

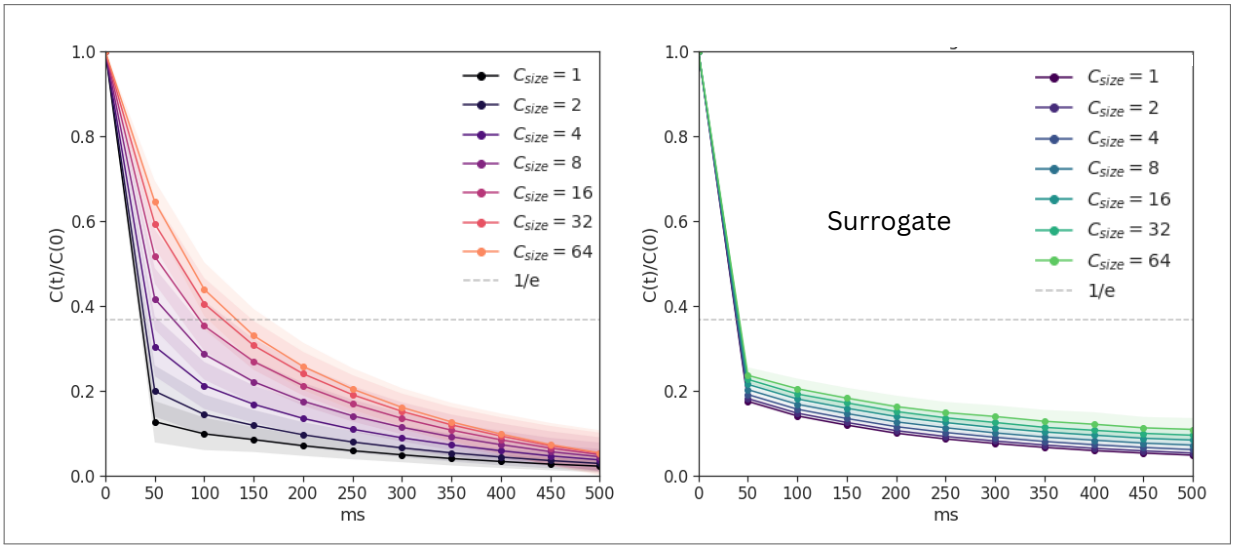

Source: The author.

The fourth and final power-law relationship is found in the eigenvalue spectrum of the covariance matrix. We observe that the eigenvalues diminish in relation to their rank, characterized by an exponent $\widetilde{\mu}$ (Eq. 2.7). For surrogate data, the shape of the spectrum is not well fit by a power-law function. Additionally, and consistently with previous findings (MESHULAM et al., 2019; MORALES; SANTO; MUÑOZ, 2023) and Eq. 2.7, the spectrum curve converges to a single shape as we compute the covariance matrix within clusters of increasing size (Fig. 24D).

We also obtained the probability distribution of the activity of coarse-grained variables at successive iterations. This is done in two manners: by looking directly at the coarse-grained variables (Fig. 26), and by calculating momentum-space coarse-grained variables, obtained by making a projection using a progressively reduced number of modes in momentum space (Eq. 2.11). Both approaches yield non-gaussian distributions, indicative of self-similar correlation structure. The coarse-grained variables activity distribution in momentum space (Fig. 24E) will be particularly relevant for state-dependent analysis in the upcoming section. Again, from surrogate data, we obtain trivial gaussian distributions (Fig. 24F), in consonance with the central limit theorem (JONA-LASINIO, 2001).

Averaging these results over the group of 9 animals (henceforth denoted by $\langle \cdots \rangle_g$), we obtained $\langle \widetilde{\alpha} \rangle_g = 1.66 \pm 0.28$, $\langle \widetilde{\beta} \rangle_g = 0.70 \pm 0.08$, $\langle \widetilde{z} \rangle_g = 0.33 \pm 0.07$, and $\langle \widetilde{\mu} \rangle_g = 0.56 \pm 0.10$. To measure the distinction between the activity distributions of authentic and surrogate data, we compared the kurtosis values at the most granular level of (momentum-space) coarse-graining: $\langle \kappa \rangle_g = 43 \pm 23$ and $\langle \kappa \rangle_g^{\text{surrogate}} = 6.4 \pm 1.4$. The large standard deviation observed in the kurtosis of the real data has a clear cause: we are ignoring the extensive range of cortical states induced by urethane (CLEMENT et al., 2008; VASCONCELOS et al., 2017; FONTENELE et al., 2019; CARVALHO et al., 2021). As a result, we lumped together regimes that we will now show to be qualitatively different in terms of scaling.

Figure 26 – (A,B) Activity distribution of coarse-grained variables at the last 3 iterations ($C_{size} = 16, 32, 64$). Here, the x-axis is normalized so activity $= 1$ stands for the maximum value permitted by the variables in their k-th iteration, 2^k. (C,D) Same as the previous, without log-scale and including all iterations.

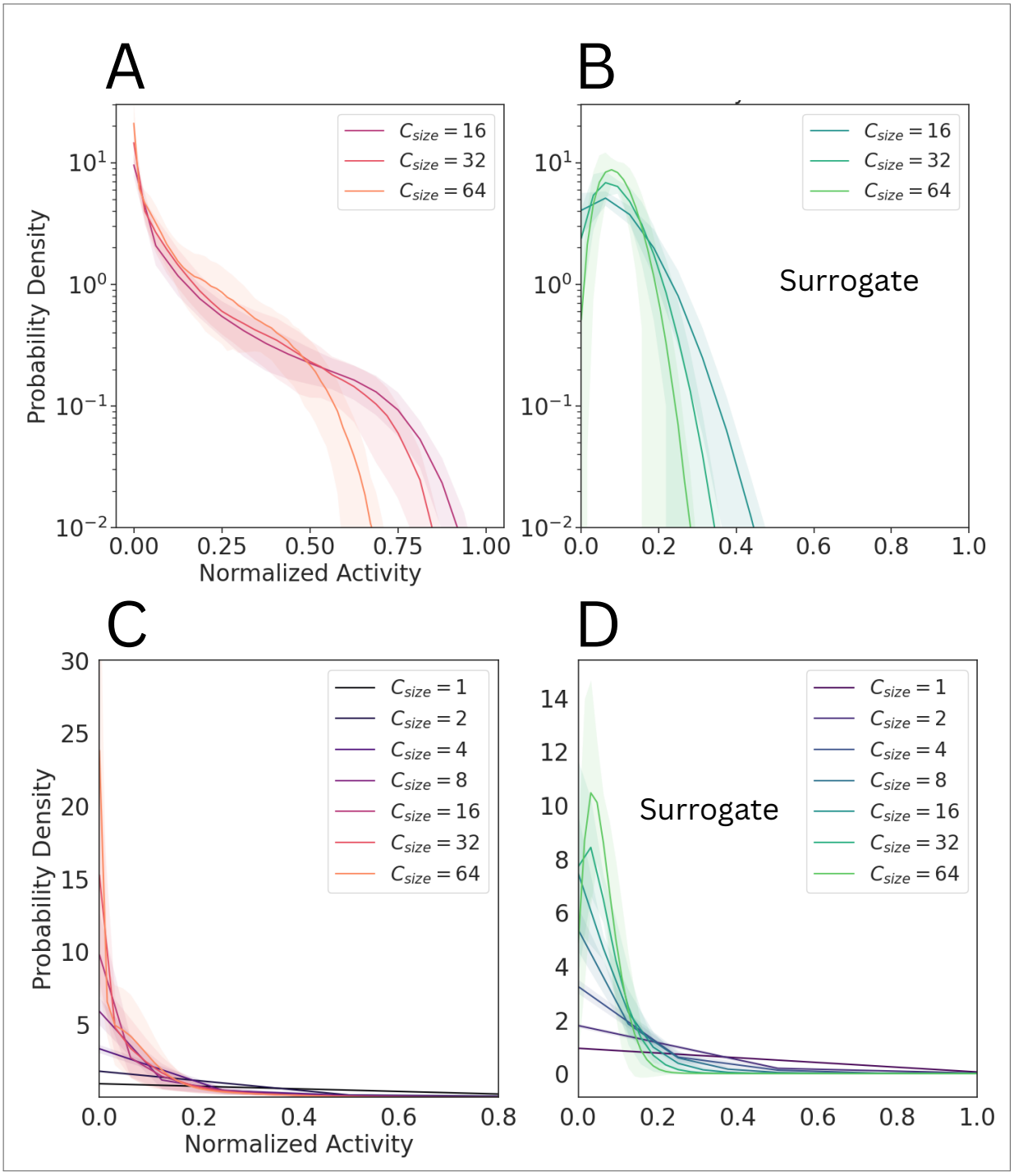

Source: The author.

3.2 STATE DEPENDENT ANALYSIS: CV PARSING

Next, we investigate to which extent the scaling results change as we parse the data according to spiking variability, as inferred by CV. The cortical CV time series of a typical urethane-anesthetized rat is erratic (Fig. 28A). Spike timings in the population of neurons gradually shift from asynchronous to more synchronized for larger CV values. (Fig. 28B). Additionally, high (low) CV levels are associated with high (low) mean values of pairwise spiking correlations between neurons (HARRIS; THIELE, 2011). As the correlation structure is a key ingredient in the PRG coarse-graining process, it is reasonable to anticipate that CV levels would affect the outcomes of the scaling analysis.

And indeed they do. We follow a data segmenting routine similar to previous works (VASCONCELOS et al., 2017; FONTENELE et al., 2019; LOTFI et al., 2020; CARVALHO et al., 2021), and calculate the CV of the population firing rate in windows of 30 s. Then, we execute the PRG analysis within each window. First, we find that all four scaling exponents are impacted by the spiking variability level, as seen in Fig 27. Observe how our results can point to different exponent values if we restrict our view to a specific CV range. The influence of CV in the analysis is also reflected in the distributions. For instances of high-CV data, we obtain activity distributions from MS coarse-graining that converge to a non-trivial (i.e. non-gaussian) shape (Fig. 28C). Conversely, for a sufficiently low value of CV, distributions from MS coarse-grained variables fall into a trivial gaussian form (Fig. 28C). Figures 28E-28H shows the scaling exponents obtained in function of the kurtosis of the distribution stemming from the same time window.

Based on the differences between authentic and surrogate data, we chose a criterion to determine whether scaling is present in a given time window. Specifically, we compare the kurtosis of the MS activity distribution (Eq. 2.12) of the analyzed time-window with the kurtoses of the distributions of MS surrogate data of all windows from the time series. Note that this is a stricter criterion than comparing solely between the same window's corresponding surrogate data. We classify the activity within a time window as displaying scaling if its kurtosis value exceeds one standard deviation above the mean kurtosis of the surrogate data. Although this line is in principle arbitrary, the analysis is not sensitive to the number of standard deviations chosen as threshold value. As we can see below, (Fig. 28D) typical kurtosis values in actual data where scaling is present are, on average, two orders of magnitude greater than the surrogate standard deviation.

Figure 27 – Scaling exponents from data segmented by CV. In this example, individual CV values from each time window were divided in 8 quantiles of equal size between its lowest and highest value. Then, line corresponds to averaging only the 30-s time windows whose CV value fall within the same quantile.

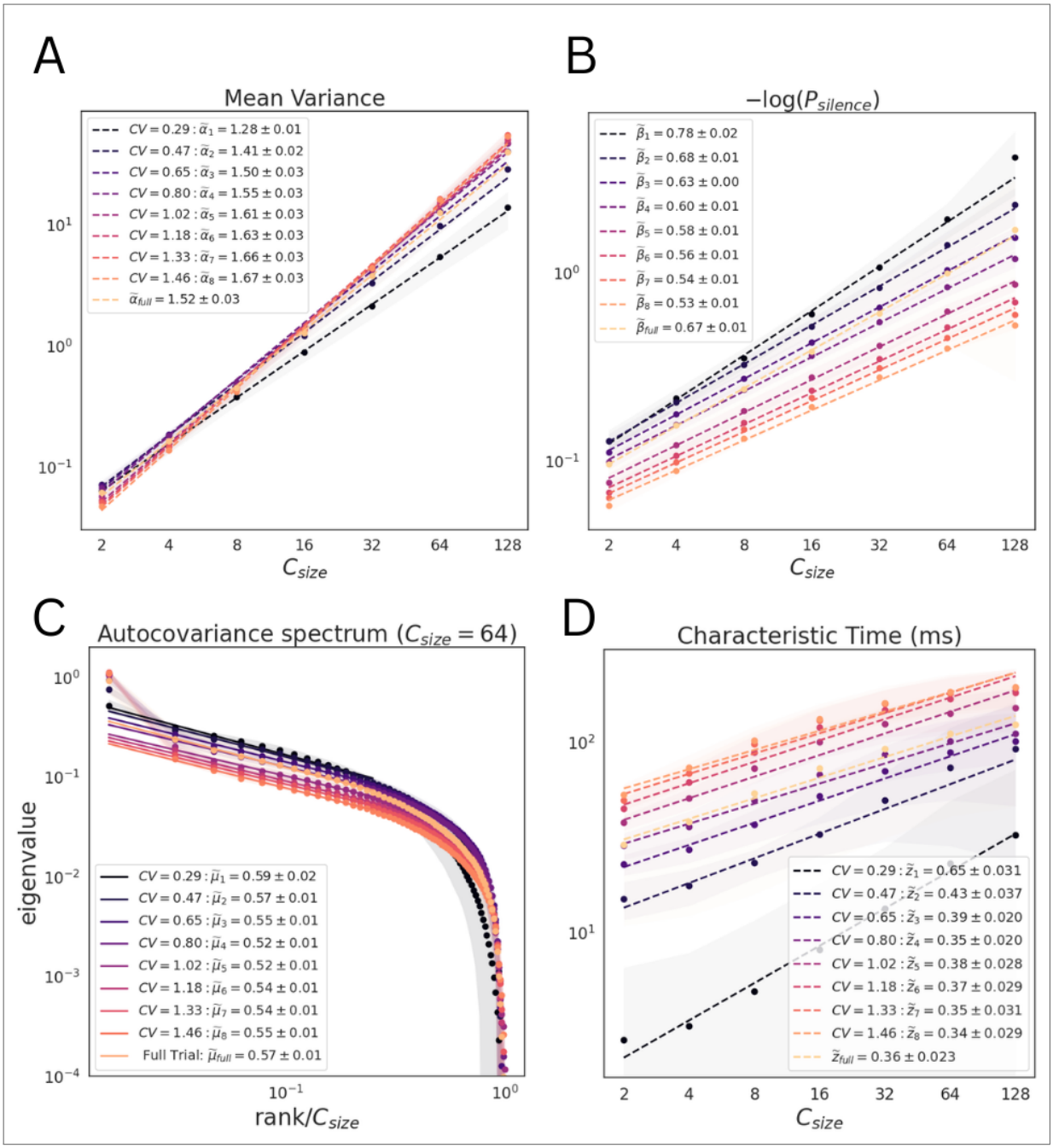

Source: The author.

By this criterion, we can identify a remarkable relationship between spiking variability and the non-gaussianity of distributions. There is a characteristic value of CV ($\simeq 0.7$) above which the kurtosis sets apart from its surrogate counterpart, increasing monotonically (Fig. 28D). Below this CV level, we consistently obtain gaussian distributions like those from surrogate data. In appendix B, we show an image panel for the state-dependent behavior of distributions

and exponents for each of the nine animals analyzed. The MS coarse-graining analysis thus indicates the presence of two distinct qualitative regimes: a trivial one occurring below a characteristic CV value and a non-trivial one emerging above it.

The relationship between the kurtosis κ and CV bears resemblance to a second-order phase transition graph of order parameter versus control parameter. Although tempting at first glance, making such comparison would be misleading. In a phase transition, scaling is expected at the critical value of the control parameter. In contrast, the kurtosis observed in the urethane data means non-trivial scaling at any point above the characteristic threshold. Thus, our findings provide backing to the conjecture put forth by Carvalho et al. (CARVALHO et al., 2021) that CV is not an ideal candidate for a control parameter, especially within the framework of the PRG coarse-graining procedure.

The behavior of the other exponents aligns consistently with this interpretation. When the coefficient of variation (CV) is low ($\lesssim 0.7$) and the kurtosis lowers approaching that of surrogate data, the scaling relationships exhibit poor goodness-of-fit, resulting in exponents spanning a wide range of values (shaded areas in Figs.**??**E-H). However, a sufficient increase in CV ($\gtrsim 0.7$), causes the kurtosis to deviate from surrogate levels and display non-gaussian activity distributions. The exponents $\widetilde{\alpha}$, $\widetilde{\beta}$, $\widetilde{\mu}$, and $\widetilde{z}$ then stabilize with scaling relationships characterized by exceptional goodness-of-fit (Figs.28E-28H). Thus, we further confirm that there are two distinct behaviors when we employ the threshold kurtosis criterion to infer scaling.

It's worth noting that these stable values differ slightly from those obtained through the state-independent analysis (shown in Section 3.1). The latter averages two regimes that, in hindsight, we show to be entirely distinct.

3.3 GROUP RESULTS

We conducted the state-dependent scaling analyses on all nine subjects available in our study. By averaging only over data segments that satisfied the scaling criterion mentioned above, we observe the behavior of exponents across subjects: $\langle\widetilde{\alpha}\rangle_g = 1.7 \pm 0.3$, $\langle\widetilde{\beta}\rangle_g = 0.62 \pm 0.08$, $\langle\widetilde{z}\rangle_g = 0.36 \pm 0.07$, and $\langle\widetilde{\mu}\rangle_g = 0.63 \pm 0.12$ (Fig. 29A-29D).

While the range of kurtosis values is not the same across subjects (Fig.29E), this variability is consistent with their differences in spiking variability distributions (Fig.29F). Despite these disparities, the characteristic CV value at which scaling manifests remained remarkably robust

Figure 28 – Results of state-dependent PRG analysis for the same subject shown in Fig. 24. (A) Example of the coefficient of variation over time for a single experiment. The curve on the right depicts a histogram of CV. (B) Examples of raster plots for different CV values. (C) Activity distribution of variables built from $N/64$ eigenmodes. Each curve averages all trials within a range of CV [in this case separated in 30 quantiles, 3 between each dashed line in (A)]. (D) Kurtosis of the distribution of MS corse-grained variables (built from $N/64$ eigenmodes). Darker curve is the moving average over windows of twelve consecutive points. Grey stripes comprise the range of κ values that fail to meet the scaling criterion (Section 2.1.2), i.e. $0 \leq K \leq \langle K \rangle^{surrogate} + \sigma_K^{surrogate}$. (E,F,G,H) Impacts of state dependence on the scaling exponents. (E,F) Exponents for the scalings of the mean variance ($\widetilde{\alpha}$) and log silence probability inside a cluster ($\widetilde{\beta}$). For low enough CV, such that κ is within surrogate range, exponents (represented by crosses) approach their trivial values of one, close to surrogate results (white dots). Increasing CV, exponents continuously evolve to a stable value. (G,H) Exponent $\widetilde{\mu}$ for the scaling of the covariance matrix eigenvalues and exponent $\widetilde{z}$ for the scaling of the mean autocorrelation decay time. In these cases, state dependent analysis does not directly impact the scaling exponents values, although exponents obtained from low CV trials, like surrogate data, fail to achieve a good power-law fit.

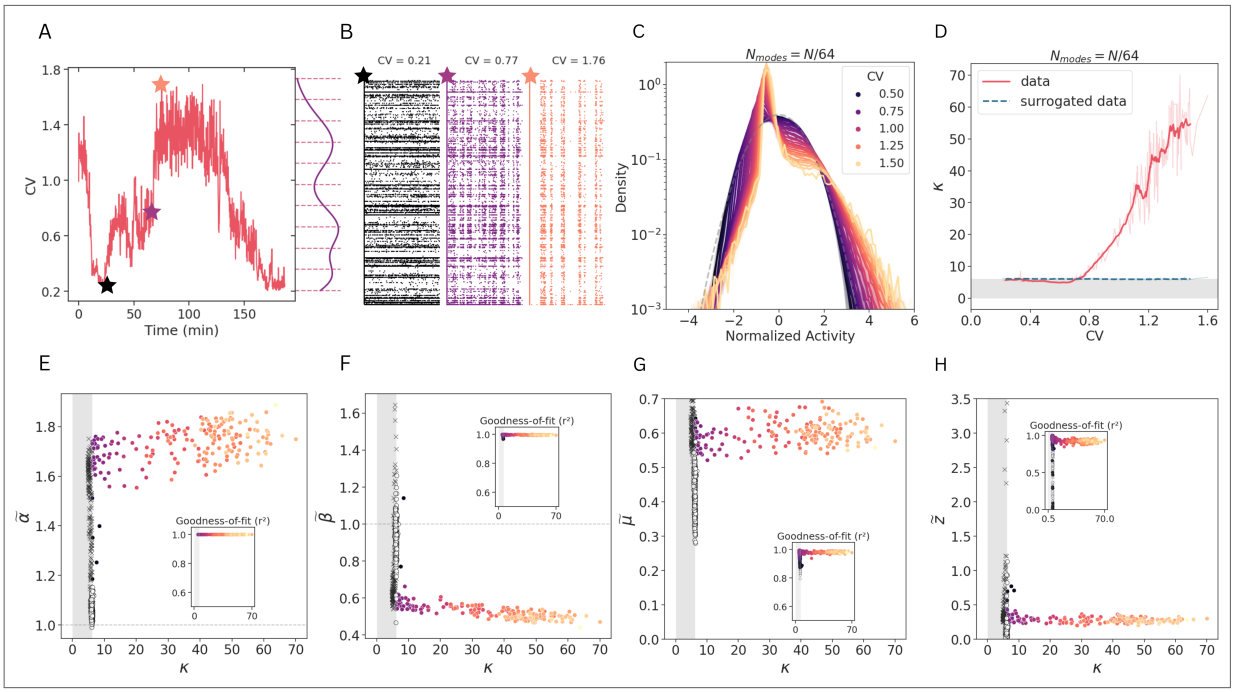

Source: (CASTRO et al., 2024)

(Fig. 29E).

It's worth highlighting that, below the characteristic CV value, the kurtosis can still fluctuate above and below the line we designated as our scaling criterion (grey stripe in Fig. 28D). We thus calculate the joint probability $P(\text{scaling}, \text{CV})$ (see Appendix B), which skewed towards higher CV values when scaling was present and lower CV values when it was absent (Fig. 29G). Overall, we note the presence of the scaling regime the majority of the data analysis time across subjects, accounting for 76% of the entire duration (Fig. 29G). However, the non-scaling regime remains significant. These metrics were also computed individually for each subject (refer to image panels in Appendix B), resulting in $72\% \pm 21\%$ of the time spent within

Figure 29 – (A,B,C,D) Averages (bars) and standard deviation (vertical lines) of state-dependent scaling exponents of each subject (darker shades with white contour represent surrogate results). Dashed horizontal lines are group averages. (E) Kurtosis as a function of CV for each subject. Results for real (surrogate) data in solid (dashed) lines. Hatched area represents the region where both scaling and no-scaling may be found for a given subject (also depicted in G for the group average). (F) $P(CV)$ for each subject. (G) $P(CV, scaling)$: probability densities of CV for trials that do or do not exhibit scaling. Hatched area covers the range of CV where both scaling and no scaling may be found, and a vertical line at $CV^* = 0.70$ marks the point at which scaling and non-scaling are equiprobable. (H) $P(scaling|CV)$: conditional probability of finding scaling given a CV value.

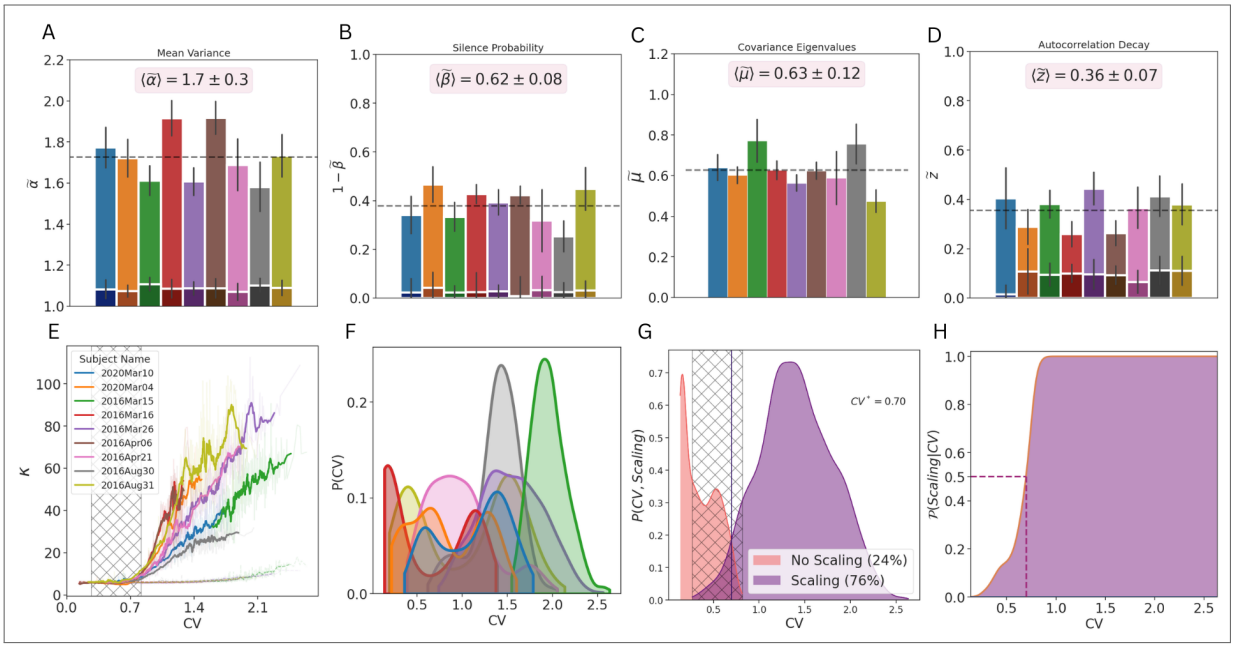

Source: (CASTRO et al., 2024)

the scaling regime when averaged.

Alternatively, we also calculate the conditional probability $P(\text{scaling}|\text{CV})$ which, for the group data, reveals a characteristic CV value at half-height of 0.7 (Fig. 29H). This parameter can be estimated for each subject and then averaged, resulting in a group-average $\langle CV \rangle_g = 0.72 \pm 0.06$ (see appendix C).

3.4 IN AND OUT OF CRITICALITY?

In summary, the present study showed that it is possible to consistently find signatures of scale invariance in data from the anesthetized rat's visual cortex, as assessed by the PRG methodology. Interested in how different cortical states may affect scaling relations in brain activity statistics, we used the CV parsing prescription from Fontenele *et. al.* (FONTENELE et al., 2019) to apply the PRG analysis in a state-dependent manner. As we scrutinized data with increasing levels of spiking variability, we found that the scaling criterion we introduced

was satisfied solely beyond a characteristic threshold of CV. Moreover, the exponents below threshold gradually transitioned from trivial values to non-trivial ones. In the presence of nontrivial scaling, exponents were relatively stable.

Remarkably, the temporal evolution of CV varies considerably among the nine analyzed rats. Despite these differences, all of them surpass the threshold distinguishing between scaling and non-scaling regimes within the same range of CV. This implies that, to some degree, we can deduce the presence of scale-invariant dynamics within a specific time window based on its spiking variability alone.

What was found in the present work is in sharp contrast with previous analyses in the same dataset involving avalanche criticality (FONTENELE et al., 2019). Using CV as a proxy for a control parameter of the system, avalanche scaling exponents were observed only within a narrow range of intermediate CV values. In contrast, PRG results indicate that a large portion of possible CV values correspond to a narrow range of parameter values close to a critical point, as previously suggested by a model (CARVALHO et al., 2021). If we view scaling as a sufficient indicator of a second-order phase transition, our findings suggest that the system oscillates in and out of criticality, with approximately three-quarters of the experimental duration spent in a scaling regime, on average.

In recent years, a lively debate has unfolded regarding whether the non-trivial, scale-free statistics observed in brain activity stem from type-1 criticality (scale-invariant avalanches (BEGGS; PLENZ, 2003)), type-2 criticality (edge-of-chaos (DAHMEN et al., 2019)), or a combination of these, which are not necessarily mutually exclusive (O'BYRNE; JERBI, 2022). Additionally, considering that only a small fraction of the cortex is typically measured, an alternative explanation involving multiple external drivings has been shown to be possible, as it can also result in scale-invariant statistics (MORRELL; SEDERBERG; NEMENMAN, 2021). Irrespective of the underlying cause, the intermittent nature of self-similarity in cortical dynamics invites us to conceive mechanisms that could cause this phenomenon. It may signify, for instance, a hallmark of self-organized quasicriticality, as proposed in a family of models with homeostatic dynamics (KINOUCHI; PRADO, 1999; COSTA; COPELLI; KINOUCHI, 2015; CAMPOS et al., 2017; COSTA; BROCHINI; KINOUCHI, 2017; KINOUCHI et al., 2019; GIRARDI-SCHAPPO et al., 2020; KINOUCHI; PAZZINI; COPELLI, 2020; FOSQUE et al., 2021).

The PRG framework has recently been applied to spiking data from non-anesthetized animals (MORALES; SANTO; MUÑOZ, 2023). A natural progression from this analysis could involve implementing the state-dependent approach outlined in our study such kind of dataset. In this

way, one could examine to which extent the results presented here still hold under more natural conditions. The fact that asynchronous states in non-anesthetized animals exhibit scale-free statistics (MORALES; SANTO; MUÑOZ, 2023), whereas they do not under urethane anesthesia, implies that not all asynchronous states are equivalent. Indeed, this observation should not come as a surprise, considering the obvious behavioral disparities between the two conditions. On the flip side, this emphasizes the need of designing novel tools to characterize asynchronous states electro-physiologically. This is because both awake and urethane-anesthetized cortices exhibit similar coefficient of variation (CV) values and pairwise correlation structures, currently standard methods for discerning cortical states. (HARRIS; THIELE, 2011; FONTENELE et al., 2019).

Finally, it is also noteworthy that any high-dimensional data able to undergo binarization may be analyzed under the phenomenological renormalization scheme, as it is model-independent. Subsequent studies could therefore probe the presence of scale invariance across various experimental setups and even novel systems.

3.5 EXTENDED RESULTS: INSPECTING SINGLE- AND MULTI-UNIT ACTIVITIES

The utilization of both Single-Unit Activity (SUA) and Multi-Unit Activity (MUA) (as detailed in Sec. 2.2.1.1) might raise concerns about potential distortions when combining these distinct types of activity in the PRG procedure. For instance, a single MUA signal may encompass spikes from multiple neurons, thereby blurring the definition of a "cluster size." Additionally, MUAs generally exhibit higher firing rates compared to SUAs, which in turn could lead to a bias in the PRG procedure that favors clustering MUAs together. Consequently, this bias could result in some clusters representing significantly more actual neurons than others.

We investigate these concerns by computing the fraction of actual MUA+MUA, SUA+SUA, and SUA+MUA pairs in the initial step of the PRG procedure across all 30-second time windows. We then compare these fractions with what would be expected from randomly pairing MUAs and SUAs. For instance, if a given dataset contains s SUAs and m MUAs, then the total number of possible pairs is calculated as $T = \binom{s+m}{2}$. The fractions of possible MUA+MUA, SUA+SUA, and SUA+MUA pairs are, respectively, $\binom{m}{2}/T$, $\binom{s}{2}/T$, and sm/T. If there were indeed a bias in the PRG procedure, one would anticipate observing a significantly larger fraction of MUA+MUA pairs than predicted by chance. However, we find the opposite trend in the data (Fig. 30A). The proportion of MUA+MUA, SUA+SUA, and SUA+MUA pairs formed

Figure 30 – Comparison of how MUAs and SUAs are joined together by the PRG. (A) illustrates the process by which the PRG combines pairs of variables during the initial iteration for a single subject. For each of the analyzed time windows, we calculated the ratio of MUA+MUA, SUA+MUA and SUA+SUA pairs. Then, we compared their averages (solid lines) with the ratio expected from random pairings (dashed lines).We can see that the PRG does not favor combining MUAs with themselves. In (B), we examine the final phase of the procedure, i.e. the final iteration of the PRG. In our case, at this stage coarse-grained variables represent sums of 64 raw variables. We calculate the ratio of MUAs to SUAs within each cluster. As we can see, this ratio closely mirrors that of the raw variables, indicating that MUA units are not inherently predisposed to being combined.

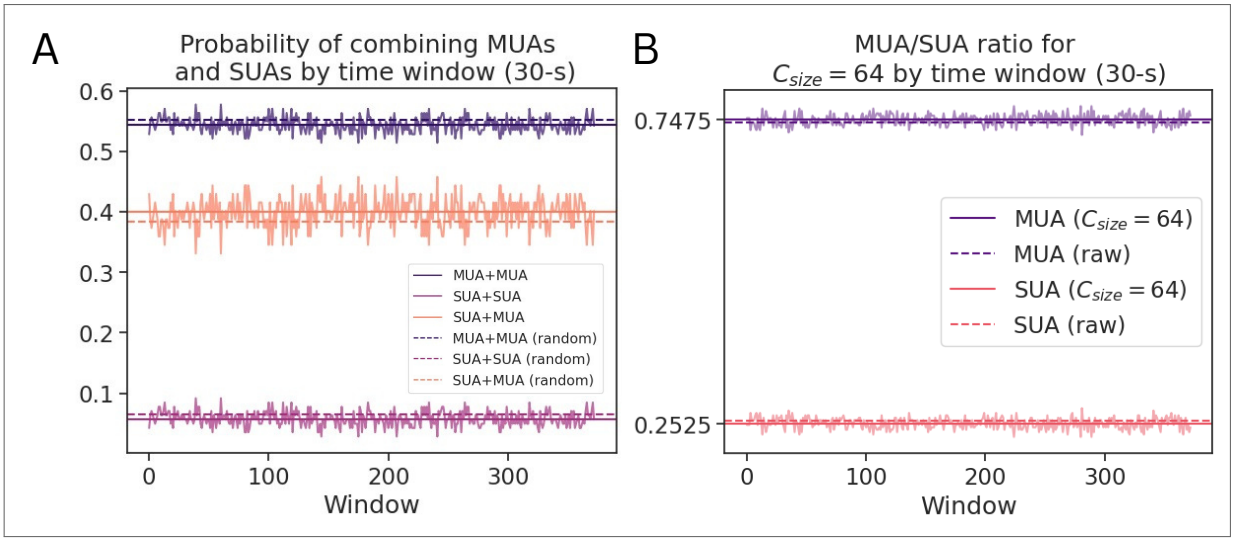

Source: (CASTRO et al., 2024)

by the PRG procedure in its initial iteration is close to what one would obtain from random pairings. Moreover, we can also look at the opposite end of the procedure. This time, we evaluate the ratio of MUAs to SUAs at the last iteration of the PRG, where our coarse-grained variables consist of sums of 64 raw variables. Again, we can see that the ratio of MUA/SUA inside each cluster is essentially the same as the initial ratio of raw variables, further confirming that MUA units are not more likely to be combined.

3.6 EXTENDED RESULTS: DIFFERENT TEMPORAL RESOLUTIONS

One matter that currently remains unconsidered in coarse-graining analysis is how different temporal resolutions impact results. In fact, the choice of time bin durations chosen to define statistical events is an ever present issue, and remains mostly an open question in regard to assessing criticality in experimental data. For most of the analyses, we fixed all bin durations to 50-ms in order to allign with our main sources for result comparison (FONTENELE et al., 2019; CARVALHO et al., 2021). Nevertheless, we repeated the PRG procedure in a single subject's data, to examine how different temporal scales change previous results obtained.

Figure 31 – Scaling exponents from data binarized with different time bin lengths. Exponents extracted from power-laws gradually shift as we increase the choice bin duration.

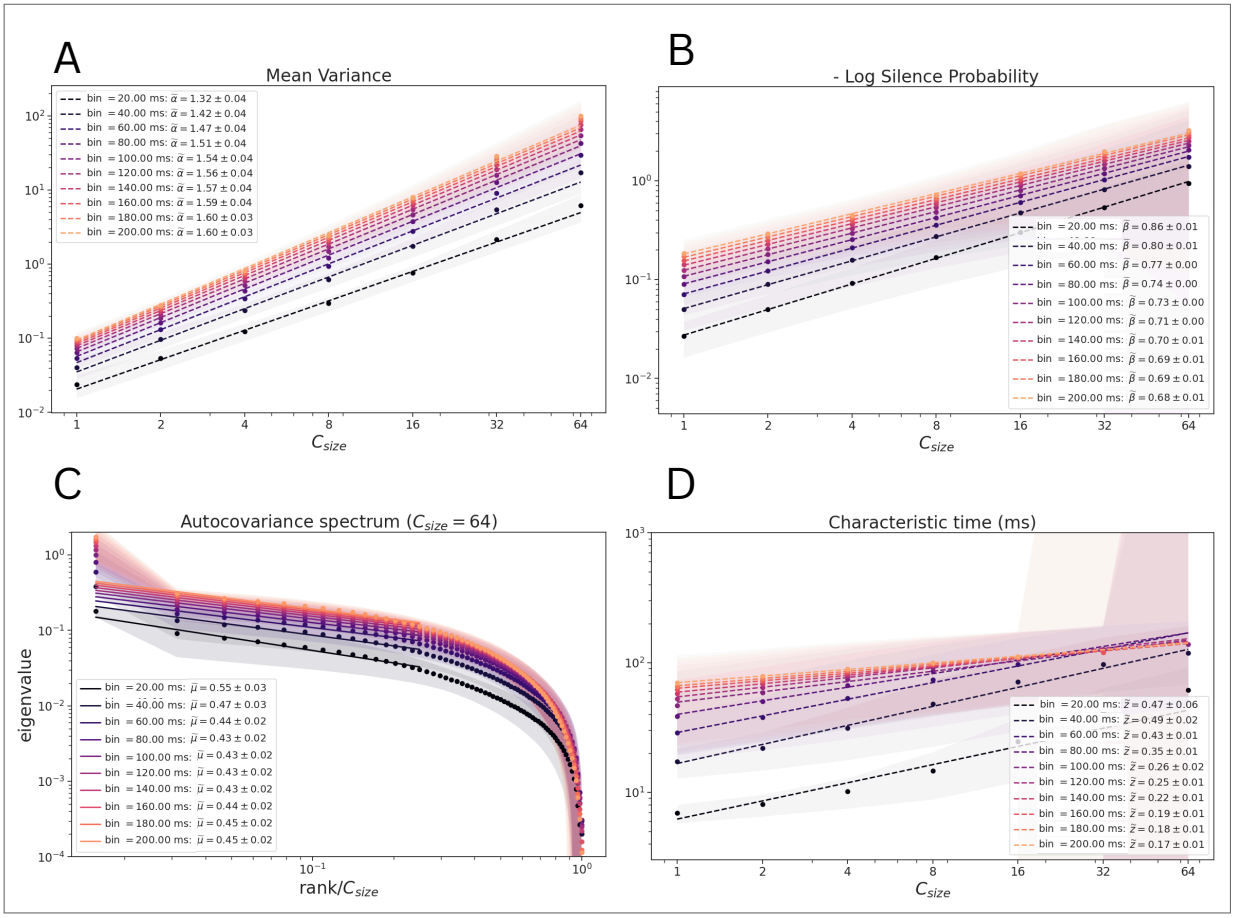

Source: The author.

Unsurprisingly, we find that PRG scaling exponents and distributions are sensitive to bin duration choice (see Figs. 31, 33), as occurs with previous methods used to empirically measure scale invariance (CARVALHO et al., 2021; ZHIGALOV et al., 2015). Interestingly, though, there is a range of time bins where the variation in some of the exponents obtained are linearly related, as shown in Fig. 32. For longer bin durations, the binary patterns within our time series potentially reach a point where they no longer exhibit significant changes between consecutive time bins, making scaling exponents stable. This inference gains support from the observed contrast in activity distributions derived from coarse-grained variables for shorter or longer time bins (Fig. 33). This pattern lasts until the duration of a time bin becomes so long that coarse-grained variables become active at all bins. At this point, exponents are again not stable and may not even make sense, as it is the case for the $\widetilde{\beta}$ of the silence probability (since there is no longer any moments where activity is absent, as in Fig. 33C).

Linear relations between phenomenological exponents are not yet established in the litera-

Figure 32 – Relations between scaling exponents. (A-C) Exponent drift for different time bins (5-700 ms), until reaching a stable value at a few hundreds of milliseconds. (D-F) Exponent planes for $\widetilde{\alpha}$, $\widetilde{\beta}$ and $\widetilde{\mu}$. Lighter colors correspond to longer bin durations.

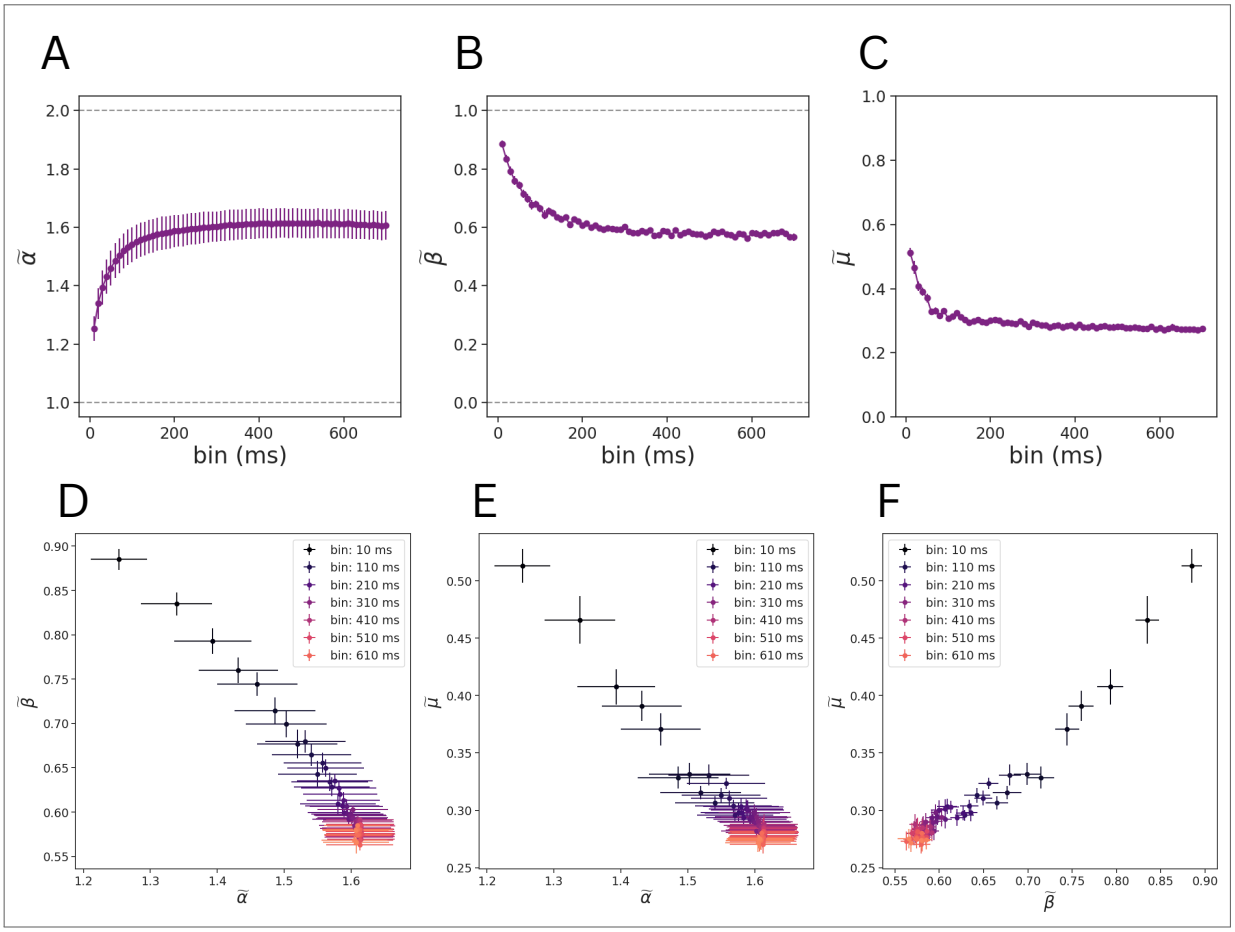

Source: The author.

ture. As we will see in the next chapter, they emerge not only when inspecting changing the choice of temporal resolution, but also in other situations. This issue will be further explored in the following chapter, where we discussed similar findings derived from fMRI data.

Figure 33 – Probability densities of (real-space) coarse-grained variables' activity for different time bin durations. Notice that, for longer time bins (B), the change between consecutive distributions becomes smaller than the initial changes (A). (C) For extremely high values of time bin, most of the time series will be always active, which does not make sense for our data and murks the definition of scaling exponents. Shaded areas are standard deviations across trials.

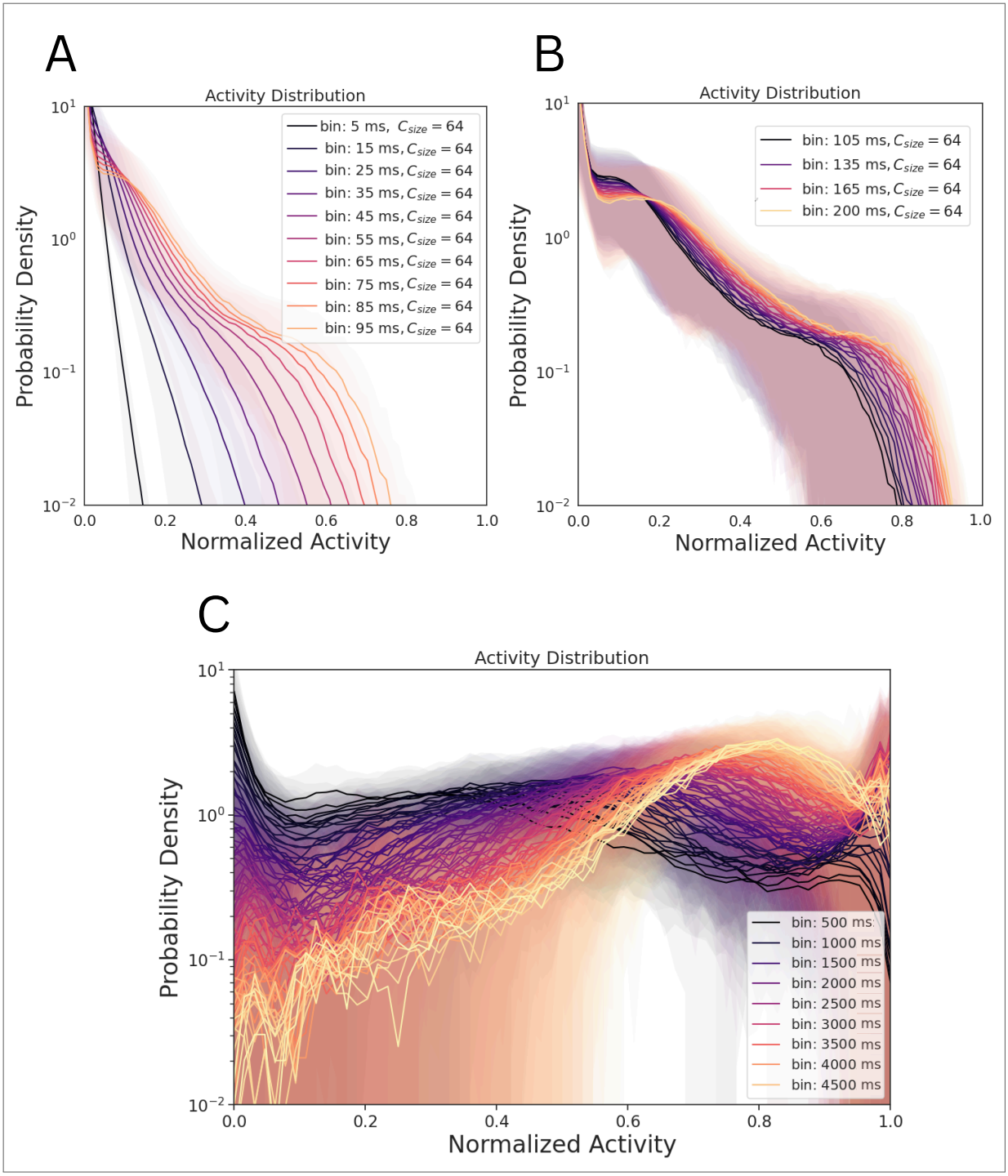

Source: The author.

4 SCALING EXPONENT RELATIONS AND CLINICAL CORRELATIONS IN LARGE HUMAN DATASETS

In this chapter, we develop an application of the PRG method adapted to whole brain rs-fMRI data from humans. We show that different participants within the datasets possess different sets of scaling exponents. Remarkably, the variability between 3 of the 4 exponents is linearly strongly related, which gives us evidence to conclude that, just as there are exponent relations in critical phenomena theory, something similar happens with PRG (*phenomenological)* exponents. We can also compare the subject's different scaling exponents to diverse clinical traits contained in the dataset, indicating potential applications of this method in measuring clinically relevant markers. This kind of advancement would not only broaden the utility of scaling analyses beyond theoretical realms but also make them more accessible and appealing to a wider audience, sparking increased interest in the field.

4.1 WHOLE BRAIN SCALING AND VARIABLE EXPONENTS

After studying the PRG in local spiking data from the rat cortex we move on to a rather different kind of setup: fMRI data from humans. As explained in Sec. 2.2.2.1, fMRI time series are recorded from the entire brain at high spatial resolutions, allowing us to investigate whether we can see similar scale-invariant features at the whole-brain level.

We make use of two different datasets from the Human Connectome Project (HCP): HCP Young Adults (YA), with participants aged 22-35, and HCP Aging, aged 36-100+ (ELAM et al., 2021). In both datasets, every participant went through two separate recording sessions. With these, we can retest any results we find, giving them more robustness. Importantly, the preprocessing pipeline for the YA and the Aging datasets are not the same (HARMS et al., 2018). Therefore, we avoid comparing them directly. Unless otherwise stated, results shown here will refer to the YA set.

To process the signals into binary time series, we use Schaefer's 1000 parcel atlas, which subdivides the brain into 1014 regions of interest (ROIs)(SCHAEFER et al., 2018). Then, we binarize the continuous signals by using a z-score upper threshold: for each ROI, we make $\sigma_i(t) = 1$ if the continuous signal was above $z_{threshold}$ at time t and $\sigma_i(t) = 0$ otherwise (see Sec. 2.2.2.2)(PONCE-ALVAREZ; KRINGELBACH; DECO, 2023). In this section, we fix $z_{threshold} = 2$ and leave a more detailed discussion regarding threshold choices to Appendix C.

Figure 34 – (A-C) Review of the PRG pipeline for fMRI data (Sec. 2.2.2.2) and (D-G) scaling exponents for a single subject.

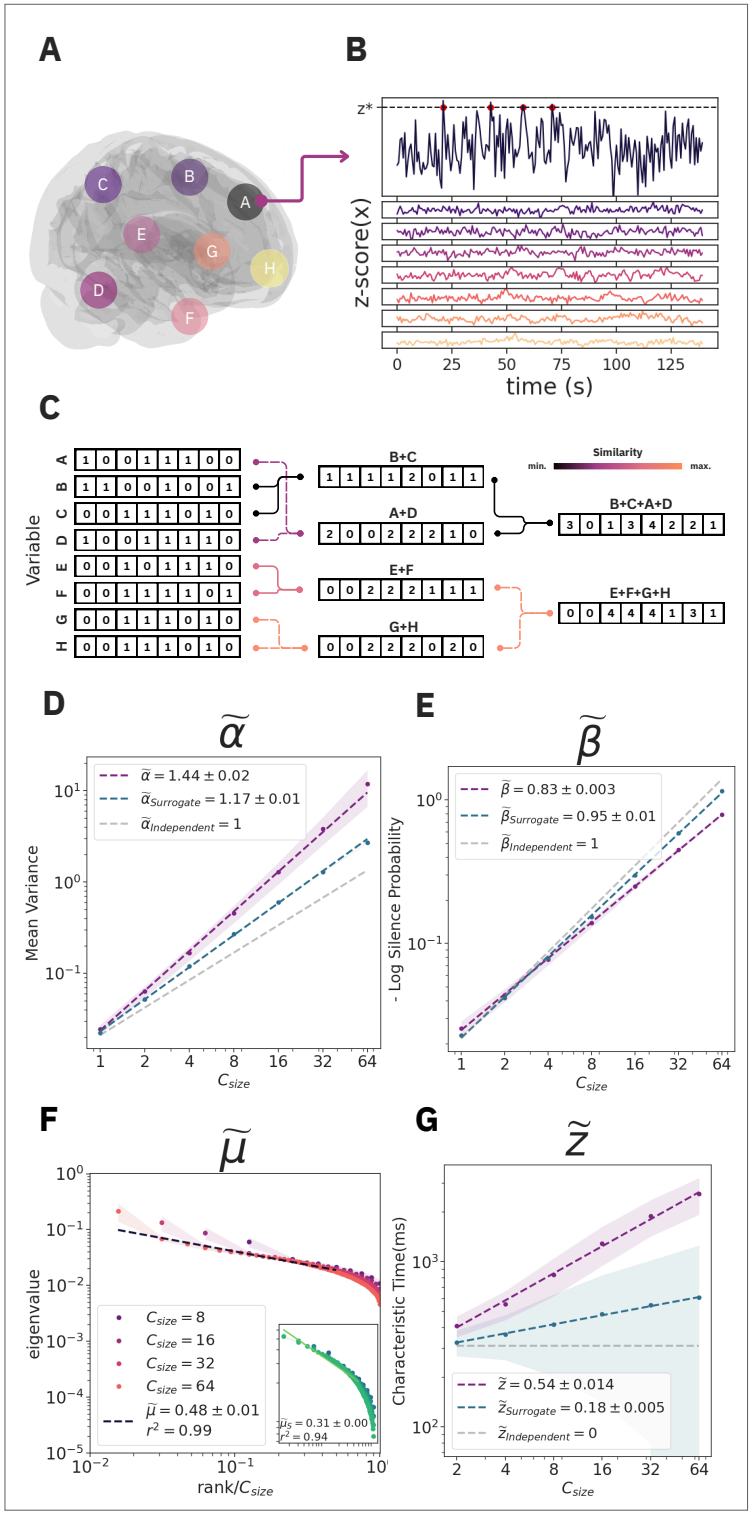

Source: The author.

We begin by showing the PRG procedure in 560-s time windows[1] of a single participant

[1] The slightly shorter window length, in comparison to the case of the anesthetized rats, allows us to have errorbars to exponents calculated from a single participant (Fig. 34D-34G), despite the short recording sessions (<30 min).

from the YA dataset, whose exponents can be seen in Fig. 34D-34G. Given that we are able to find good power law adjustments to individual participants, we proceed to analyze the exponent values at the population level. Despite being relatively stable across different sessions, scaling exponents show considerable variability (Fig. 35). We also show the activity distribution of coarse-grained variables averaged across all participants, and contrast it to its surrogate counterpart (Fig. 35E).

Figure 35 – (A-D) Spread of scaling exponents across all subjects (smoothed with a gaussian kernel for better visualization). The two axes compare the resulting exponent for the first and second recording sessions of each subject. Authentic (surrogate) data are shown in purple (yellow) gradient, with darker colors corresponding to higher densities. YA (Aging) dataset are shown in main figures (insets). Surrogate values in (C) were omitted because power law adjustments had poor ($r^2 < 0.85$) quality. (E) Activity distribution of coarse-grained variables in the last iteration ($C_{size} = 64$) averaged across all subjects in the YA dataset.

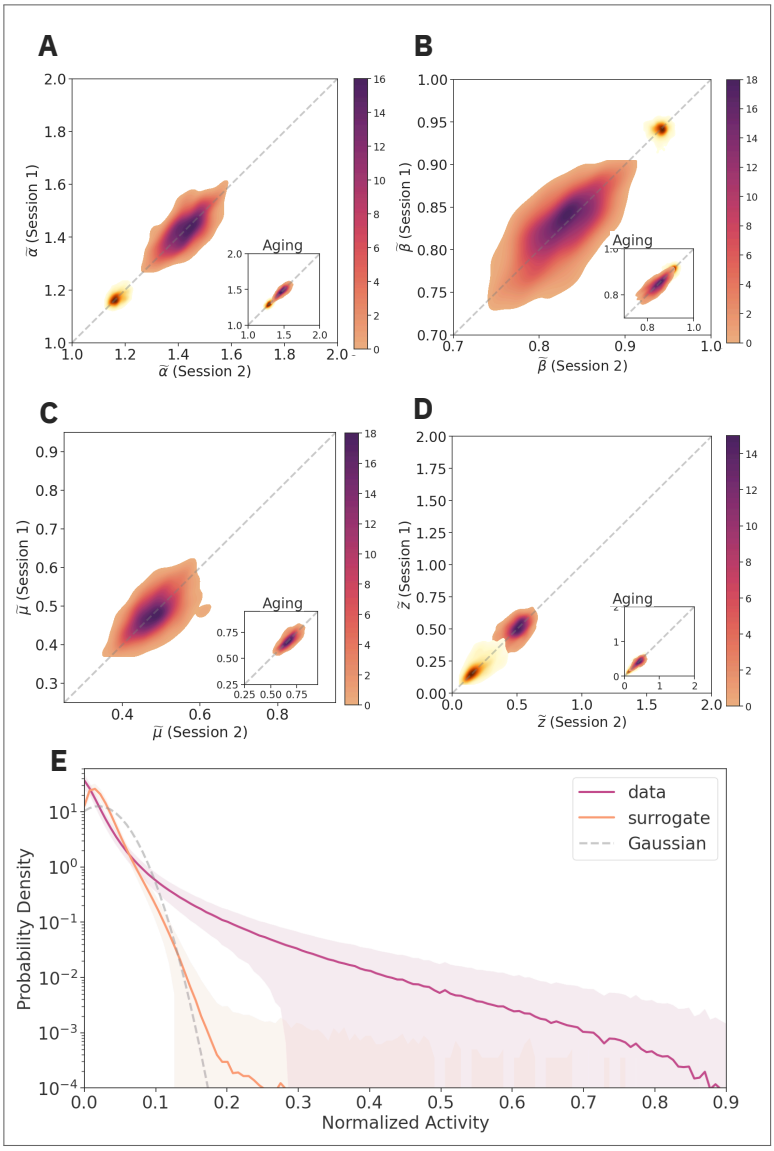

Source: The author.

4.2 EXPONENT RELATIONS: RECONCILING EXPONENT DIVERSITY?

The large spread in the values of the exponents has not received significant attention in the literature, with prior studies primarily reporting their averages and standard deviations (MORALES; SANTO; MUÑOZ, 2023; PONCE-ALVAREZ; KRINGELBACH; DECO, 2023; CASTRO et al., 2024). However, here we find a key feature in those variations: they are *strongly* interdependent (Fig. 36A-36C). In fact, the exponents $\widetilde{\alpha}$, $\widetilde{\beta}$ and $\widetilde{\mu}$ are linearly related, falling nicely onto a line in 3-D space (Fig. 36D). In a complete theory, the relationship among scaling exponents would be derived from an effective theory (MESHULAM et al., 2018). Here such relationships are found experimentally, by graphing exponent values in function of one another. As we can see, only two out of the four phenomenological exponents seem to be independent: exponent $\widetilde{z}$ is the only not related with the others (Fig. 37B). This kind of finding would be hard to find in previous experiments, because invasive animal setups tend to have, at best, about a dozen samples. The large sample size of the HCP fMRI datasets is then what uncovers these previously unknown relations.

Importantly, this level of correlation (the coefficient of determination r^2 in Figs. 36, 37 is the square of the Pearson coefficient) found in the relations are much higher than anything usually driven by biological mechanisms. This makes unfeasible the explanation that some combination of biological factors would push independent exponents into an apparent relation. Hence, the most plausible hypothesis is that the scaling relations between exponents can be found at a theoretical level.

In addition to the relations between the four scaling exponents established by the original method, we find that higher statistical moments of coarse-graining (up to $m_4 = \langle(\sigma - \langle\sigma\rangle)^4\rangle$) also scale, giving exponents which are also linearly dependent to the others (Fig. 37A).

We have also measured a different exponent, which comes from the magnitude of the dominant eigenvalue in the covariance spectrum and also indicates scale invariance

$$\lambda_1(C_{size}) \sim (C_{size})^{\epsilon}. \tag{4.1}$$

Notice in Fig. 34F, for example, how the highest eigenvalue in each coarse-graining iteration also seems to follow a power law. This impression was the motivation for the calculation of this exponent. This exponent is also tied to the others through a linear relation. Summarizing

Figure 36 – The PRG exponents $\widetilde{\alpha}$, $\widetilde{\beta}$ and $\widetilde{\mu}$ are strongly linearly related in the HCP-YA dataset. (A-C) shows each relation pair by pair and (D) shows the approximately 1-D line formed by the exponent relations combined in 3-D space, color graded by the μ (z-axis) value.

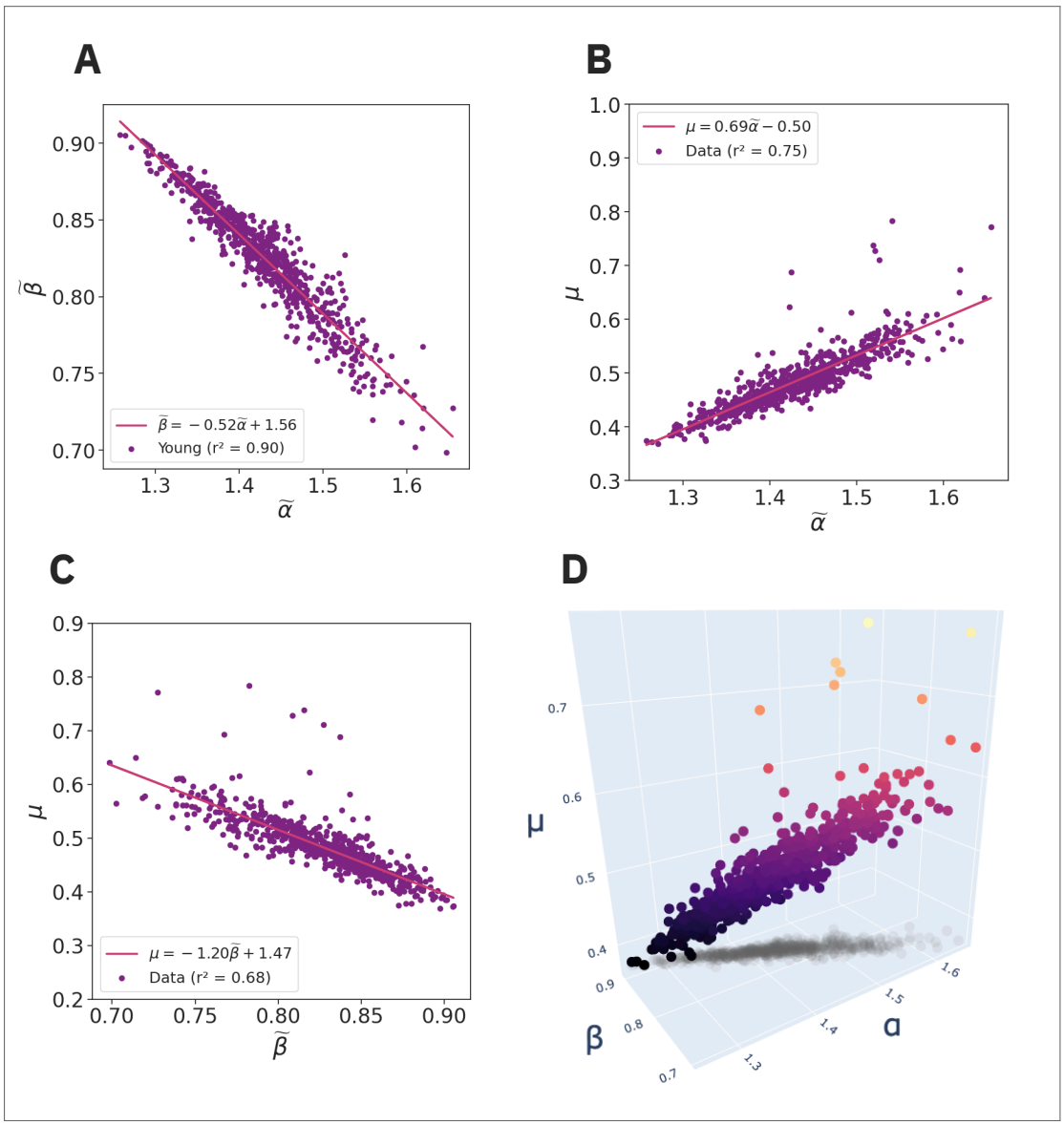

Source: The author.

all relations, we have:

$$\widetilde{\beta} \simeq \frac{3-\widetilde{\alpha}}{2}, \tag{4.2}$$

$$\widetilde{\mu} \simeq \frac{2}{3}\widetilde{\alpha} - \frac{1}{2}, \tag{4.3}$$

$$\widetilde{\mu} \simeq -\frac{5}{4}\widetilde{\beta} + \frac{3}{2}, \tag{4.4}$$

$$\epsilon \simeq \widetilde{\alpha} - 1, \tag{4.5}$$

$$\alpha_3 \simeq 4\widetilde{\alpha} - \frac{2}{3}, \tag{4.6}$$

$$\alpha_4 \simeq 5\widetilde{\alpha} - \frac{4}{5} \tag{4.7}$$

for the exponents from higher order moments. In the absence of a theory, all equalities are approximations.

Figure 37 – (A) Exponent relations between the scaling exponents of higher order moments and the scaling of variance $\widetilde{\alpha}$. Skewness exponent α_3 and kurtosis exponent α_3 are shown in blue and red, respectively. (B) Absence of linear relations in between the autocorrelation decay exponent $\widetilde{z}$ and the other PRG exponents. The straight line show the best fit achieved, $r^2 = 0.34$.(C) Examply of the scaling of the dominant eigenvalue and (D) its respective exponent ϵ compared to the α exponent across samples.

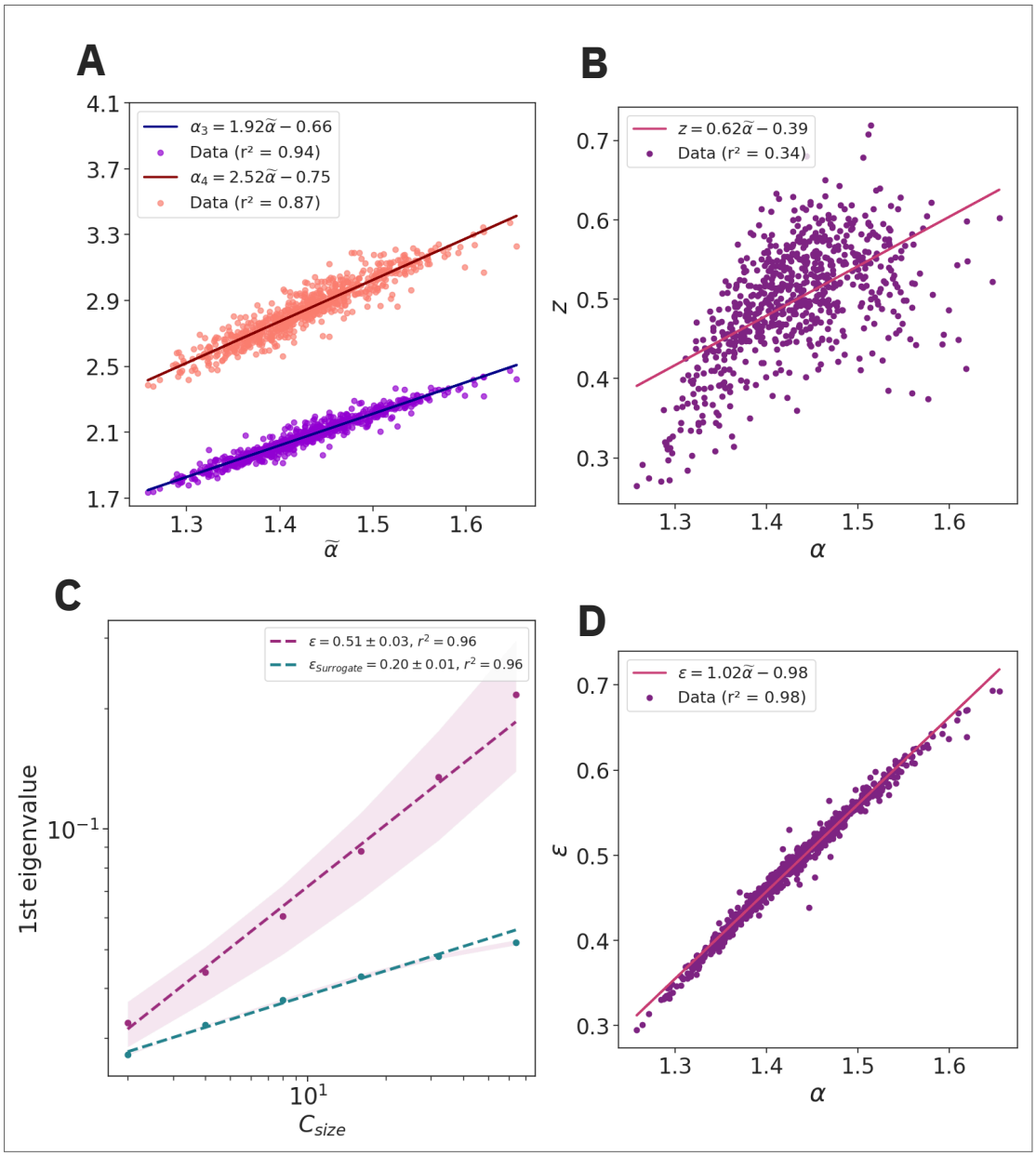

Source: The author.

4.3 CLINICAL METADATA AND SCALING EXPONENTS

Another aspect which can be explored in our setup is the relation between scale invariance quantifiers and various clinical traits of the subjects. This perspective is specially exciting in our setup when considering, again, the large number of volunteers in the experiment. Up to 2020, all the previous works connecting criticality and clinics on fMRI *combined* had less than half of the amount of samples in the HCP datasets alone (ZIMMERN, 2020). While a complete clinical analysis is beyond the scope of this work, we went through a basic exploration of the dataset contents.

We begin by comparing exponents from female (F) and male (M) subjects of the YA dataset, using violin plots of the distributions[2]. We find that the two categories have essentially the save average values (within the exponent adjustment errorbar) and similar standard deviations (Fig. 38). Still, the minor differences towards the ends of the distributions are considered statistically significant by the Komolgorov-Smirnoff two-sample test.

Next, we analyse the spread of exponent values relative to the age of the subjects. In the YA dataset, subject ages were registered with only three groups (22-25, 26-30 and 31-35 years), hence we again compare the distributions with violin plots. We find that lower values of exponents are skewed towards older adults, although this difference is again minor, and sometimes not statistically significant when subject to a KS test. However, the Aging dataset allows us to better see the impacts of aging in scaling exponents: in this case, we have a wider range of ages and they are measured in months, allowing for a less coarse analysis. In this situation, we find a consistent decrease (or increase, in the case of $\widetilde{\beta}$) in the magnitude of exponents throughout the years. This result hints that scaling exponents might also serve as potential biomarkers to track changes in the brain over time, specially if future works can make a distinction between healthy and unhealthy aspects of aging with scaling analysis, including the PRG in the recent trend of applying mathematical techniques to categorize the different pathways to aging (FÜLÖP et al., 2020). A simple step in this direction is to search for correlations between scaling and anatomic or behavioral traits of subjects: we show some examples below.

[2] A violin plot is a compact way of showing multiple attributes of a distribution at once. The coloured part is the histogram of the values smoothed by a Gaussian kernel, with more frequent values displayed as parts with larger width. The white dot displays the position of the median, within the inner black box which marks the distance between the first ($Q1$) and third quartiles ($Q3$) of the distribution, called the inter-quartile range (IQR). The rest of the vertical line extends to the the ends of the plot mark minimum ($Q0$) and maximum ($Q4$) values $Q_{4/0} = Q_{3/1} \pm 1.5IQR$. Points beyond these values are considered outliers.

In Figs. 41A and 41C we measure correlations between the $\widetilde{\alpha}$ exponent (of the scaling of the variance in coarse-grained variables) and the total volume of white and grey matter. White matter primarily consists of neuron axons, which are nerve fibers forming the pathways enabling communication between neurons in different parts of the brain; grey matter refers to the outer layers of the brain (cortices), where most neuron cell bodies and dendrites are located. The latter has the strongest impact on PRG exponents out of the two (Fig. 41 only shows the values for the $\widetilde{\alpha}$ exponent, but since they are linearly related, a similar result can

Figure 38 – Exponent distributions by gender. Stars over the violin plots represent p-values for the KS test between samples, and values greater than 0.05 are specified. The difference in average exponent values from the two distributions is small, falling within errorbars. Still, the two-sampled KS test determines there is a significant difference between distributions

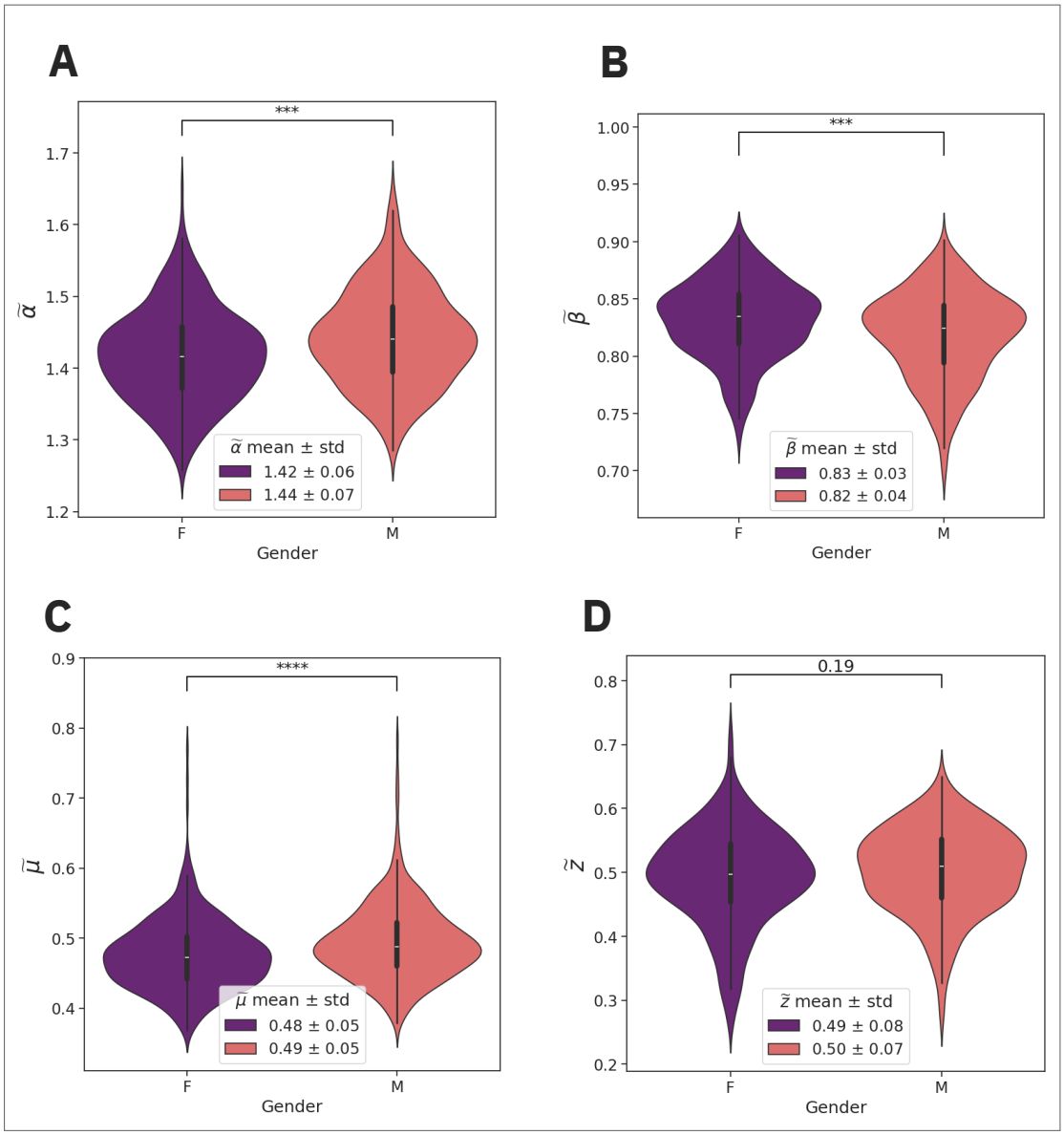

Source: The author.

be find with any of the exponents). This is interesting because the volume of grey matter is influenced by individual habits such as sleep health and amount of physical activity, and is associated to a reduced risk cognitive impairment in later stages of life (ERICKSON et al., 2010; SCHIEL et al., 2023).

We have also found that higher values of $\widetilde{\alpha}$ correlate with higher scores in the Penn Progressive Matrices, which assesses fluid intelligence (Fig. 41B), with a correlation coefficient[3] $\rho_{pearson} = 0.16$. Something similar was done recently with synchronization entropy and

[3] As a small disclaimer, it should be noticed that correlation levels in life sciences are expected to be lower than those from results in physics or chemistry, for example. In general, phenomena in living systems are the product of many codependent factors and it is unlikely that any single measurement will capture all mechanisms simultaneously. Nevertheless, it is still essential that these correlations are statistically

Figure 39 – Exponent distributions by age group for the YA dataset. Stars over the violin plots represent p-values for the KS test between samples, and values greater than 0.05 are specified.

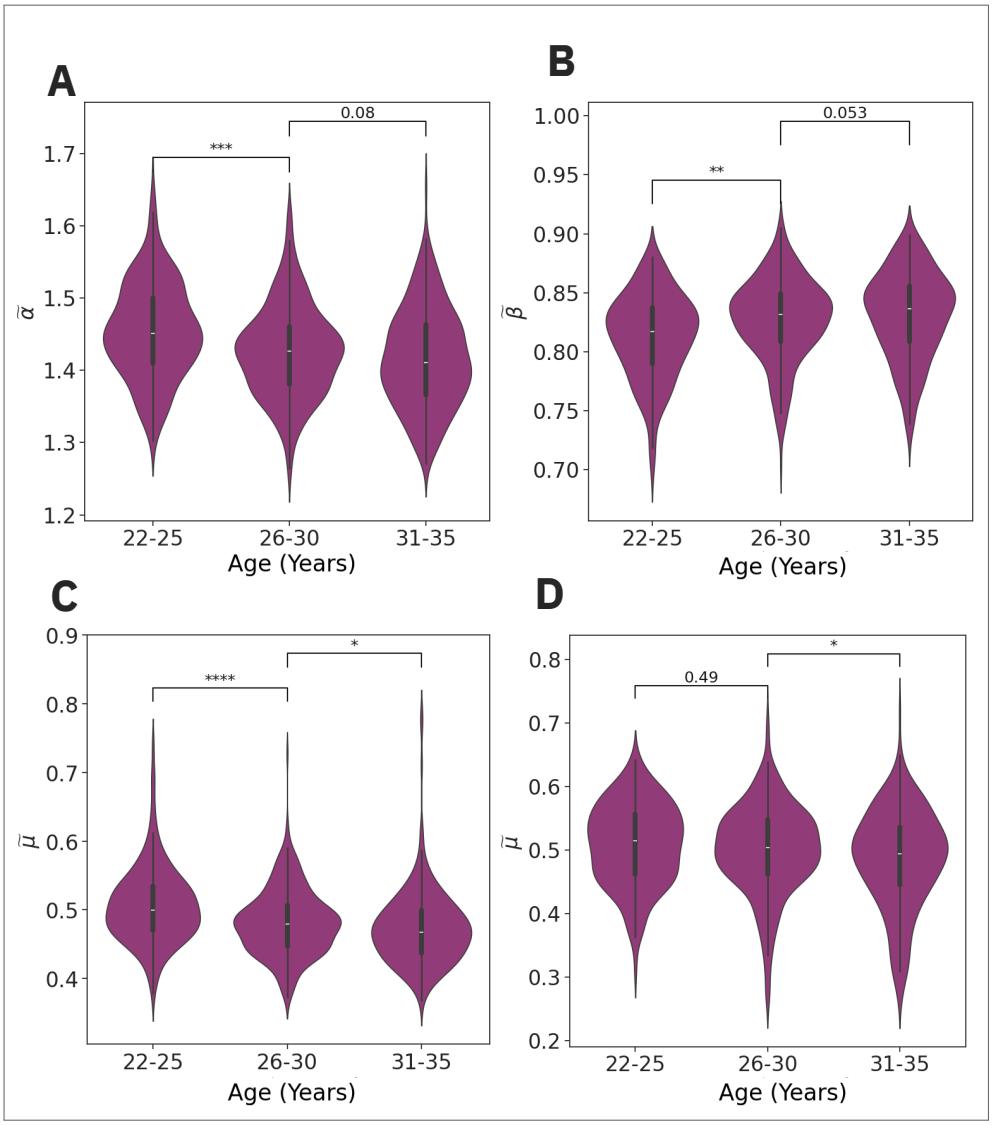

Source: The author.

Figure 40 – Exponent distributions by age (in years) for the Aging dataset.

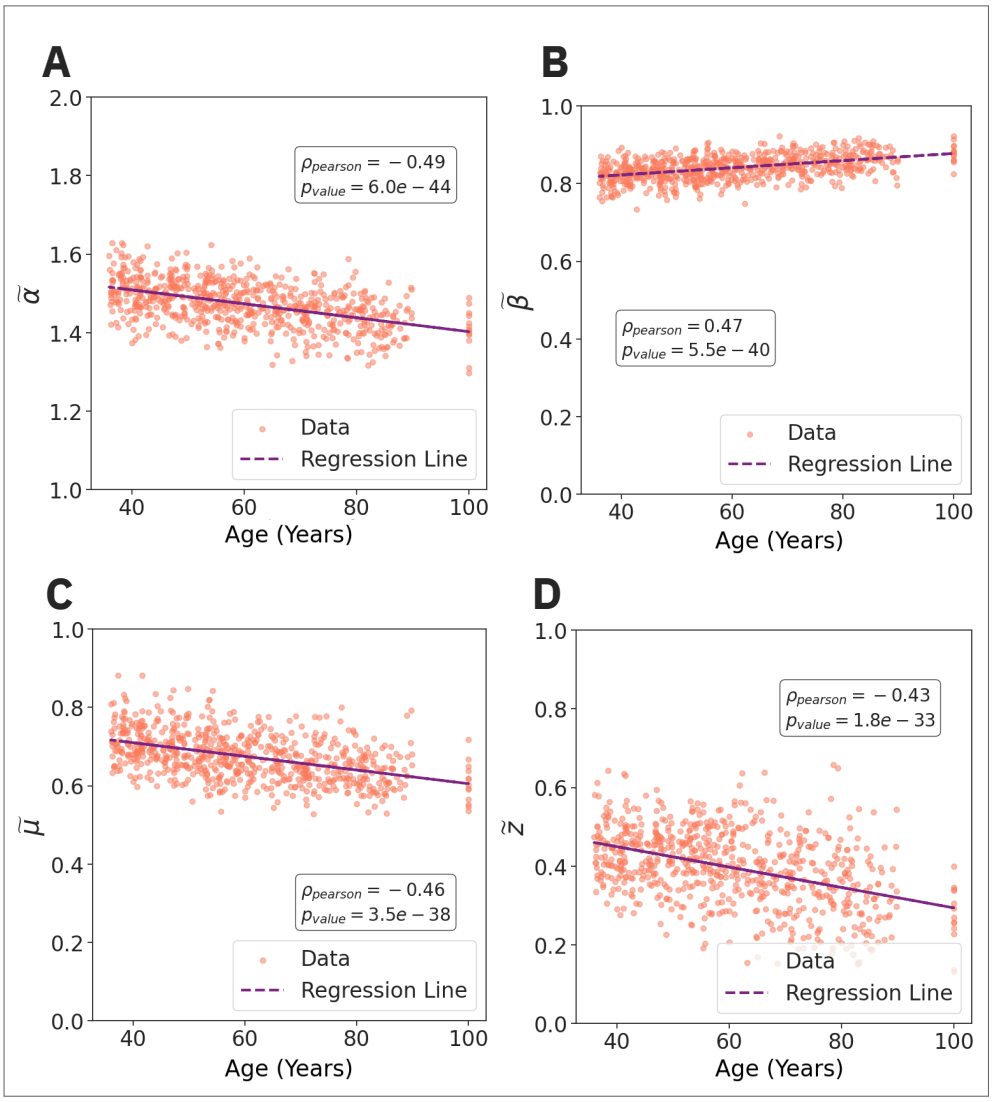

Source: The author.

avalanche analysis (XU; FENG; YU, 2022), where it was suggested that the neural dynamics of human participants with higher fluid intelligence and working memory scores are closer to criticality. Fluid intelligence is believed to be not the product of any single brain area but the integration of them. Thus, multi-scale metrics like PRG exponents can be thought of as natural candidates to better quantify the dynamics of this aspect of cognition and, most importantly, to better understand unhealthy cognitive decline.

Finally, we look for possible relations involving the exponent $\widetilde{z}$. Given its apparent independence from the other exponents, we can look for connections particular to it. We find that it is correlated with beta oscillation band (13-30 Hz) peak of magnetoencephalogram (MEG) signals. These were recorded in a smaller ($\sim$100) subset of the participants. The prominence

significant, *i.e.* have small p-values (typically $p < 0.05$).

Figure 41 – Correlations between the $\widetilde{\alpha}$ exponent and the (A) white matter volume of the brain, (B) the average number of correct responses in the Penn Matrices (PMAT24) fluid intelligence test, (C) grey matter volume. (D) Correlation between the $\widetilde{z}$ exponent and the value of the beta frequency peak from the associated MEG experiment (available for a subset of the subjects).

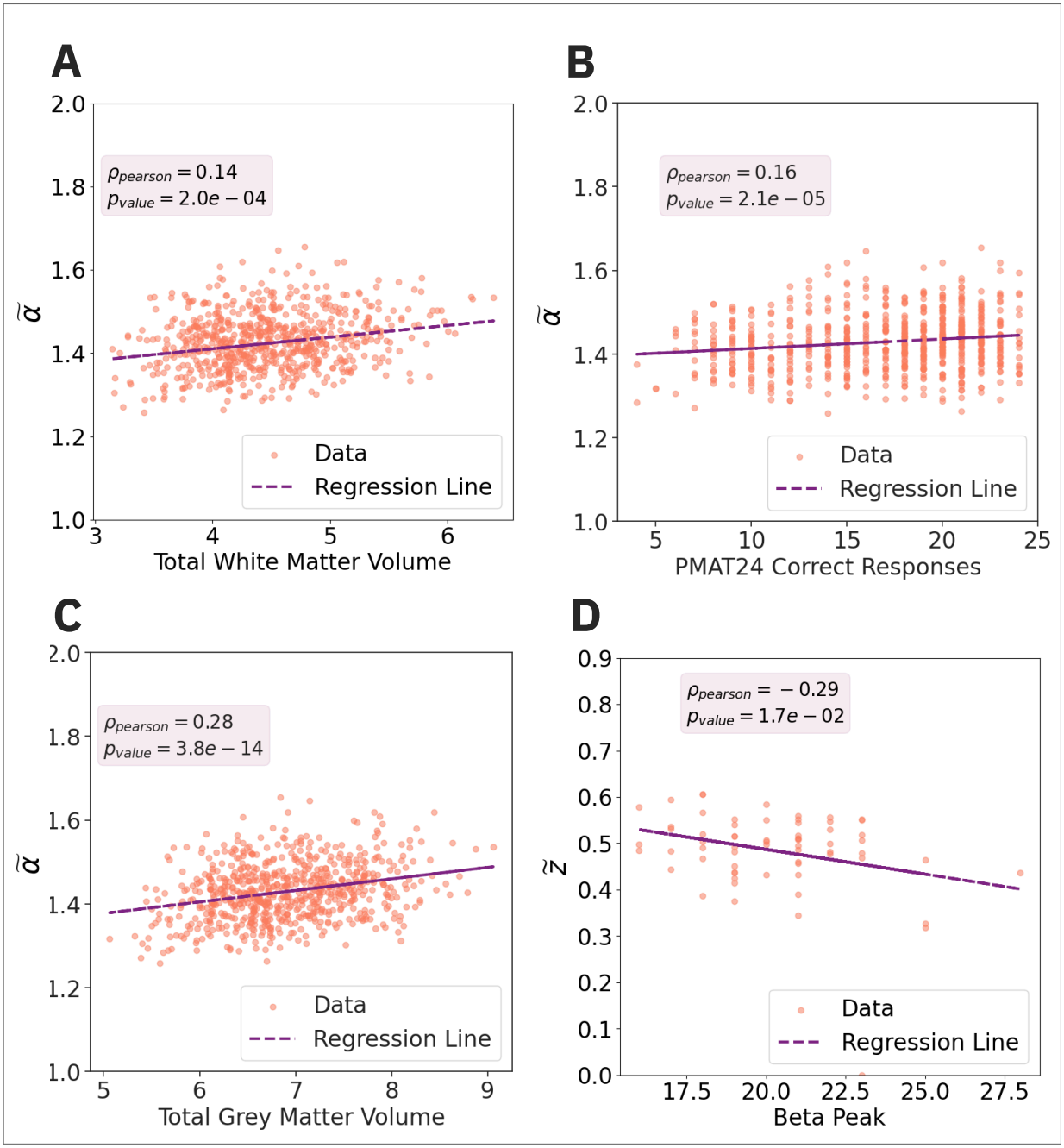

Source: The author.

of beta oscillations in brain signals is associated to visual-motor integration and motor control (WANG, 2010; BASTOS et al., 2015).

Overall, we believe that the existence of correlations between scale-invariant statistics in the brain and clinical factors of the experiment participants can open avenues for the development of clinical analyses based on the PRG method. Proposing the adoption of physics

and mathematics methodologies in clinical applications is not exclusive to this work; rather, it has seen a marked increase in recent years, as indicated by the literature (TIJHUIS et al., 2021; ESCRICHS et al., 2022; ZIMMERMANN et al., 2024; HINDRIKS et al., 2024). Despite being in its early stages, approaches like these hold potential of driving innovation in biomedical research.

4.4 EVALUATING THE ROBUSTNESS OF THE PRG PROCEDURE

Before closing this chapter, we address a couple of technical points of the PRG method. We argued in Sec. 3.4 that this procedure can be applied to any high-dimensional data. If that is the case, it is of interest to discover whether its results are robust with respect to changes that may be necessary in different datasets.

The first aspect we analyze is the choice of similarity metric used to pair up variables into coarser-grained ones. As discussed in Sec. 2.1.3, the decision to use pairwise Pearson coefficients in the coarse-graining procedure is arbitrary. But this should not be an issue (in principle), given that the RG obtain its results from flowing across many scales, and minor discrepancies from the details of the blocking rule should should not matter at the fixed point. Is this intuition still true for our phenomenological applications, where systems are not only finite but we are limited to a very low number of PRG transformations (tipically $k = 6, 7, 8$)?

To answer this question, we repeat the procedure for the same data (the same subject from Fig. 34), replacing the Pearson correlation with 4 other similarity metrics: the Spearman rank correlation (SM), mutual information (MI), cosine distance (CD) and Hamming distance (HD) (detailed in Sec. 2.1.3). Notice that the last method, HD, simply counts how many entries are equal between two vectors, while completely ignoring the actual values inside them: we purposefully put it here as a *bad* metric, to test the limits of the coarse-graining. What we find is that the method is very robust with respect to the choice of pairing rule, giving the same exponents within error bars for most of the methods (Fig. 42). Predictably, the only method that disagrees with the others in exponent values was the Hamming distance.

The other aspect we intend to evaluate is the convergence of the method to a fixed point. Given the limitation on the number of iterations imposed by the number of variables in our data, we wish to have a way of knowing whether the amount of coarse-graining steps available is enough to take the coarse-grained variables distribution to a fixed form. Here we propose to do so by using a distance measure between the activity distribution of coarse-grained variables from successive iterations, in this case calculating the Wasserstein distance

(Sec. 2.1.4) between them.

We find that, regardless of similarity metric, the difference between distributions tends to diminish after the first few iterations. Still, with the amount of iterations we are able to track, we cannot see a clear sign that the distribution is approaching a fixed form (which

Figure 42 – PRG exponents obtained using different similarity metrics to pair coarse-grained variables. In order, these metrics are: Pearson coefficient (P), Spearman rank correlation (SM), mutual information (MI), cosine distance (CD) and Hamming distance (HD). The last was intentionally chosen poor metric, in order to test the limits of the PRG method.

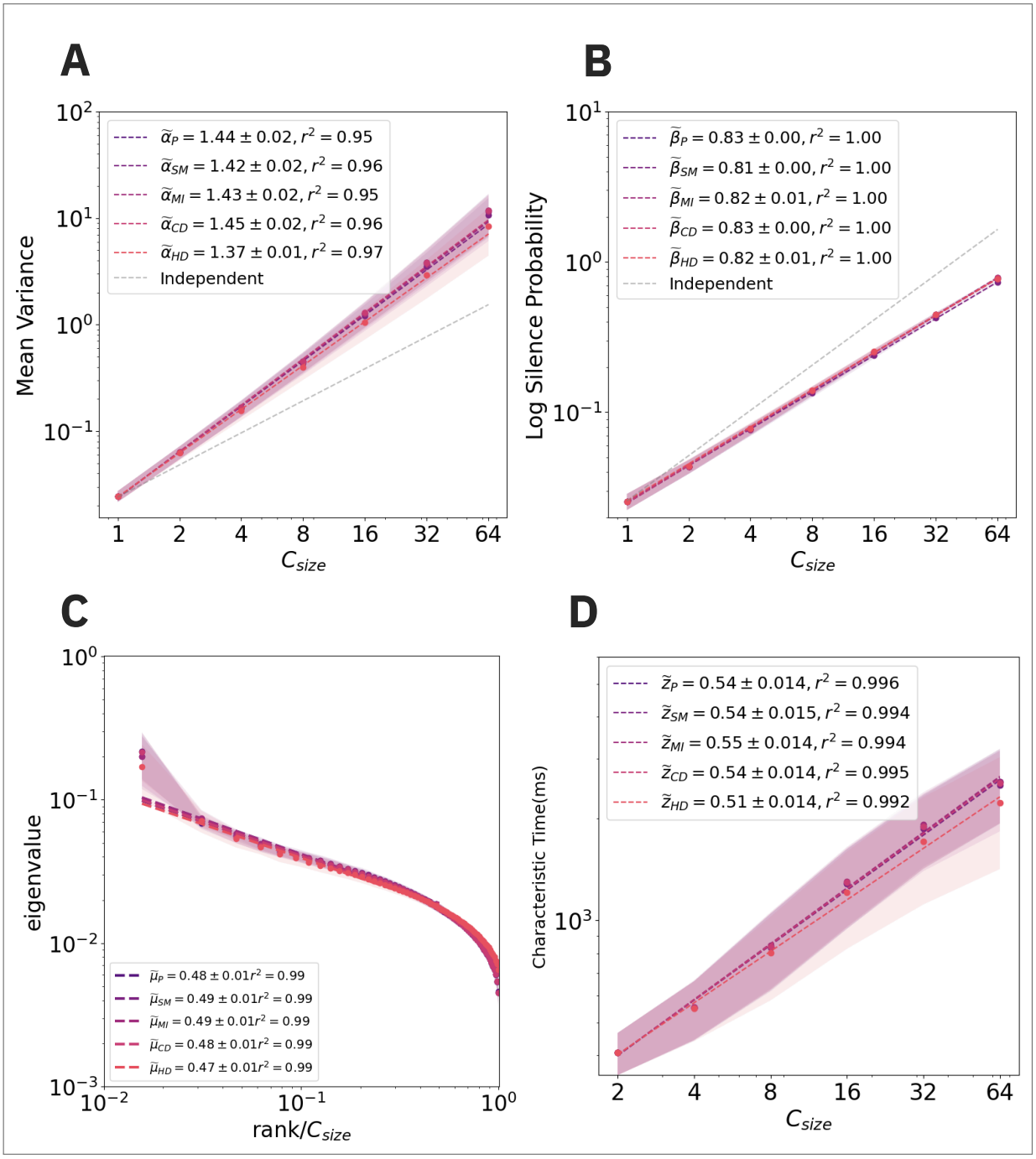

Source: The author.

Figure 43 – Wasserstein distances W_1 between successive activity distributions from the PRG method. (A) Comparison between distribution changes for different similarity metrics (Sec. 2.1.3). The distance across iterations seems to be monotonically decreasing for the momentum-space picture (inset). (B) Comparison of W_1 distances between spiking rat and human fMRI data, both from the momentum space distributions.

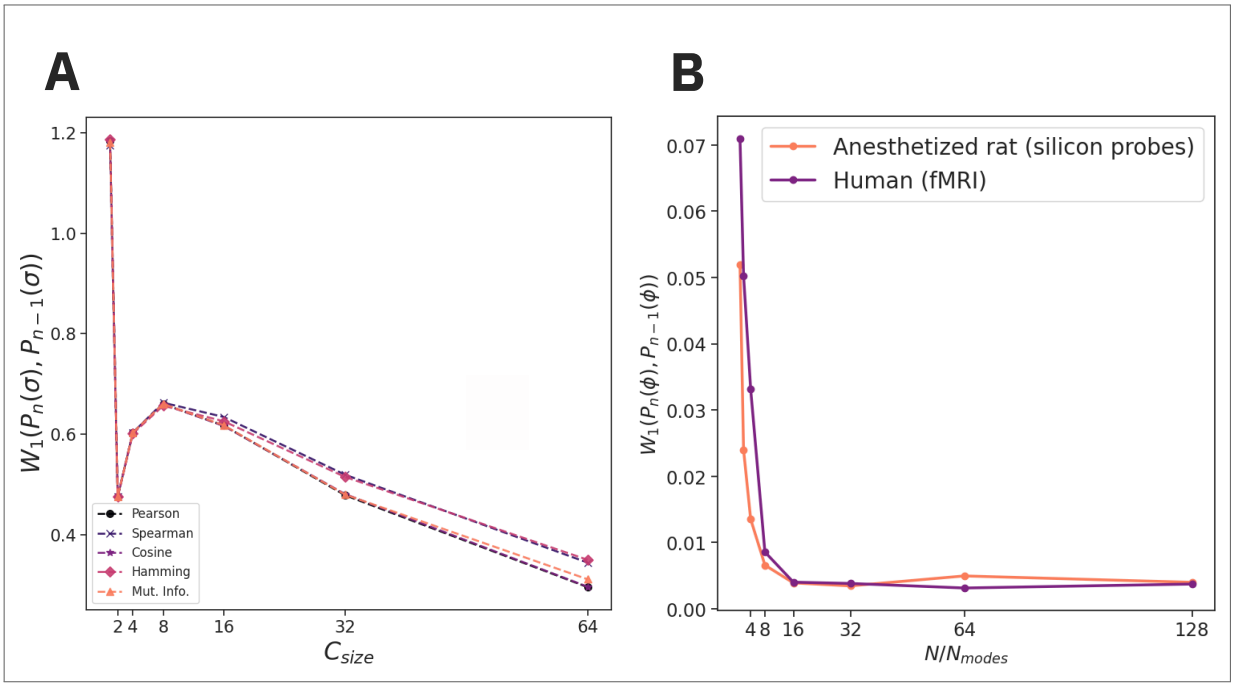

Source: The author.

would be indicated by $W_1(P_n(\sigma), P_{n-k}(\sigma)) \to const. \sim 0$) (Fig. 43A). In momentum space, however, the difference between distributions quickly drop within the first 5 rounds of coarse-graining. Something similar also happens if we look again at the anesthetized rats data from Chap. 3 (Fig. 43B).

In conclusion, we find that measuring the distance between distributions gives clues of how many iterations it takes to find a distribution that does not change under PRG transformations, albeit the dataset size does not permit us to give a definitive answer. Perhaps further investigation — possibly in models, where we have more control over the number of variables and parameters — can give a definitive answer on whether this (or some other) method is a valid way to assess the convergence of the PRG to a fixed point.

5 CLOSING REMARKS

By reaching the ending pages, we hope to have given a first introduction to the field of criticality in the brain, and how it has evolved from its inception to its current state. To translate ideas from statistical mechanics and dynamical systems to neuronal systems and the brain is a very exciting challenge, as it opens the possibility of understanding, from physical principles, how living beings perceive the world around them. Even though a theory of brain dynamics is barely in its infancy, research fields dedicated to it are timely and flourishing.

At the same time, there are many open questions on how to adapt or develop theoretical and experimental techniques that can overcome current observational issues. How to ride out subsampling problems, set correct event thresholds or bin lengths (or leapfrog them altogether) and other data-related technicalities are among them. For the sake of brevity, we opted to not list every single method existent in the criticality literature, leaving out, for example, maximum entropy models (SCHNEIDMAN et al., 2006) and detrended fluctuation analysis (DFA) (LINKENKAER-HANSEN et al., 2001). Each method — including the PRG — has their own strengths and will be better suited to answer different questions; still, we are only crawling towards a conclusive description of the putative phase transition governing brain dynamics.

One of the main targets of this work was to investigate the connection between criticality and more biological aspects of the system. Both result chapters try to achieve this with different approaches: Chap. 3, for instance, addresses how the temporal structure of cortical dynamics, a feature generally not encompassed in phase transition theory, may impact criticality and scale invariance. Our results show that anesthetized rats spiking data seem to fluctuate in and out of a critical regime, presenting scale invariance every time its spiking variability is above a characteristic threshold (CASTRO et al., 2024). Additionally, the so-called asynchronous states, as inferred by the CV, may not mean the same thing for awake and anesthetized animals, since they do not show the same signatures for the PRG method. To better understand *when* scale invariance presents itself in cortical dynamics is relevant because it may give us insights on its specific role at a given situation.

In Chap. 4, We explore the diversity of scaling exponents measured in fMRI data from human individuals, to obtain two distinct findings: first, different PRG exponents follow linear relationships between them. Finding how critical exponents relate from one another is an important step towards a deeper grasp of the PRG, as it happened historically with the RG

before the coming of Wilson's description (notice, though, that those systems had a fixed set of critical exponents, so this is not an exact comparison).

Finally, we show some preliminary results regarding the connection between scaling exponents and clinical aspects of the experiment participants. While not a comprehensive analysis in its current state, this research represents (to the best of our knowledge) the study with the largest sample size to date that correlates clinics and brain criticality (ZIMMERN, 2020).

With the PRG method itself being a recent development, there are many avenues are open for extending the results seen here. To list a few, we can:

- Determine if PRG exponents yield similar results for systems within the same universality class, to understand how universality transposes into the phenomenological scheme;
- Inspect the intermittency of scale invariance seen in Chap. 3 for awake animals and its relationship with task execution;
- Derive formal expressions for the empirical relations obtained in Chap. 4; and
- Explore the interplay between PRG and the main putative phase transitions for the brain in the literature, namely avalanche (type 1) criticality, edge-of-chaos (type 2) and asynchronous-to-synchronous transition (POIL et al., 2012; FONTENELE et al., 2019).

As we bring this thesis to a close, we hope its contents contribute to the body of knowledge in brain criticality and serves as a stepping stone for future discoveries.

REFERENCES

BASTOS, A. M.; VEZOLI, J.; BOSMAN, C. A.; SCHOFFELEN, J.; OOSTENVELD, R.; DOWDALL, J. R.; WEERD, P. D.; KENNEDY, H.; FRIES, P. Visual areas exert feedforward and feedback influences through distinct frequency channels. *Neuron*, v. 85, p. 390–401, 2015.

BEGGS, J. M. The criticality hypothesis: how local cortical networks might optimize information processing. *Philos. Trans. Royal Soc. A*, v. 366, p. 329–343, 2007.

BEGGS, J. M.; PLENZ, D. Neuronal avalanches in neocortical circuits. *J. Neurosci.*, v. 23, p. 11167–11177, 2003.

BEGGS, J. M.; PLENZ, D. Neuronal avalanches are diverse and precise activity patterns that are stable for many hours in cortical slice cultures. *J. Neurosci.*, v. 24, p. 5216–5229, 2004.

BELLAY, T.; KLAUS, A.; SESHADRI, S.; PLENZ, D. Irregular spiking of pyramidal neurons organizes as scale-invariant neuronal avalanches in the awake state. *Elife*, v. 4, p. e07224, 2015.

BONACHELA, J. A.; FRANCISCIS, S. de; TORRES, J. J.; NOZ, M. A. M. Self-organization without conservation: are neuronal avalanches generically critical? *J. Stat. Mech.*, v. 2010, p. P02015, 2010.

BONACHELA, J. A.; NOZ, M. A. M. Self-organization without conservation: true or just apparent scale-invariance? *J. Stat. Mech.*, v. 2009, p. P09009, 2009.

BRADDE, S.; BIALEK, W. Pca meets rg. *J. Stat. Phys.*, v. 167, p. 462–475, 2017.

BUZSAKI, G. Y.; BICKFORD, R. G.; PONOMAREFF, G.; THAL, L. J.; MANDEL, R.; GAGE, F. H. Nucleus basalis and thalamic control of neocortical activity in the freely moving rat. *J. Neurosci.*, v. 8, p. 4007–4026, 1988.

CAMPOS, J. G. F.; COSTA, A. de A.; COPELLI, M.; KINOUCHI, O. Correlations induced by depressing synapses in critically self-organized networks with quenched dynamics. *Phys. Rev. E*, v. 95, p. 042303, 2017.

CANDIA, A. de; SARRACINO, A.; APICELLA, I.; ARCANGELIS, L. de. Critical behaviour of the stochastic Wilson-Cowan model. *PLoS Comput. Biol.*, v. 17, p. 1–23, 2021.

CAPEK, E.; RIBEIRO, T. L.; KELLS, P.; SRINIVASAN, K.; MILLER, S. R.; GEIST, E.; VICTOR, M.; VAKILI, A.; PAJEVIC, S.; CHIALVO, D. R. et al. Parabolic avalanche scaling in the synchronization of cortical cell assemblies. *Nat. Commun.*, v. 14, p. 2555, 2023.

CARVALHO, T. T. A.; FONTENELE, A. J.; GIRARDI-SCHAPPO, M.; FELICIANO, T.; AGUIAR, L. A. A.; SILVA, T. P. L.; VASCONCELOS, N. A. P. de; CARELLI, P. V.; COPELLI, M. Subsampled directed-percolation models explain scaling relations experimentally observed in the brain. *Front. Neural Circuits*, v. 14, p. 83, 2021.

CASSANDRO, M.; JONA-LASINIO, G. Critical point behaviour and probability theory. *Adv. Phys.*, v. 27, p. 913–941, 1978.

CASTRO, D. M.; FELICIANO, T.; VASCONCELOS, N. A. P. de; SOARES-CUNHA, C.; COIMBRA, B.; RODRIGUES, A. J.; CARELLI, P. V.; COPELLI, M. In and out of criticality? state-dependent scaling in the rat visual cortex. *PRX Life*, v. 2, p. 023008, 2024.

CHEN, G.; SCHERR, F.; MAASS, W. A data-based large-scale model for primary visual cortex enables brain-like robust and versatile visual processing. *Sci. Adv.*, v. 8, p. eabq7592, 2022.

CLEMENT, E. A.; RICHARD, A.; THWAITES, M.; AILON, J.; PETERS, S.; DICKSON, C. T. Cyclic and sleep-like spontaneous alternations of brain state under urethane anaesthesia. *PloS One*, v. 3, p. e2004, 2008.

COSTA, A. A.; BROCHINI, L.; KINOUCHI, O. Self-organized supercriticality and oscillations in networks of stochastic spiking neurons. *Entropy*, v. 19, p. 399, 2017.

COSTA, A. de A.; COPELLI, M.; KINOUCHI, O. Can dynamical synapses produce true self-organized criticality? *J. Stat. Mech. Theory Exp.*, v. 2015, p. P06004, 2015.

DAHMEN, D.; GRÜN, S.; DIESMANN, M.; HELIAS, M. Second type of criticality in the brain uncovers rich multiple-neuron dynamics. *Proc. Natl. Acad. Sci. U.S.A.*, v. 116, p. 13051–13060, 2019.

DALLA PORTA, L.; MATIAS, F. S.; SANTOS, A. J. dos; ALONSO, A.; CARELLI, P. V.; COPELLI, M.; MIRASSO, C. R. Exploring the phase-locking mechanisms yielding delayed and anticipated synchronization in neuronal circuits. *Front. Sys. Neurosci.*, v. 13, p. 41, 2019.

DE ARCANGELIS, L.; PERRONE-CAPANO, C.; HERRMANN, H. J. Self-organized criticality model for brain plasticity. *Phys. Rev. Lett.*, v. 96, p. 028107, 2006.

DEFELIPE, J. The evolution of the brain, the human nature of cortical circuits, and intellectual creativity. *Front. Neuroanat.*, v. 5, p. 29, 2011.

DESTEXHE, A.; TOUBOUL, J. D. Is there sufficient evidence for criticality in cortical systems? *Eneuro*, v. 8, 2021.

DOMB, C. *The critical point: a historical introduction to the modern theory of critical phenomena*. London: CRC Press, 1996.

EGUÍLUZ, V. M.; CHIALVO, D. R.; CECCHI, G. A.; BALIKI, M.; APKARIAN, A. V. Scale-free functional brain networks. *Phys. Rev. Lett.*, v. 94, p. 018102, 2005.

ELAM, J. S.; GLASSER, M. F.; HARMS, M. P.; SOTIROPOULOS, S. N.; ANDERSSON, J. L. R.; BURGESS, G. C.; CURTISS, S. W.; OOSTENVELD, R.; LARSON-PRIOR, L. J.; SCHOFFELEN, J. et al. The human connectome project: a retrospective. *NeuroImage*, v. 244, p. 118543, 2021.

ERICKSON, K. I.; RAJI, C. A.; LOPEZ, O. L.; BECKER, J. T.; ROSANO, C.; NEWMAN, A. B.; GACH, H. M.; THOMPSON, P. M.; HO, A. J.; KULLER, L. H. Physical activity predicts gray matter volume in late adulthood: the cardiovascular health study. *Neurology*, v. 75, p. 1415–1422, 2010.

ESCRICHS, A.; PERL, Y. S.; URIBE, C.; CAMARA, E.; TÜRKER, B.; PYATIGORSKAYA, N.; LÓPEZ-GONZÁLEZ, A.; PALLAVICINI, C.; PANDA, R.; ANNEN, J. o. Unifying turbulent dynamics framework distinguishes different brain states. *Commun. Biol.*, v. 5, p. 638, 2022.

FONTENELE, A. J.; SOOTER, J. S.; K., N. V.; GAUTAM, S. H.; SHEW, W. L. Low-dimensional criticality embedded in high-dimensional awake brain dynamics. *Sci. Adv.*, v. 10, p. eadj9303, 2024.

FONTENELE, A. J.; VASCONCELOS, N. A. P. de; FELICIANO, T.; AGUIAR, L. A. A.; SOARES-CUNHA, C.; COIMBRA, B.; PORTA, L. D.; RIBEIRO, S.; RODRIGUES, A. J.; SOUSA, N.; CARELLI, P.; COPELLI, M. Criticality between cortical states. *Phys. Rev. Lett.*, v. 122, p. 208101, 2019.

FOSQUE, L. J.; WILLIAMS-GARCÍA, R. V.; BEGGS, J. M.; ORTIZ, G. Evidence for quasicritical brain dynamics. *Phys. Rev. Lett.*, v. 126, p. 098101, 2021.

FRAIMAN, D.; BALENZUELA, P.; FOSS, J.; CHIALVO, D. R. Ising-like dynamics in large-scale functional brain networks. *Phys. Rev. E*, American Physical Society, v. 79, p. 061922, 2009.

FRIEDMAN, N.; ITO, S.; BRINKMAN, B. A.; SHIMONO, M.; DEVILLE, R. L.; DAHMEN, K. A.; BEGGS, J. M.; BUTLER, T. C. Universal critical dynamics in high resolution neuronal avalanche data. *Phys. Rev. Lett.*, v. 108, p. 208102, 2012.

FÜLÖP, T.; DESROCHES, M.; COHEN, A. A.; SANTOS, F. A. N.; RODRIGUES, S. Why we should use topological data analysis in ageing: towards defining the "topological shape of ageing". *Mech. Ageing Dev.*, v. 192, p. 111390, 2020.

GAUTAM, S. H.; HOANG, T. T.; MCCLANAHAN, K.; GRADY, S. K.; SHEW, W. L. Maximizing sensory dynamic range by tuning the cortical state to criticality. *PLoS Comput. Biol.*, v. 11, p. e1004576, 2015.

GERSTNER, W. Integrate-and-fire neurons and networks. *The handbook of brain theory and neural networks*, v. 2, p. 577–581, 2002.

GIRARDI-SCHAPPO, M.; BROCHINI, L.; COSTA, A.; CARVALHO, T.; KINOUCHI, O. Synaptic balance due to homeostatically self-organized quasicritical dynamics. *Phys. Rev. Res.*, v. 2, p. 012042, 2020.

GREENFIELD, E.; LECAR, H. Mutual information in a dilute, asymmetric neural network model. *Phys. Rev. E*, v. 63, p. 041905, 2001.

GROSS, C. G. Early history of neuroscience. *Encyclopedia of neuroscience*, Birkhäuser Boston, MA, v. 2, p. 843–846, 1987.

HALDEMAN, C.; BEGGS, J. M. Critical branching captures activity in living neural networks and maximizes the number of metastable states. *Phys. Rev. Lett.*, v. 94, p. 058101, 2005.

HAMPEL, H.; TOSCHI, N.; BABILONI, C.; BALDACCI, F.; BLACK, K. L.; BOKDE, A. L. W.; BUN, R. S.; CACCIOLA, F.; CAVEDO, E.; CHIESA, P. A. et al. Revolution of alzheimer precision neurology. passageway of systems biology and neurophysiology. *J. Alzheimer's Dis.*, v. 64, p. S47–S105, 2018.

HARMS, M. P.; SOMERVILLE, L. H.; ANCES, B. M.; ANDERSSON, J.; BARCH, D. M.; BASTIANI, M.; BOOKHEIMER, S. Y.; BROWN, T. B.; BUCKNER, R. L.; BURGESS, G. C. et al. Extending the human connectome project across ages: Imaging protocols for the lifespan development and aging projects. *Neuroimage*, v. 183, p. 972–984, 2018.

HARRIS, K. D.; THIELE, A. Cortical state and attention. *Nat. Rev. Neurosci.*, v. 12, n. 9, p. 509, 2011.

HELIAS, M.; DAHMEN, D. *Statistical field theory for neural networks*. New York: Springer, 2020. v. 970.

HERCULANO-HOUZEL, S.; MOTA, B.; LENT, R. Cellular scaling rules for rodent brains. *Proc. Natl. Acad. Sci. U.S.A.*, v. 103, p. 12138–12143, 2006.

HILGETAG, C. C.; GOULAS, A. Is the brain really a small-world network? *Brain. Struct. Funct.*, v. 221, p. 2361–2366, 2016.

HILLMAN, E. M. C. Coupling mechanism and significance of the bold signal: a status report. *Annu. Rev. Neurosci.*, v. 37, p. 161–181, 2014.

HINDRIKS, R.; BROEDERS, T. A. A.; SCHOONHEIM, M. M.; DOUW, L.; SANTOS, F.; WIERINGEN, W. van; TEWARIE, P. K. Higher-order functional connectivity analysis of resting-state functional magnetic resonance imaging data using multivariate cumulants. *Hum. Brain Mapp.*, v. 45, p. e26663, 2024.

HOLT, G. R.; SOFTKY, W. R.; KOCH, C.; DOUGLAS, R. J. Comparison of discharge variability in vitro and in vivo in cat visual cortex neurons. *J. Neurophysiol.*, v. 75, p. 1806–1814, 1996.

JONA-LASINIO, G. The renormalization group: A probabilistic view. *Nuovo Cim. B*, v. 352, p. 99–119, 1975.

JONA-LASINIO, G. Renormalization group and probability theory. *Phys. Rep.*, v. 352, p. 439–458, 2001.

JUN, J. J.; STEINMETZ, N. A.; SIEGLE, J. H.; DENMAN, D. J.; BAUZA, M.; BARBARITS, B.; LEE, A. K.; ANASTASSIOU, C. A.; ANDREI, A.; AYDIN, c. et al. Fully integrated silicon probes for high-density recording of neural activity. *Nature*, v. 551, p. 232–236, 2017.

KAAS, J. H.; COLLINS, C. E. The organization of sensory cortex. *Curr. Opin. Neurobiol.*, Elsevier, v. 11, n. 4, p. 498–504, 2001.

KADANOFF, L. P. More is the same; phase transitions and mean field theories. *J. Stat. Phys.*, Springer, v. 137, p. 777–797, 2009.

KANDEL, E. R.; SCHWARTZ, J. H.; JESSELL, T. M.; SIEGELBAUM, S.; HUDSPETH, A. J.; MACK, S. et al. *Principles of neural science*. New York: McGraw-hill New York, 2000. v. 4.

KINOUCHI, O.; BROCHINI, L.; COSTA, A. A.; CAMPOS, J. G. F.; COPELLI, M. Stochastic oscillations and dragon king avalanches in self-organized quasi-critical systems. *Sci. Rep.*, v. 9, p. 3874, 2019.

KINOUCHI, O.; COPELLI, M. Optimal dynamical range of excitable networks at criticality. *Nat. Phys.*, v. 2, p. 348–351, 2006.

KINOUCHI, O.; PAZZINI, R.; COPELLI, M. Mechanisms of self-organized quasicriticality in neuronal network models. *Front. Phys.*, v. 8, p. 530, 2020.

KINOUCHI, O.; PRADO, C. P. Robustness of scale invariance in models with self-organized criticality. *Phys. Rev. E*, v. 59, p. 4964, 1999.

KOCH, C. *Biophysics of computation: information processing in single neurons*. Oxford: Oxford University Press, 2004.

KOHN, A.; SMITH, M. A. Utah array extracellular recordings of spontaneous and visually evoked activity from anesthetized macaque primary visual cortex (v1). *CRCNS. org*, v. 10, p. K0NC5Z4X, 2016.

KOLOURI, S. Optimal transport and wasserstein distance. Lecture Notes. n.d.

LARREMORE, D.; SHEW, W.; RESTREPO, J. Predicting Criticality and Dynamic Range in Complex Networks: Effects of Topology. *Phys. Rev. Lett.*, v. 106, p. 058101, 2011.

LATHAM, P. E.; ROUDI, Y. Mutual information. *Scholarpedia*, v. 4, p. 1658, 2009.

LEE, S.; DAN, Y. Neuromodulation of brain states. *Neuron*, v. 76, p. 209–222, 2012.

LEVINA, A.; HERRMANN, J. M.; GEISEL, T. Dynamical synapses causing self-organized criticality in neural networks. *Nat. Phys.*, v. 3, p. 857–860, 2007.

LEVINA, A.; HERRMANN, J. M.; GEISEL, T. Phase transitions towards criticality in a neural system with adaptive interactions. *Phys. Rev. Lett.*, v. 102, p. 118110, 2009.

LINKENKAER-HANSEN, K.; NIKOULINE, V. V.; PALVA, J. M.; ILMONIEMI, R. J. Long-range temporal correlations and scaling behavior in human brain oscillations. *J. Neurosci.*, v. 21, p. 1370–1377, 2001.

LITWIN-KUMAR, A.; DOIRON, B. Slow dynamics and high variability in balanced cortical networks with clustered connections. *Nat. Neurosci.*, v. 15, p. 1498–1505, 2012.

LOMBARDI, F.; HERRMANN, H. J.; PERRONE-CAPANO, C.; PLENZ, D.; ARCANGELIS, L. de. Balance between excitation and inhibition controls the temporal organization of neuronal avalanches. *Phys. Rev. Lett.*, v. 108, p. 228703, 2012.

LOTFI, N.; FELICIANO, T.; AGUIAR, L. A. A.; SILVA, T. P. L.; CARVALHO, T. T. A.; ROSSO, O. A.; COPELLI, M.; MATIAS, F. S.; CARELLI, P. V. Statistical complexity is maximized close to criticality in cortical dynamics. *Phys. Rev. E*, v. 103, p. 012415, 2021.

LOTFI, N.; FONTENELE, A. J.; FELICIANO, T.; AGUIAR, L. A. A.; VASCONCELOS, N. A. P. de; SOARES-CUNHA, C.; COIMBRA, B.; RODRIGUES, A. J.; SOUSA, N.; COPELLI, M.; CARELLI, P. V. Signatures of brain criticality unveiled by maximum entropy analysis across cortical states. *Phys. Rev. E*, v. 102, p. 012408, 2020.

MARRO, J.; DICKMAN, R. *Nonequilibrium Phase Transition in Lattice Models*. Cambridge: Cambridge University Press, 1999.

MCCOMB, W. D. *Renormalization methods: a guide for beginners*. Oxford: OUP Oxford, 2003.

MESHULAM, L.; GAUTHIER, J. L.; BRODY, C. D.; TANK, D. W.; BIALEK, W. Coarse–graining and hints of scaling in a population of 1000+ neurons. *ArXiv. org*, 2018.

MESHULAM, L.; GAUTHIER, J. L.; BRODY, C. D.; TANK, D. W.; BIALEK, W. Coarse graining, fixed points, and scaling in a large population of neurons. *Phys. Rev. Lett.*, v. 123, p. 178103, 2019.

MILLER, S. R.; YU, S.; PLENZ, D. The scale-invariant, temporal profile of neuronal avalanches in relation to cortical γ–oscillations. *Sci. Rep.*, v. 9, p. 16403, 2019.

MORALES, G.; SANTO, S. D.; MUÑOZ, M. Quasiuniversal scaling in mouse-brain neuronal activity stems from edge-of-instability critical dynamics. *Proc. Natl. Acad. Sci.*, v. 120, p. e2208998120, 2023.

MORETTI, P.; MUÑOZ, M. A. Griffiths phases and the stretching of criticality in brain networks. *Nat. Commun.*, v. 4, p. 2521, 2013.

MORRELL, M. C.; SEDERBERG, A.; NEMENMAN, I. Latent dynamical variables produce signatures of spatiotemporal criticality in large biological systems. *Phys. Rev. Let.*, v. 126, p. 118302, 2021.

MOTA, B.; HERCULANO-HOUZEL, S. Cortical folding scales universally with surface area and thickness, not number of neurons. *Science*, v. 349, p. 74–77, 2015.

NANDI, M. K.; SARRACINO, A.; HERRMANN, H. J.; ARCANGELIS, L. de. Scaling of avalanche shape and activity power spectrum in neuronal networks. *Phys. Rev. E*, v. 106, p. 024304, 2022.

NAWROT, M. P.; BOUCSEIN, C.; MOLINA, V. R.; RIEHLE, A.; AERTSEN, A.; ROTTER, S. Measurement of variability dynamics in cortical spike trains. *J. Neurosci. Methods*, v. 169, p. 374–390, 2008.

NICOLETTI, G.; SUWEIS, S.; MARITAN, A. Scaling and criticality in a phenomenological renormalization group. *Phys. Rev. Res.*, v. 2, p. 023144, 2020.

O'BYRNE, J.; JERBI, K. How critical is brain criticality? *Trends Neurosci.*, v. 45, p. 820–837, 2022.

PALVA, J. M.; ZHIGALOV, A.; HIRVONEN, J.; KORHONEN, O.; LINKENKAER-HANSEN, K.; PALVA, S. Neuronal long-range temporal correlations and avalanche dynamics are correlated with behavioral scaling laws. *Proc. Natl. Acad. Sci.*, v. 110, p. 3585–3590, 2013.

PANARETOS, V. M.; ZEMEL, Y. Statistical aspects of wasserstein distances. *Annu. Rev. Stat. Appl.*, v. 6, p. 405–431, 2019.

PASQUALE, V.; MASSOBRIO, P.; BOLOGNA, L. L.; CHIAPPALONE, M.; MARTINOIA, S. Self-organization and neuronal avalanches in networks of dissociated cortical neurons. *Neurosci.*, v. 153, p. 1354–1369, 2008.

PÁSZTO, V.; MAREK, L.; TUCEK, P. Fractal dimension calculation for corine land-cover evaluation in gis - a case study. *CEUR Workshop Proc.*, v. 706, p. 196–205, 2011.

PAXINOS, G.; ASHWELL, K. *Atlas of the developing rat nervous system*. New York: Academic Press, 2018.

PEDROSA, V.; CLOPATH, C. The role of neuromodulators in cortical plasticity. a computational perspective. *Front. Synaptic Neurosci.*, v. 8, p. 38, 2017.

PETERMANN, T.; THIAGARAJAN, T. C.; LEBEDEV, M. A.; NICOLELIS, M. A. L.; CHIALVO, D. R.; PLENZ, D. Spontaneous cortical activity in awake monkeys composed of neuronal avalanches. *Proc. Natl. Acad. Sci. USA*, v. 106, p. 15921–15926, 2009.

PETERMANN, T.; THIAGARAJAN, T. C.; LEBEDEV, M. A.; NICOLELIS, M. A.; CHIALVO, D. R.; PLENZ, D. Spontaneous cortical activity in awake monkeys composed of neuronal avalanches. *Proc. Natl. Acad. Sci.*, National Acad Sciences, v. 106, n. 37, p. 15921–15926, 2009.

PIUVEZAM, H. C.; MARIN, B.; COPELLI, M.; MUÑOZ, M. A. Unconventional criticality, scaling breakdown, and diverse universality classes in the wilson-cowan model of neural dynamics. *Phys. Rev. E*, American Physical Society, v. 108, p. 034110, Sep 2023.

PLENZ, D.; NIEBUR, E. (Ed.). *Criticality in Neural Systems*. Weinheim: Wiley, 2014.

PLENZ, D.; THIAGARAJAN, T. C. The organizing principles of neuronal avalanches: Cell assemblies in the cortex? *Trends Neurosci.*, v. 30, p. 101–110, 2007.

POIL, S.-S.; HARDSTONE, R.; MANSVELDER, H. D.; LINKENKAER-HANSEN, K. Critical-state dynamics of avalanches and oscillations jointly emerge from balanced excitation/inhibition in neuronal networks. *J. Neurosci.*, v. 32, p. 9817–23, 2012.

PONCE-ALVAREZ, A.; KRINGELBACH, M. L.; DECO, G. Critical scaling of whole-brain resting-state dynamics. *Commun. Biol.*, v. 6, p. 627, 2023.

PRIESEMANN, V.; MUNK, M. H. J.; WIBRAL, M. Subsampling effects in neuronal avalanche distributions recorded *in vivo*. *BMC Neurosci.*, v. 10, p. 40, 2009.

PRIESEMANN, V.; WIBRAL, M.; VALDERRAMA, M.; PRöPPER, R.; QUYEN, M. L. V.; GEISEL, T.; TRIESCH, J.; NIKOLIć, D.; MUNK, M. H. J. Spike avalanches in vivo suggest a driven, slightly subcritical brain state. *Front. Sys. Neurosci.*, v. 8, p. 108, 2014.

REICHL, L. E. *A modern course in statistical physics*. New Jersey: John Wiley & Sons, 1998.

RENART, A.; ROCHA, J. de la; BARTHO, P.; HOLLENDER, L.; PARGA, N.; REYES, A.; HARRIS, K. D. The asynchronous state in cortical circuits. *Science*, v. 327, p. 587–590, 2010.

RIBEIRO, T. L.; COPELLI, M.; CAIXETA, F.; BELCHIOR, H.; CHIALVO, D. R.; NICOLELIS, M. A. L.; RIBEIRO, S. Spike avalanches exhibit universal dynamics across the sleep-wake cycle. *PLoS One*, v. 5, p. e14129, 2010.

RINGACH, D. L. Spontaneous and driven cortical activity: implications for computation. *Curr. Opin. Neurobiol.*, v. 19, p. 439–444, 2009.

SANTO, S. di; VILLEGAS, P.; BURIONI, R.; MUÑOZ, M. A. Landau–Ginzburg theory of cortex dynamics: Scale-free avalanches emerge at the edge of synchronization. *Proc. Natl. Acad. Sci. U.S.A.*, v. 115, p. E1356–E1365, 2018.

SCARPETTA, S.; APICELLA, I.; MINATI, L.; CANDIA, A. de. Hysteresis, neural avalanches, and critical behavior near a first-order transition of a spiking neural network. *Phys. Rev. E*, v. 97, p. 062305, 2018.

SCHAEFER, A.; KONG, R.; GORDON, E. M.; LAUMANN, T. O.; ZUO, X.; HOLMES, A. J.; EICKHOFF, S. B.; YEO, B. T. Local-global parcellation of the human cerebral cortex from intrinsic functional connectivity mri. *Cereb. Cortex*, v. 28, p. 3095–3114, 2018.

SCHIEL, J. E.; TAMM, S.; HOLUB, F.; PETRI, R.; DASHTI, H. S.; DOMSCHKE, K.; FEIGE, B.; GOODMAN, M. O.; JONES, S. E.; LANE, J. M. et al. Associations between sleep health and grey matter volume in the uk biobank cohort (n= 33 356). *Brain Commun.*, v. 5, p. fcad200, 2023.

SCHNEIDMAN, E.; BERRY, M. J.; SEGEV, R.; BIALEK, W. Weak pairwise correlations imply strongly correlated network states in a neural population. *Nature*, v. 440, p. 1007–1012, 2006.

SCHÖLVINCK, M. L.; SALEEM, A. B.; BENUCCI, A.; HARRIS, K. D.; CARANDINI, M. Cortical state determines global variability and correlations in visual cortex. *J. Neurosci.*, v. 35, p. 170–178, 2015.

SCHREIBER, T.; SCHMITZ, A. Surrogate time series. *Physica D.*, v. 142, p. 346–382, 2000.

SCOTT, G.; FAGERHOLM, E. D.; MUTOH, H.; LEECH, R.; SHARP, D. J.; SHEW, W. L.; KNÖPFEL, T. Voltage imaging of waking mouse cortex reveals emergence of critical neuronal dynamics. *J. Neurosci.*, v. 34, p. 16611–16620, 2014.

SEJNOWSKI, T. J.; CHURCHLAND, P. S.; MOVSHON, J. A. Putting big data to good use in neuroscience. *Nat. Neurosci.*, v. 17, p. 1440–1441, 2014.

SENZAI, Y.; FERNANDEZ-RUIZ, A.; BUZSÁKI, G. Layer-specific physiological features and interlaminar interactions in the primary visual cortex of the mouse. *Neuron*, v. 101, p. 500–513, 2019.

SETHNA, J. P.; DAHMEN, K. A.; MYERS, C. R. Crackling noise. *Nature*, v. 410, p. 242–250, 2001.

SHEW, W.; PLENZ, D. The functional benefits of criticality in the cortex. *Neuroscientist*, v. 19, p. 88–100, 2013.

SHEW, W.; YANG, H.; PETERMANN, T.; ROY, R.; PLENZ, D. Neuronal avalanches imply maximum dynamic range in cortical networks at criticality. *J. Neurosci.*, v. 29, p. 15595–15600, 2009.

SHEW, W. L.; CLAWSON, W. P.; POBST, J.; KARIMIPANAH, Y.; WRIGHT, N. C.; WESSEL, R. Adaptation to sensory input tunes visual cortex to criticality. *Nat. Phys.*, v. 11, p. 659–663, 2015.

SHEW, W. L.; YANG, H.; YU, S.; ROY, R.; PLENZ, D. Information capacity and transmission are maximized in balanced cortical networks with neuronal avalanches. *J. Neurosci.*, v. 31, p. 55–63, 2011.

SHRIKI, O.; ALSTOTT, J.; CARVER, F.; HOLROYD, T.; HENSON, R. N.; SMITH, M. L.; COPPOLA, R.; BULLMORE, E.; PLENZ, D. Neuronal avalanches in the resting MEG of the human brain. *J. Neurosci.*, v. 33, p. 7079–7090, 2013.

SKINNER, F. K. Conductance-based models. *Scholarpedia*, v. 1, p. 1408, 2006.

SOFTKY, W. R.; KOCH, C. The highly irregular firing of cortical cells is inconsistent with temporal integration of random epsps. *J. Neurosci.*, v. 13, p. 334–350, 1993.

SRINIVASAN, K.; RIBEIRO, T. L.; KELLS, P.; PLENZ, D. The recovery of parabolic avalanches in spatially subsampled neuronal networks at criticality. *bioRxiv*, p. 2024–02, 2024.

STEWART, C. V.; PLENZ, D. Inverted-U profile of dopamine-NMDA-mediated spontaneous avalanche recurrence in superficial layers of rat prefrontal cortex. *J. Neurosci.*, v. 26, p. 8148–59, 2006.

TAGLIAZUCCHI, E.; BALENZUELA, P.; FRAIMAN, D.; CHIALVO, D. R. Criticality in large-scale brain fMRI dynamics unveiled by a novel point process analysis. *Front. Physiol.*, v. 3, p. 15, 2012.

TALLINEN, T.; CHUNG, J. Y.; ROUSSEAU, F.; GIRARD, N.; LEFÈVRE, J.; MAHADEVAN, L. On the growth and form of cortical convolutions. *Nat. Phys.*, v. 12, p. 588–593, 2016.

TIJHUIS, F. B.; BROEDERS, T. A. A.; SANTOS, F. A. N.; SCHOONHEIM, M. M.; KILLESTEIN, J.; LEURS, C. E.; GEEST, Q. van; STEENWIJK, M. D.; GEURTS, J. J. G.; HULST, H. E. et al. Dynamic functional connectivity as a neural correlate of fatigue in multiple sclerosis. *NeuroImage Clin.*, v. 29, p. 102556, 2021.

TOMEN, N.; HERRMANN, M. J.; ERNST, U. *The Functional Role of Critical Dynamics in Neural Systems*. Cham, Switzerland: Springer, 2019.

TONG, D. Statistical field theory. *Lecture Notes*, 2017.

TOUBOUL, J.; DESTEXHE, A. Can power-law scaling and neuronal avalanches arise from stochastic dynamics? *PloS one*, v. 5, p. e8982, 2010.

TOUBOUL, J.; DESTEXHE, A. Power-law statistics and universal scaling in the absence of criticality. *Phys. Rev. E*, v. 95, p. 012413, 2017.

TSODYKS, M.; KENET, T.; GRINVALD, A.; ARIELI, A. Linking spontaneous activity of single cortical neurons and the underlying functional architecture. *Science*, v. 286, p. 1943–1946, 1999.

VASCONCELOS, N. A. P. de; SOARES-CUNHA, C.; RODRIGUES, A. J.; RIBEIRO, S.; SOUSA, N. Coupled variability in primary sensory areas and the hippocampus during spontaneous activity. *Sci. Rep.*, v. 7, p. 46077, 2017.

VENTURA-ANTUNES, L.; MOTA, B.; HERCULANO-HOUZEL, S. Different scaling of white matter volume, cortical connectivity, and gyrification across rodent and primate brains. *Front. neuroanat.*, v. 7, p. 3, 2013.

VILLANI, C. *Topics in optimal transportation*. Providence: American Mathematical Soc., 2021. v. 58.

WANG, X. Neurophysiological and computational principles of cortical rhythms in cognition. *Physiol. Rev.*, v. 90, p. 1195–1268, 2010.

WILSON, K. G. The renormalization group: Critical phenomena and the kondo problem. *RMP*, v. 47, p. 773, 1975.

XU, L.; FENG, J.; YU, L. Avalanche criticality in individuals, fluid intelligence, and working memory. *Human brain mapping*, v. 43, p. 2534–2553, 2022.

YANG, H.; SHEW, W. L.; ROY, R.; PLENZ, D. Maximal variability of phase synchrony in cortical networks with neuronal avalanches. *J. Neurosci.*, v. 32, p. 1061–1072, 2012.

ZHIGALOV, A.; ARNULFO, G.; NOBILI, L.; PALVA, S.; PALVA, J. M. Relationship of fast-and slow-timescale neuronal dynamics in human MEG and SEEG. *J. Neurosci.*, v. 35, p. 5385–5396, 2015.

ZIMMERMANN, M. L. M.; BREEDT, L. C.; CENTENO, E. G. Z.; REIJNEVELD, J. C.; SANTOS, F. A. N.; STAM, C. J.; LINGEN, M. R. van; SCHOONHEIM, M. M.; HILLEBRAND, A.; DOUW, L. The relationship between pathological brain activity and functional network connectivity in glioma patients. *JNO*, p. 1–11, 2024.

ZIMMERN, V. Why brain criticality is clinically relevant: a scoping review. *Front. Neural Circuits*, v. 14, p. 565335, 2020.

APPENDIX A – TRANSLATIONAL INVARIANCE AND COVARIANCE MATRIX

In section 2.1.2, we argue that, for systems with translational invariance, diagonalizing the covariance matrix is equivalent to applying a Fourier transform on it. Here, we go through a brief demonstration, as previously done in (NICOLETTI; SUWEIS; MARITAN, 2020).

Starting with the covariance matrix

$$C_{ij} = \langle \sigma_i^{(1)} \sigma_j^{(1)} \rangle - \langle \sigma_i^{(1)} \rangle \langle \sigma_j^{(1)} \rangle \ , \tag{A.1}$$

possessing translational invariance means that $C_{ij} = C(\mathbf{x}_i - \mathbf{x}_j)$ for some function C. Then, its Fourier transform is

$$\begin{aligned} C(\mathbf{k}, \mathbf{q}) &= \frac{1}{N} \sum_{i,j} C(\mathbf{x}_i - \mathbf{x}_j) e^{-i\mathbf{x}_i \cdot \mathbf{k}} e^{-i\mathbf{x}_j \cdot \mathbf{q}} & \text{(A.2)} \\ &= \delta_{\mathbf{k},\text{-}\mathbf{q}} G(\mathbf{k}), & \text{(A.3)} \end{aligned}$$

where

$$G(\mathbf{k}) = \sum_n e^{-i\mathbf{x}_n \cdot \mathbf{k}} C(\mathbf{x}_n). \tag{A.4}$$

Therefore, we can write $C(\mathbf{x}_i - \mathbf{x}_j)$ as

$$C(\mathbf{x}_i - \mathbf{x}_j) = \frac{1}{N} \sum_{\mathbf{k}} e^{i\mathbf{k} \cdot (\mathbf{x}_i - \mathbf{x}_j)} G(\mathbf{k}), \tag{A.5}$$

showing that the covariance matrix is diagonal in Fourier space.

We can also demonstrate that the eigenvalues can be expressed as the Fourier transform of the correlation function G(k):

$$\begin{aligned} \sum_{\mathbf{x}_j} C(\mathbf{x}_i - \mathbf{x}_j) e^{i\mathbf{k} \cdot \mathbf{x}_j} &= e^{i\mathbf{k} \cdot \mathbf{x}_i} \sum_{\mathbf{x}_j} C(\mathbf{x}_i - \mathbf{x}_j) e^{-i(\mathbf{k} \cdot \mathbf{x}_i - \mathbf{k} \cdot \mathbf{x}_j)} & \text{(A.6)} \\ &= e^{i\mathbf{k} \cdot \mathbf{x}_i} G(\mathbf{k}), & \text{(A.7)} \end{aligned}$$

hence e^{ikx} is an eigenfunction of eigenvalue $G(\mathbf{k})$.

APPENDIX B – JOINT PROBABILITY OF CV AND SCALING BY ANIMAL

Here, we show de details of the state-dependent PRG analysis, as done in section 3.2, for each animal individually. For each 30-s window i, we compute the spiking variability CV_i of its population rate and the kurtosis κ_i of its MS activity distribution. Comparing κ_i with its surrogate counterpart, we apply the scaling criterion (Section 3.2) to determine whether there is scaling in this window (say, $S_i = 1$) or not ($S_i = 0$).

For a single animal, or for the whole group, we can therefore estimate the joint probability $P(x, s)$ and the corresponding marginals:

$$\mathbb{P}[\mathrm{CV} = x] = \sum_{s=0,1} P(x, s)\, dx \tag{B.1}$$

and

$$\mathbb{P}[S = s] = \int_0^\infty P(x, s)\, dx\ . \tag{B.2}$$

The marginal distribution of CV (i.e. regardless of scaling, as in Eq. B.1) is shown in Fig. 29F.

On the other hand, the distributions $P(x, 1)$ and $P(x, 0)$ are shown in Figs. 44-52 for each subject, and in Fig. 29G of the manuscript for the group data. In this case, the area of each distribution is simply the probability of finding scaling or not finding scaling in the whole time series, as in Eq. B.2.

Figure 44 – State dependent analysis for subject 1. (A) Kurtosis of the distribution of MS corse-grained variables (built from $N/64$ eigenmodes). Darker curve is the moving average over windows of twelve consecutive points. Hatched area represents the region where both scaling and no-scaling may be found. (B) Coefficient of variation over time. (C) $P(CV, scaling)$: probability densities of CV for trials that do or do not exhibit scaling. Hatched area covers the range of CV where both scaling and no scaling may be found, and a vertical line at $CV^* = 0.70$ marks the point at which scaling and non-scaling are equiprobable. (E,F,G,H) Exponents for the scalings of the (C) mean variance ($\widetilde{\alpha}$), (D) log silence probability inside a cluster ($\widetilde{\beta}$), (G) scaling of the covariance matrix eigenvalues ($\widetilde{\mu}$) and (H) exponent $\widetilde{z}$ for the scaling of the mean autocorrelation.

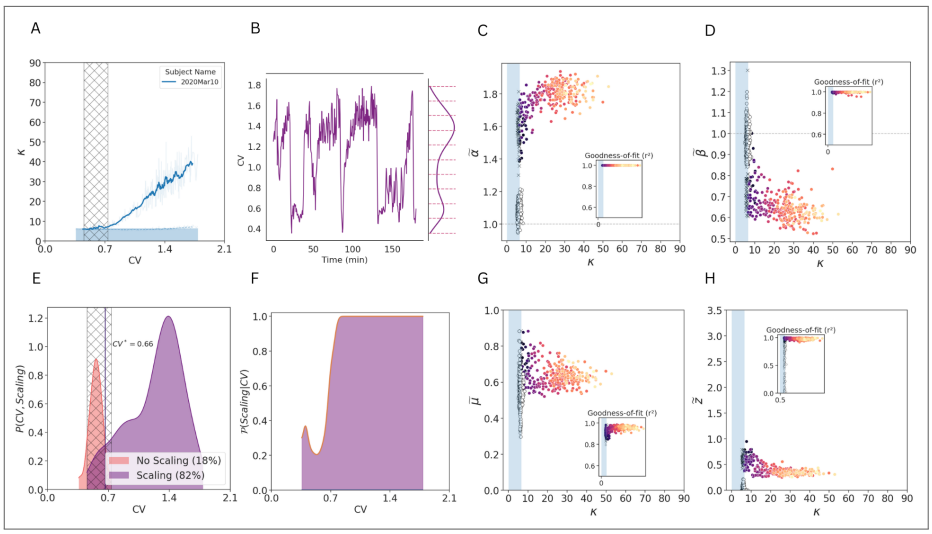

Source: (CASTRO et al., 2024)

Figure 45 – State dependent analysis for subject 2. (A) Kurtosis of the distribution of MS corse-grained variables (built from $N/64$ eigenmodes). Darker curve is the moving average over windows of twelve consecutive points. Hatched area represents the region where both scaling and no-scaling may be found. (B) Coefficient of variation over time. (C) $P(CV, scaling)$: probability densities of CV for trials that do or do not exhibit scaling. Hatched area covers the range of CV where both scaling and no scaling may be found, and a vertical line at $CV^* = 0.70$ marks the point at which scaling and non-scaling are equiprobable. (E,F,G,H) Exponents for the scalings of the (C) mean variance ($\widetilde{\alpha}$), (D) log silence probability inside a cluster ($\widetilde{\beta}$), (G) scaling of the covariance matrix eigenvalues ($\widetilde{\mu}$) and (H) exponent $\widetilde{z}$ for the scaling of the mean autocorrelation.

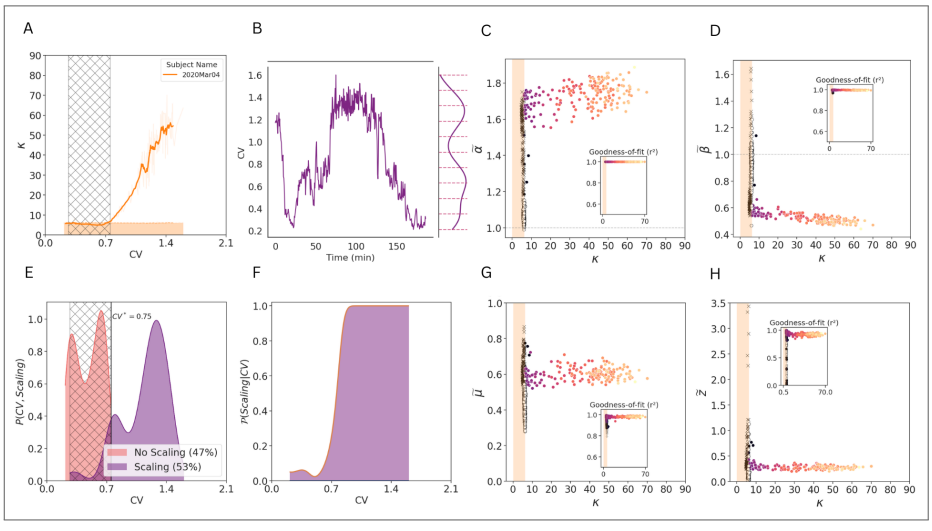

Source: (CASTRO et al., 2024)

Figure 46 – State dependent analysis for subject 3. (A) Kurtosis of the distribution of MS corse-grained variables (built from $N/64$ eigenmodes). Darker curve is the moving average over windows of twelve consecutive points. Hatched area represents the region where both scaling and no-scaling may be found. (B) Coefficient of variation over time. (C) $P(CV, scaling)$: probability densities of CV for trials that do or do not exhibit scaling. Hatched area covers the range of CV where both scaling and no scaling may be found, and a vertical line at $CV^* = 0.70$ marks the point at which scaling and non-scaling are equiprobable. (E,F,G,H) Exponents for the scalings of the (C) mean variance ($\widetilde{\alpha}$), (D) log silence probability inside a cluster ($\widetilde{\beta}$), (G) scaling of the covariance matrix eigenvalues ($\widetilde{\mu}$) and (H) exponent $\widetilde{z}$ for the scaling of the mean autocorrelation.

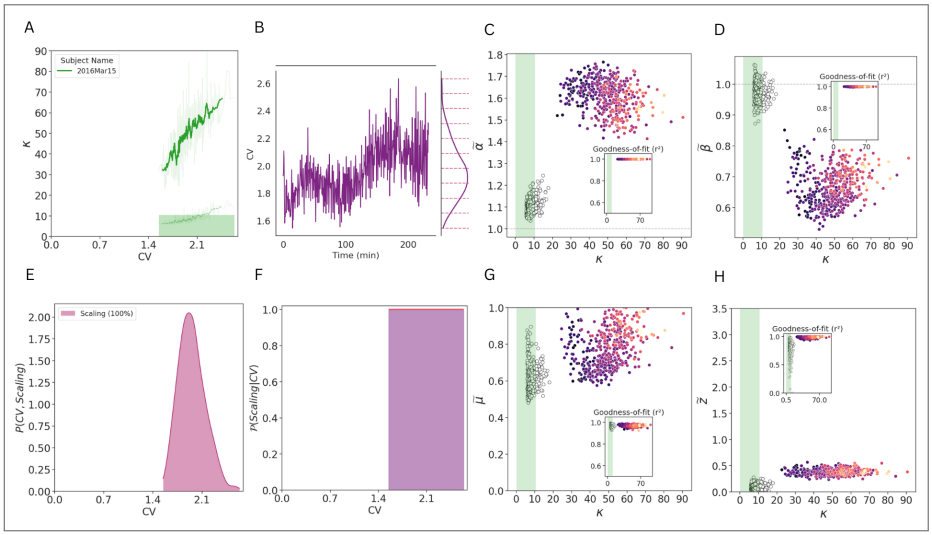

Source: (CASTRO et al., 2024)

Figure 47 – State dependent analysis for subject 4. (A) Kurtosis of the distribution of MS corse-grained variables (built from $N/64$ eigenmodes). Darker curve is the moving average over windows of twelve consecutive points. Hatched area represents the region where both scaling and no-scaling may be found. (B) Coefficient of variation over time. (C) $P(CV, scaling)$: probability densities of CV for trials that do or do not exhibit scaling. Hatched area covers the range of CV where both scaling and no scaling may be found, and a vertical line at $CV^* = 0.70$ marks the point at which scaling and non-scaling are equiprobable. (E,F,G,H) Exponents for the scalings of the (C) mean variance ($\widetilde{\alpha}$), (D) log silence probability inside a cluster ($\widetilde{\beta}$), (G) scaling of the covariance matrix eigenvalues ($\widetilde{\mu}$) and (H) exponent $\widetilde{z}$ for the scaling of the mean autocorrelation.

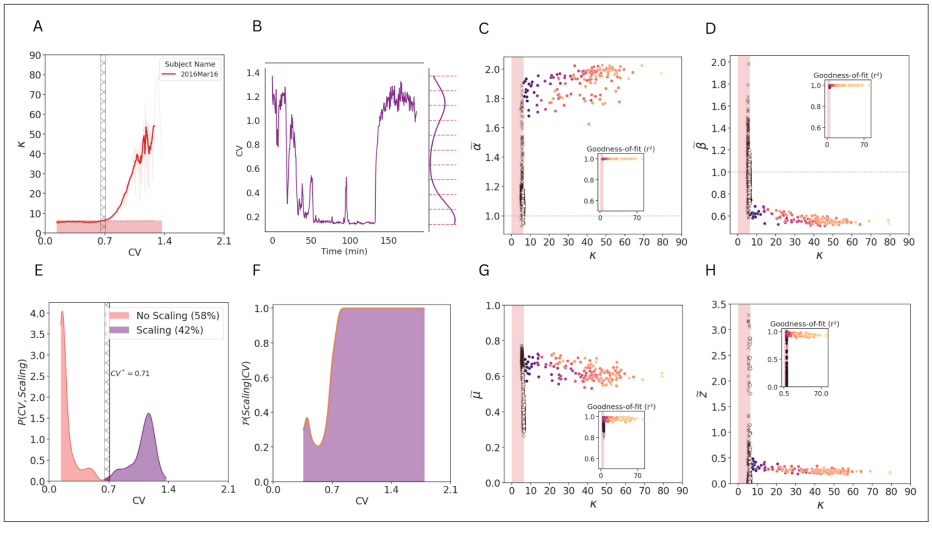

Source: (CASTRO et al., 2024)

Figure 48 – State dependent analysis for subject 5. (A) Kurtosis of the distribution of MS corse-grained variables (built from $N/64$ eigenmodes). Darker curve is the moving average over windows of twelve consecutive points. Hatched area represents the region where both scaling and no-scaling may be found. (B) Coefficient of variation over time. (C) $P(CV, scaling)$: probability densities of CV for trials that do or do not exhibit scaling. Hatched area covers the range of CV where both scaling and no scaling may be found, and a vertical line at $CV^* = 0.70$ marks the point at which scaling and non-scaling are equiprobable. (E,F,G,H) Exponents for the scalings of the (C) mean variance ($\widetilde{\alpha}$), (D) log silence probability inside a cluster ($\widetilde{\beta}$), (G) scaling of the covariance matrix eigenvalues ($\widetilde{\mu}$) and (H) exponent $\widetilde{z}$ for the scaling of the mean autocorrelation.

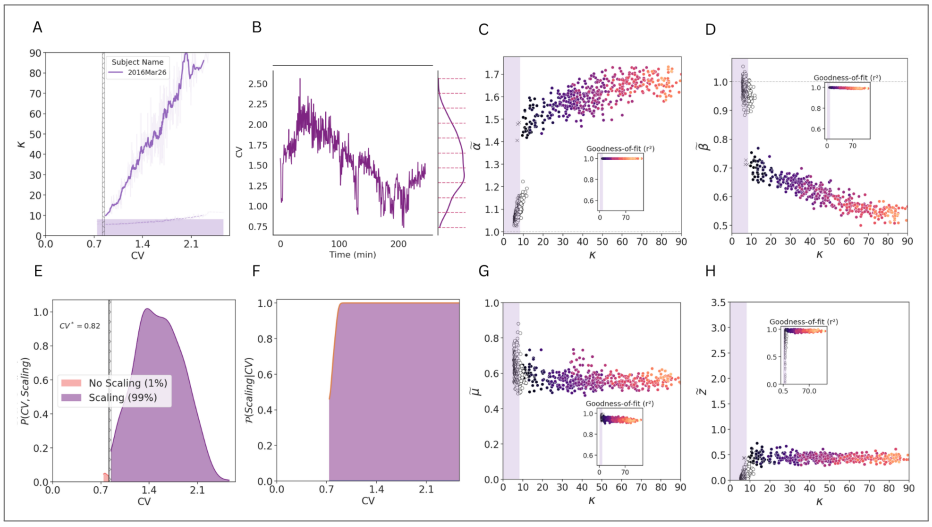

Source: (CASTRO et al., 2024)

Figure 49 – State dependent analysis for subject 6. (A) Kurtosis of the distribution of MS corse-grained variables (built from $N/64$ eigenmodes). Darker curve is the moving average over windows of twelve consecutive points. Hatched area represents the region where both scaling and no-scaling may be found. (B) Coefficient of variation over time. (C) $P(CV, scaling)$: probability densities of CV for trials that do or do not exhibit scaling. Hatched area covers the range of CV where both scaling and no scaling may be found, and a vertical line at $CV^* = 0.70$ marks the point at which scaling and non-scaling are equiprobable. (E,F,G,H) Exponents for the scalings of the (C) mean variance ($\widetilde{\alpha}$), (D) log silence probability inside a cluster ($\widetilde{\beta}$), (G) scaling of the covariance matrix eigenvalues ($\widetilde{\mu}$) and (H) exponent $\widetilde{z}$ for the scaling of the mean autocorrelation.

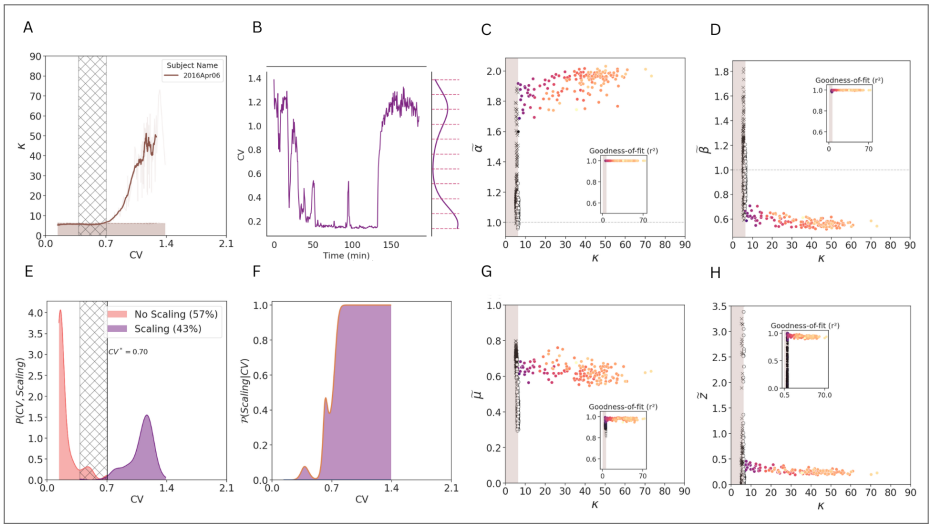

Source: (CASTRO et al., 2024)

Figure 50 – State dependent analysis for subject 7. (A) Kurtosis of the distribution of MS corse-grained variables (built from $N/64$ eigenmodes). Darker curve is the moving average over windows of twelve consecutive points. Hatched area represents the region where both scaling and no-scaling may be found. (B) Coefficient of variation over time. (C) $P(CV, scaling)$: probability densities of CV for trials that do or do not exhibit scaling. Hatched area covers the range of CV where both scaling and no scaling may be found, and a vertical line at $CV^* = 0.70$ marks the point at which scaling and non-scaling are equiprobable. (E,F,G,H) Exponents for the scalings of the (C) mean variance ($\widetilde{\alpha}$), (D) log silence probability inside a cluster ($\widetilde{\beta}$), (G) scaling of the covariance matrix eigenvalues ($\widetilde{\mu}$) and (H) exponent $\widetilde{z}$ for the scaling of the mean autocorrelation.

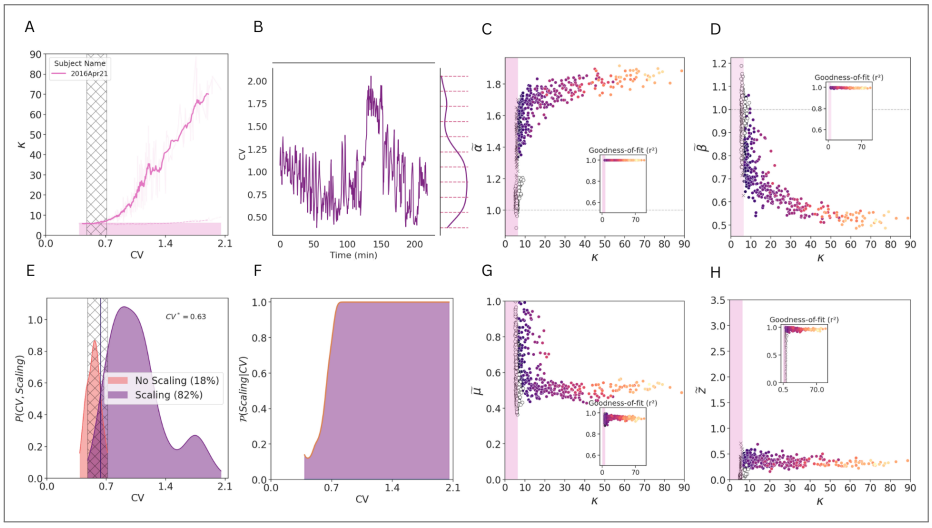

Source: (CASTRO et al., 2024)

Figure 51 – State dependent analysis for subject 8. (A) Kurtosis of the distribution of MS corse-grained variables (built from $N/64$ eigenmodes). Darker curve is the moving average over windows of twelve consecutive points. Hatched area represents the region where both scaling and no-scaling may be found. (B) Coefficient of variation over time. (C) $P(CV, scaling)$: probability densities of CV for trials that do or do not exhibit scaling. Hatched area covers the range of CV where both scaling and no scaling may be found, and a vertical line at $CV^* = 0.70$ marks the point at which scaling and non-scaling are equiprobable. (E,F,G,H) Exponents for the scalings of the (C) mean variance ($\widetilde{\alpha}$), (D) log silence probability inside a cluster ($\widetilde{\beta}$), (G) scaling of the covariance matrix eigenvalues ($\widetilde{\mu}$) and (H) exponent $\widetilde{z}$ for the scaling of the mean autocorrelation.

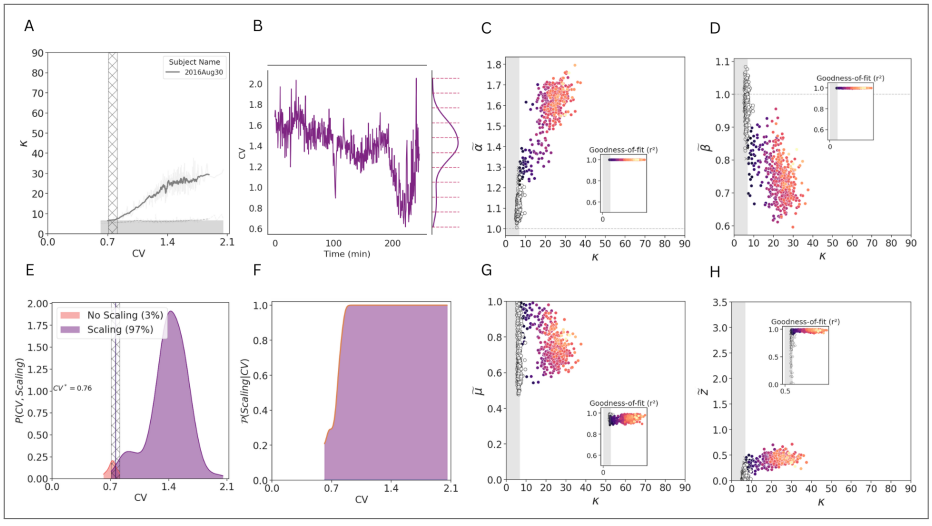

Source: (CASTRO et al., 2024)

Figure 52 – State dependent analysis for subject 9. (A) Kurtosis of the distribution of MS corse-grained variables (built from $N/64$ eigenmodes). Darker curve is the moving average over windows of twelve consecutive points. Hatched area represents the region where both scaling and no-scaling may be found. (B) Coefficient of variation over time. (C) $P(CV, scaling)$: probability densities of CV for trials that do or do not exhibit scaling. Hatched area covers the range of CV where both scaling and no scaling may be found, and a vertical line at $CV^* = 0.70$ marks the point at which scaling and non-scaling are equiprobable. (E,F,G,H) Exponents for the scalings of the (C) mean variance ($\widetilde{\alpha}$), (D) log silence probability inside a cluster ($\widetilde{\beta}$), (G) scaling of the covariance matrix eigenvalues ($\widetilde{\mu}$) and (H) exponent $\widetilde{z}$ for the scaling of the mean autocorrelation.

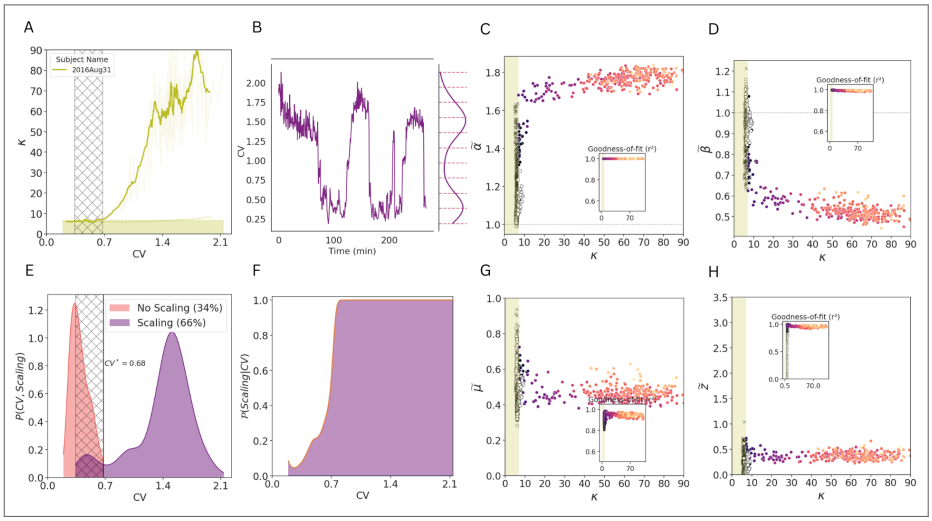

Source: (CASTRO et al., 2024)

APPENDIX C – ON THE THRESHOLD CHOICE IN PRG ANALISYS OF FMRI DATA

In Chap. 4, we had to binarize continuous fMRI data in order to apply the PRG method. To do so, we applied a z-score score upper threshold to define events in the time series $\{\sigma_i(t)\}$ for a fixed threshold $z_{th} = 2$. Here, we turn address how the PRG exponents and exponent relations vary in function of this threshold choice.

Figure 53 – Scaling of different observables in the PRG for different choices of the z-score threshold used to determine events in continuous data.

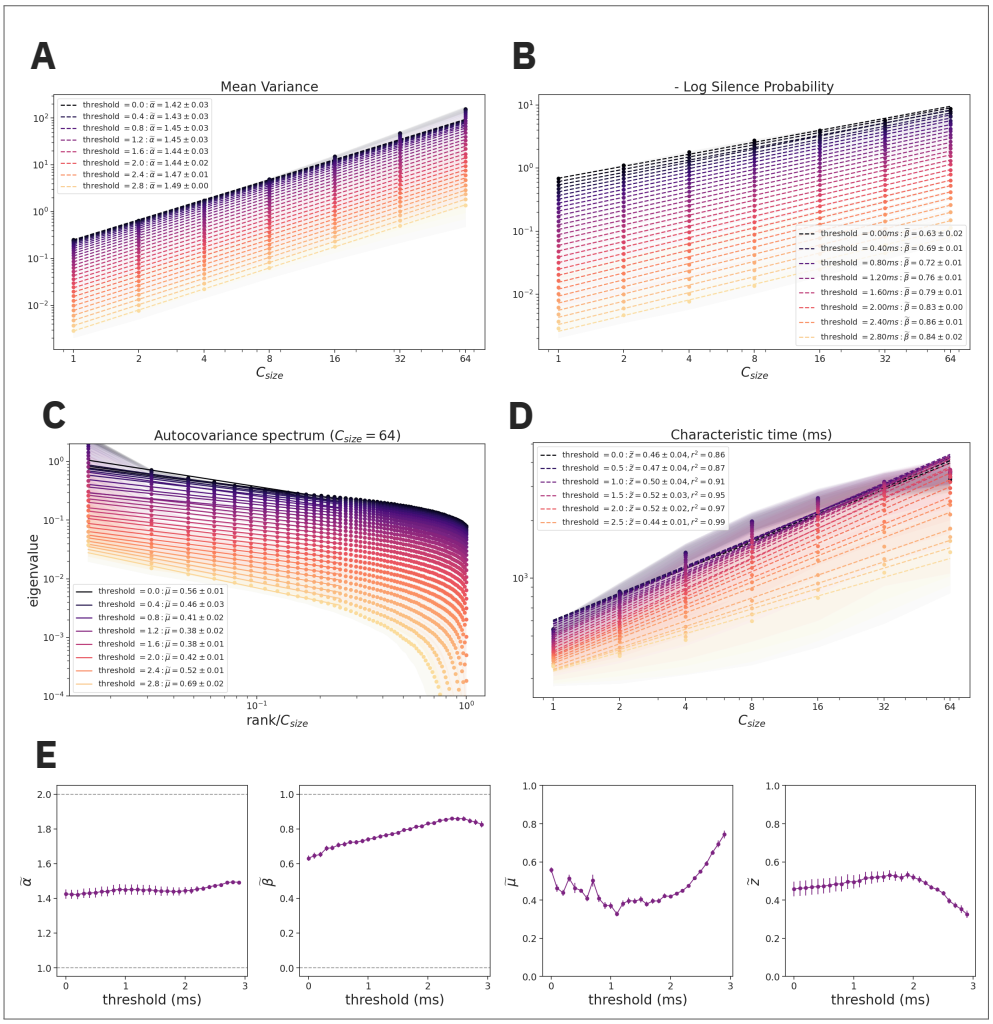

Source: Provided by the author.

First, we show the different exponents found when repeating the procedure for single subject, with $0 \leq z_{threshold} \leq 3$ (Fig. 53). While exponents $\widetilde{\alpha}$ and $\widetilde{\beta}$ remain stable or increase linearly, exponents $\widetilde{\mu}$ and $\widetilde{z}$ seem to behave in a less predictable manner. For the $\widetilde{z}$ exponent from the scaling of the autocorrelation function, in particular, power law adjustments also lose

their goodness-of-fit for lower thresholds, where any activity above average counts as an event in the binary time series.

Figure 54 – Histogram of PRG exponents calculated for each participant in the HCP-YA dataset (left) for different thresholds z_{th}. Spearman rank correlation coefficients between distributions show how much the change in exponent values affect their ordering within the distribution (right).

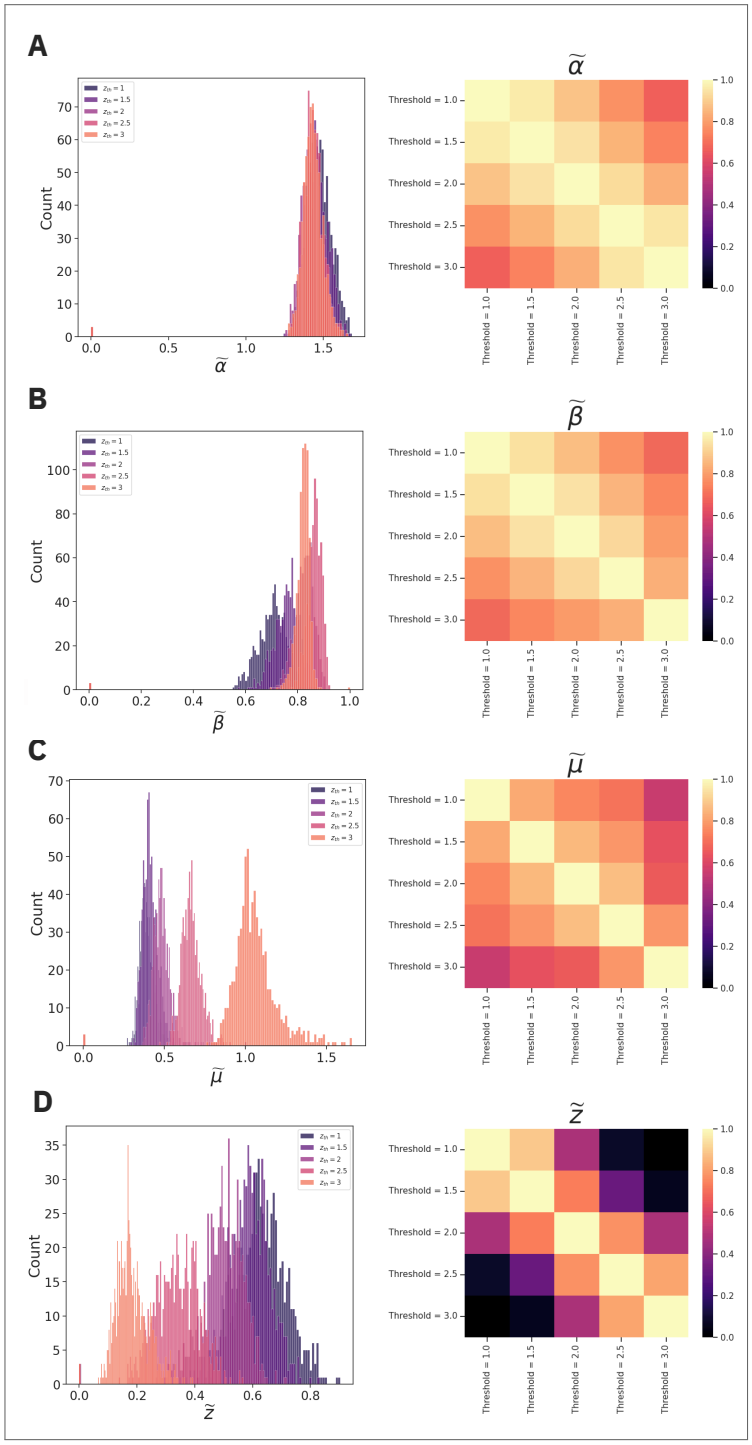

Source: Provided by the author.

In Fig. 54, we see how this impression translates to group data. In the left side, we show histograms of all exponents obtained for all participants in the Young Adults (YA) dataset.

Results align with the trend obtained for a single subject. the $\widetilde{\alpha}$, in particular, seems to be completely unaffected by the value of z_{th}. Then, we examine whether the shift in the exponent distributions cause by threshold choice interfere in the ordering of the values within the distribution (i.e., if extreme values of the distribution still come from the same experiments when the threshold is changed). We do this by calculating Spearman's rank correlation between histograms. Like in our first impression, Spearman's coefficients show that $\widetilde{\beta}$ values are orderly shifted by the choice of threshold, alghough the same does not happen for the other two exponents that change with z_{th}. The distributions for exponent $\widetilde{z}$ from high and low thresholds have actually correlation coefficients near 0, suggesting that the change in the data's temporal structure induced by threshold choice completely scrambles how the autocorrelation scales.

On the other hand, the ordered shift in the $\widetilde{\beta}$ distribution hints that we may write its values as a function of z_{th}. Something similar was already employed by Petermann *et al.* (PETERMANN et al., 2009b), where authors calculated the shape collapse for avalanche distributions obtained from different bin duration lengths. To achieve a shape collapse of the silence probability as a function of C_{size}, we do the following: first, we restrict threshold values to $0.5 \leq z_{th} \leq 2.5$. We do this because, for extreme values of threshold, the activity distribution of coarse-grained variables may become pathological (i.e. close to being completely silent or to have no silences at all) (Fig. 55A), which may cause unexpected distortions in the scaling exponent calculation. Then, we find the linear coefficients that best adjust the $\widetilde{\beta}$ *versus* z_{th} line (Fig. 55B), and use them in the rescaling

$$\mathcal{F}(C_{size}) \rightarrow \mathcal{F}(C_{size}).(C_{size})^{\widetilde{\beta}(2)-\widetilde{\beta}(z_{th})}. \tag{C.1}$$

Fig. 55C is the same as Fig. 53B with the rescaling from above applied to obtain the shape collapse of different curves.

Finally, we show what would the exponent relations from Fig. 36 look like for different threshold choices. Besides avoiding extreme z_{th}, there is another reason to choose $z_{th} = 2$ as our standard threshold: it is also the value which yields the best adjustment for all relations we have found previously.

Figure 55 – (A) Activity distribution of coarse-grained variables for different choices of z-score threshold z_{th}. (B) Exponents $\widetilde{\alpha}$ and $\widetilde{\beta}$ obtained for different z_{th}, along with linear fits. (C) Probability of silence in coarse-grained variables rescaled according to Eq. C.1.

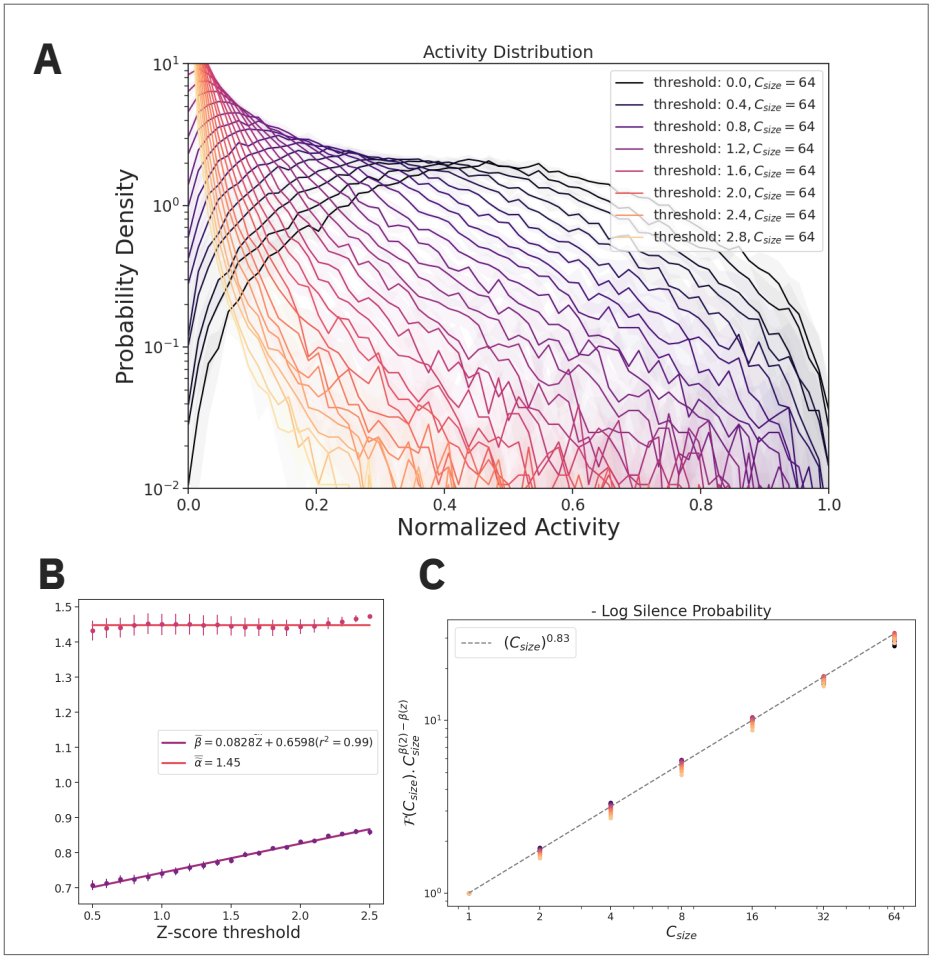

Source: Provided by the author.

Figure 56 – PRG exponent relations for different choices choices of z-score threshold z_{th}. Insets show the goodness-of-fit for each case.

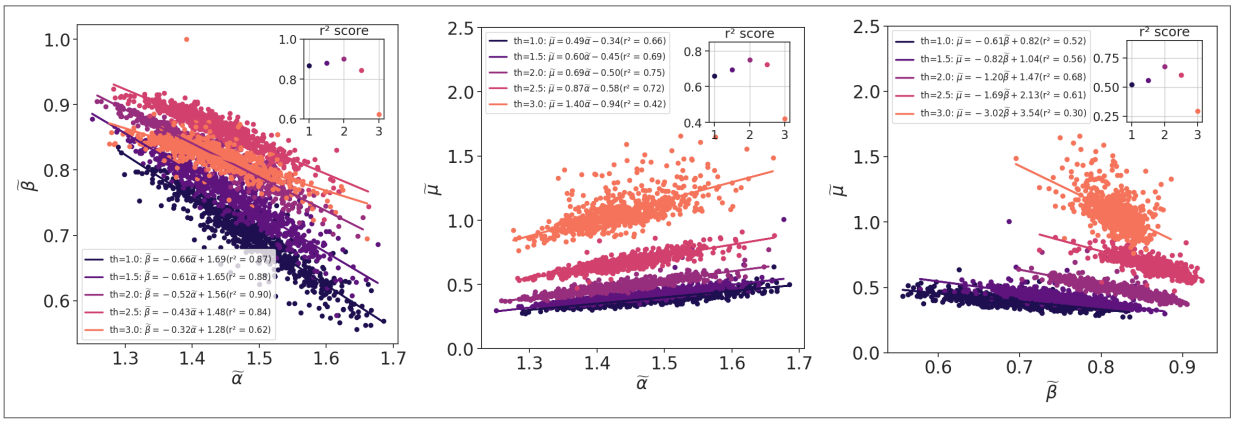

Source: Provided by the author.